Photoacoustic spectroscopy of $^{14}CH_4$ using a mid-infrared optical parametric oscillator

Master's thesis
Santeri Larnimaa
Molecular Science
University of Helsinki
April 2020

HELSINGIN YLIOPISTO
HELSINGFORS UNIVERSITET
UNIVERSITY OF HELSINKI
MATEMAATTIS-LUONNONTIETEELLINEN TIEDEKUNTA
MATEMATISK-NATURVETENSKAPLIGA FAKULTETEN
FACULTY OF SCIENCE

Tiedekunta – Fakultet – Faculty Faculty of Science	Koulutusohjelma – Utbildningsprogram – Degree programme Master's Programme in Chemistry and Molecular Sciences	
Tekijä – Författare – Author Santeri Larnimaa		
Työn nimi – Arbetets titel – Title Photoacoustic spectroscopy of $^{14}CH_4$ using a mid-infrared optical parametric oscillator		
Työn laji – Arbetets art – Level Master's thesis	Aika – Datum – Month and year April 2020	Sivumäärä – Sidoantal – Number of pages 76

Tiivistelmä – Referat – Abstract

Radiomethane ($^{14}CH_4$) is a radioactive isotopologue of methane known to be emitted from nuclear facilities. As methane is a potent greenhouse gas and measuring the concentration of carbon-14 in a methane sample gives information about the origin of the sample, it is important to be able monitor $^{14}CH_4$. The state-of-the-art method for radiomethane measurements is accelerator mass spectrometry, but optical methods have also been proposed due their affordability and suitability for field measurements. Radiomethane has already been measured with optical methods, but usually indirectly by first combusting it to carbon dioxide – direct measurement of radiomethane with optical methods would require spectroscopic information, and the first absorption spectrum of radiomethane was measured only in the year 2019.

In this thesis, the exploration of the CH-stretching vibrational band ν_3 of $^{14}CH_4$ is continued: Total of 43 lines with 17 new lines have been measured and assigned with improved accuracy. Furthermore, the widths of the lines have been studied in detail for the first time and a simple model to estimate the $^{14}CH_4$ line positions to aid possible future research on radiomethane is presented. The measurements were conducted with photoacoustic spectroscopy using frequency modulation techniques and a mid-infrared continuous-wave optical parametric oscillator (OPO) as a light source. The OPO frequency was referenced to a wavelength meter and the frequency scanning (measuring over an absorption line) was executed with a proportional–integral–derivative controller in LabVIEW. The novel results presented in this thesis are useful for possible future applications in quantitative analysis of radiomethane, and the results are also relevant for fundamental research as radiomethane is the last naturally occurring isotopologue of methane that has not yet been extensively studied with optical methods.

Avainsanat – Nyckelord – Keywords
Radiomethane, methane, carbon-14, mid-infrared, vibrational band, optical methods, photoacoustic spectroscopy, frequency modulation, optical parametric oscillator, OPO, linewidth

Säilytyspaikka – Förvaringställe – Where deposited
Helda / E-Thesis

Contents

1. Introduction

Methane (CH_4) is an important substance that is emitted into the atmosphere for example from wetlands, biomass burning and exploitation of fossil fuels.[2] Even though the concentration of methane in the atmosphere is only about 1.87 ppm (parts per million),[3] methane is undeniably a potent greenhouse gas having about 34 times the global warming potential of carbon dioxide.[4] It is therefore important to better understand the origin of methane emissions, for example, whether the methane originates from a biogenic or a fossil source.[2] This can be accomplished by measuring the radiocarbon (^{14}C) content in a methane sample.[5,6]

Radiocarbon is a radioactive isotope of carbon. It is a low-energy β-emitter (0.156 MeV)[7] with a half-life of 5730 a.[8] Its natural abundance in carbon is only about 1.2 ppt (parts per trillion),[9] which has the consequence that radiomethane exists naturally in minuscule, parts per quintillion amounts in the atmosphere! In order to detect such small concentrations, highly sensitive methods are needed – even with the state of the art method, acceleration mass spectrometry (AMS),[10] preconcentration methods are used.[11] Even though AMS is a very sensitive method, it is considered expensive, laborious and not well suited for field applications.[1,12,13]

For these reasons, optical methods for radiocarbon measurements have been proposed, and such methods have already proven highly sensitive in this application.[12,14] Especially radioactive carbon dioxide ($^{14}CO_2$) has been studied so that it could be monitored in emissions from nuclear facilities by optical methods,[13,15] an application relevant also for radiomethane, as radiomethane is produced among other radioactive organic species in nuclear processes.[16] For example, Genoud *et al.*[15] have developed an optical measurement setup that is capable of detecting $^{14}CO_2$ concentrations relevant to the nuclear industry and recently[13] they demonstrated measuring $^{14}CO_2$ and radiomethane from atmospheric-like samples as a step towards in-situ continuous monitoring of radiocarbon emissions from nuclear facilities: in their system, radiomethane was measured by catalytically converting it to $^{14}CO_2$ and deducing the amount of $^{14}CH_4$ from a measurement without using the catalyst.

For accurate radiomethane measurements however, it would be important to be able to measure radiomethane directly. This has not been possible yet due to lack of spectroscopic information on $^{14}CH_4$: the first measured absorption spectrum of radiomethane was reported only last year (2019) by Karhu *et al.*[1] They measured the anti-symmetric CH-stretching vibrational band[17] ν_3 of $^{14}CH_4$ using photoacoustic Fourier transform spectroscopy with a mid-infrared optical frequency comb as a light source. They managed to measure several lines especially in the R-branch, but due to a relatively low signal-to-noise ratio (SNR) and resolution, only a few lines in the P-branch could be reliably assigned.

In this thesis, the work by Karhu *et al.*[1] is continued. A mid-infrared continuous-wave optical parametric oscillator (OPO) has been utilized in a photoacoustic spectroscopy experiment based on frequency modulation techniques to measure several lines in the same CH-stretching vibrational band ν_3 of $^{14}CH_4$, but with higher resolution, SNR and accuracy. Many of the lines are in the P-branch, and the total number of measured lines is 43 with 17 lines that have never been reliably assigned before. In addition, the widths of the measured transitions are reported, and an updated model to estimate the positions of $^{14}CH_4$ lines is presented to aid possible future research on radiomethane.

The structure of the thesis is as follows: Section 2 discusses the background of the used measurement methods, and section 3 describes the experimental setup designed for the $^{14}CH_4$ measurements. For example, section 2.1 introduces briefly the basic concepts relevant for understanding optical parametric oscillation, and section 3.1 concentrates on the experimental design and characterization of the OPO constructed for the measurements, because the experimental design has some interesting aspects. For instance, the OPO was referenced to a wavelength meter and the frequency scanning (measuring over an absorption line) was executed using a proportional–integral–derivative controller in LabVIEW.

Similarly, section 2.2 discusses photoacoustic spectroscopy and frequency modulation, and section 3.2 considers the photoacoustic setup designed for the $^{14}CH_4$ measurements and concludes the description of the experimental setup. The rest of this thesis (section 4) analyses in detail the results of the radiomethane measurements; the determined line positions and linewidths are tabulated in appendix A and B, respectively, and appendices C–G discuss some additional, but important aspects of the measurements.

The results presented in this thesis are important for future applications that would rely on direct detection of radiomethane with optical methods. In addition, $^{14}CH_4$ is the last naturally occurring isotopologue of methane whose spectroscopic properties have not yet been thoroughly studied with optical methods, which also makes the results presented in this thesis interesting and relevant for fundamental research.

2. Background

2.1. Optical parametric oscillator

An optical parametric oscillator (OPO) can be thought of as a wavelength converter, and, in the work described in this thesis, such an instrument was built and used to convert laser light in the near-infrared region (1064 nm) into light in the mid-infrared region (2.7–3.4 μm), where conventional laser light generation can be difficult.[18] The first OPO was reported already in the sixties,[19] and OPOs have since been used in a variety of spectroscopic applications,[20] for example in this thesis to measure the antisymmetric vibrational band ν_3 of radiomethane. The theory of OPOs has already been reviewed in several pieces of literature,[20–24] which is why only the basic concepts of the method are briefly discussed in this section. In section 3.1 however, special emphasis is given on the experimental design and characterization of the OPO constructed in this thesis work.

Optical parametric oscillation is based on a nonlinear optical parametric process[20,24] that may occur when a so-called nonlinear material is radiated with a high power light source that has a proper polarization.[25] In our case, a $LiNbO_3$ crystal is radiated with a high power laser whose output beam is extraordinarily polarized relative to the crystal lattice.[26] In the process, two photons interact generating a third photon whose frequency is the difference of the incident photon frequencies. The process must conserve energy, which can be expressed as[24]

$$\nu_{\text{idler}} = \nu_{\text{pump}} - \nu_{\text{signal}} \,, \tag{1}$$

where the labels "pump", "signal" and "idler" have been chosen to follow the common convention.

In an OPO, the process described by equation (1) is utilized by building a resonator around the nonlinear material. For example in the OPO presented in section 3.1, a continuous-wave laser beam (the pump) is focused into the $LiNbO_3$ crystal. If certain conditions discussed below are met, a signal beam is generated from quantum noise[27] and amplified in the resonator. These two light beams will result in an idler beam based on equation (1), and this idler beam is now used as a light source in the photoacoustic experiment discussed in later sections.

The probability of the nonlinear effect depends on the spatial overlap of the pump and signal beams (resonator alignment) but also on the focus tightness of the beams. A dimensionless quantity to describe this is called the focusing parameter:[20]

$$\xi_j = \frac{L\lambda_j}{2\pi w_j^2 n_j}\,, \tag{2}$$

where L is the length of the crystal, λ_j is the wavelength of a beam with a label j, w_j is the waist size of the crystal focus and n_j is the corresponding refractive index. It has been theoretically shown that the optimum focusing parameter is about 2.84 assuming the same focusing parameter for the beams.[25] However, a focusing parameter in the order of one is commonly used,[20,28] as the response of the gain to ξ is quite flat within this range;[25] in the OPO presented in section 3.1 a focusing parameter of 1.9 was used.

Another condition for the nonlinear process to be efficient is that the phases of the pump and signal waves need to be matched:[24] Due to the frequency dependency of the refractive index of the crystal (see the Sellmeier equation, for example, in reference 29), the waves will travel in the medium at slightly different speeds with a consequence that newly generated signal waves will eventually fall out of phase and interfere destructively with the already formed signal beam. The phase matching condition to ensure efficient signal beam amplification can be written as[24]

$$\Delta k = k_{\text{pump}} - k_{\text{signal}} - k_{\text{idler}} = 0\,, \tag{3}$$

where $k_j = 2\pi n_j/\lambda_j$ is the angular wavenumber of the beam with a label j.

A method often used to ensure sufficient enough phase matching is quasi phase matching[24] (QPM), which is also used in the OPO presented in section 3.1. In the QPM, the used crystal is periodically poled, in other words, manufactured such that the crystal lattice

direction always changes by 180° after some constant distance called the poling period. Usually these types of crystals have domains with different poling periods next to each other so that the pump beam can be guided through different domains in the crystal in order to change the phase matching condition by moving the crystal on a translational stage for example. With QPM, the phase matching condition can be written as[24]

$$\Delta k = k_{\text{pump}} - k_{\text{signal}} - k_{\text{idler}} - \frac{2\pi}{\Lambda}\,, \tag{4}$$

where Λ is the poling period (in the range of 28.5–31.5 μm for the crystal used in the OPO discussed in section 3.1).

Note that the phase matching does not need to be exactly zero for amplification of the signal beam in the resonator to be nonzero. The so-called gain profile describes signal power as a function of phase matching Δk:[24]

$$P_{\text{signal}} \propto P_{\text{idler}} \propto \operatorname{sinc}\left(\frac{\Delta k L}{2\pi}\right), \tag{5}$$

where L is the length of the crystal and the proportionality is only an approximation. Note that the gain profile is also a function of ν_{signal} via equation (4), and the gain is plotted as a function of signal frequency in figure 1 (left vertical axis) to illustrate its shape.

Only the top part of the gain profile has been shown in figure 1 because the gain must surpass a certain threshold for the optical parametric oscillation to start. This is because the total gain in one round trip must overcome the net losses inside the resonator for the signal to be amplified. This is in practice ensured by pumping the crystal with high enough power provided that the other conditions for the optical parametric oscillation explained above are met.

An important detail not explicitly illustrated in figure 1 is that even if all of the above-mentioned conditions are met, not all of the frequencies allowed by the gain profile will result in OPO action, because the resonator itself supports only certain signal frequencies.[24] In other words, there are certain resonator modes[30] in which the OPO can start to oscillate, and the distance between these modes in frequency domain is usually assumed constant and called the free spectral range (FSR) of the resonator. For example, the FSR of the OPO resonator discussed in section 3.1 is about 400 MHz, which means that there are several modes in which the OPO can start to oscillate.

Usually however, the OPO starts to oscillate only in one resonator mode, preferably the one that corresponds to minimum losses.[24] However, due to external interferences, temperature drifting and, for example, the fact that the gain profile is usually relatively flat, the resonator mode that corresponds to minimum losses might not be unambiguous or it might change during an experiment. As a result, the OPO can change the mode that it is oscillating in, and this phenomenon is called mode hopping.[20] Mode hopping of OPOs is common and a nuisance in spectroscopic applications, because ideally one would want to tune the idler frequency in a continuous manner over the absorption feature of interest, but a mode hop will result in a step like change in the idler frequency.

A common way to prevent mode hopping is to place an etalon[30] inside the resonator. An etalon is a component that induces frequency dependent losses as illustrated in figure 1 (the right vertical axis). The etalon will force the OPO to oscillate in a resonator mode close to the transmission maximum of the etalon, which will in turn reduce the probability of a mode hop. Figure 2 (an animation) illustrates the net effect of the gain and etalon losses and how the position of the resulting net gain maximum can be changed by changing the etalon angle, in other words, by effectively changing the etalon FSR. The figure implies that a mode hop can also be induced by turning the etalon, because turning the etalon will increase losses at the frequency of the current oscillating mode and the probability of a mode hop increases. This is sometimes useful, which will be seen in section 3.1.2.

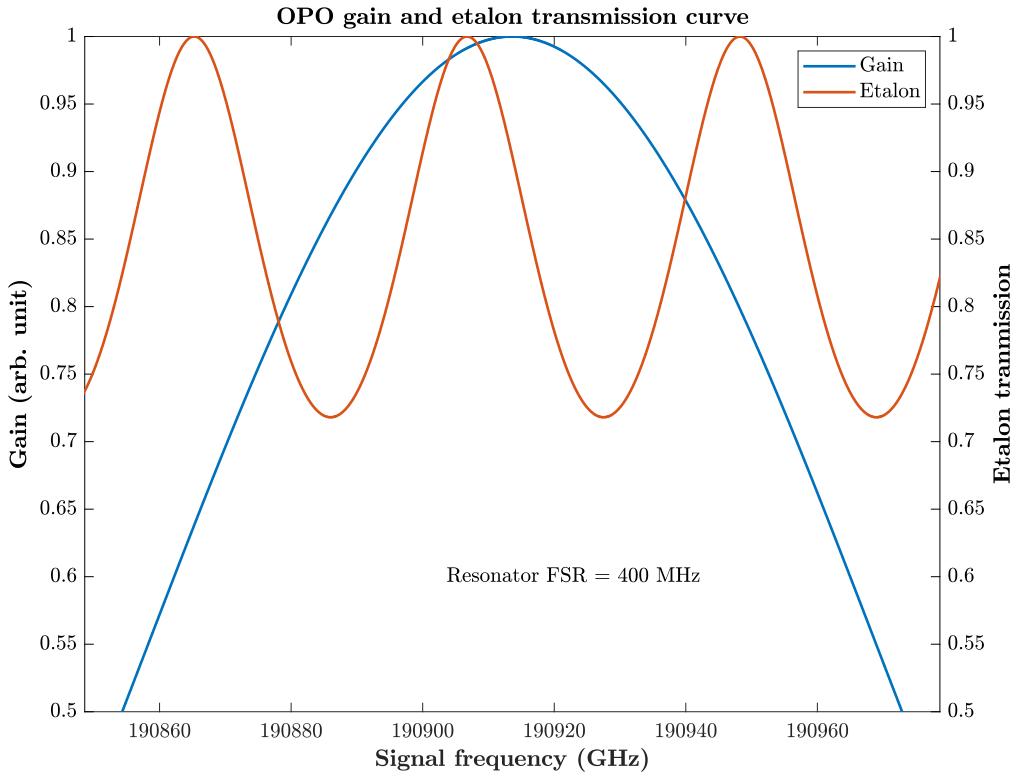

Figure 1: Simulation of the OPO gain curve (left vertical axis) for the OPO presented in section 3.1, and the transmission curve of a 40 GHz FSR etalon (right vertical axis) used to manage mode hopping in the experimental setup (subsection 3.1.2). The resonator modes are not included in the figure, because the FSR of resonator is small relative to the etalon FSR.

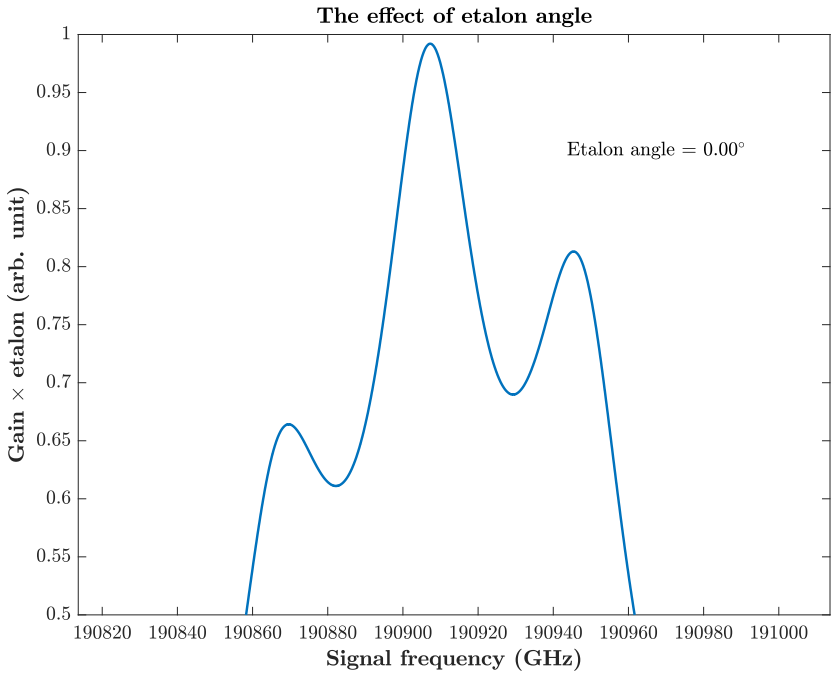

Figure 2: An animation illustrating the net gain defined by the gain profile and the etalon in figure 1.

2.2. Photoacoustic spectroscopy and frequency modulation

Photoacoustic spectroscopy (PAS) is one the most sensitive optical methods for trace gas analysis, capable of detecting even sub-parts-per-trillion concentrations.[31] PAS is based on generating periodic absorption in a closed cell that contains the sample to be measured: periodic absorption leads to periodic temperature changes and, in a constant volume, to periodic pressure changes, in other words, to an acoustic signal that can be monitored with a microphone.[32] Conventional capacitive microphones can be used, but in recent years, a detector based on measuring the movement of a silicon cantilever by laser interferometry has proven to offer significantly improved detection sensitivities.[31,33,34] This method, referred to as cantilever-enhanced photoacoustic spectroscopy (CEPAS), is also utilized in the radiomethane measurements discussed in this thesis.

There are several approaches to generate the periodic absorption necessary for PAS.[35] The simplest of these may be the method of amplitude modulation using a chopper, where a light beam aligned into the sample cell is chopped with a certain frequency: the output signal of the detector can be, for example, Fourier transformed, and the Fourier component corresponding to the modulation frequency is proportional to the sample absorption.[36] One problem of amplitude modulation is that undesired background absorption, for example, by the cell windows may interfere with the absorption features of interest. This can be avoided by using frequency modulation techniques,[37] because in such methods the measured signal is proportional to different order derivatives of the absorption feature,[38] which will result in efficient rejection of constant or nearly constant background absorptions.[39]

The method of frequency modulation was also utilized in the radiomethane measurements discussed in this thesis, which is why the rest of this section covers the basics of frequency modulation and how to measure the so-called second harmonic spectrum of an absorption feature. It is important to note that the following mathematical expression derived for the so-called second harmonic coefficient is only illustrative; the more formal theory of frequency modulation techniques has been extensively scrutinized, for example, in reference 37. The derivation below is based on references 38 and 40.

In frequency modulation, the frequency of the light source, for example a laser or in our case the OPO idler, is modulated at some center frequency:

$$\nu_{\text{idler}} = \nu_{\text{center}} + \nu_{\text{MA}} \cos(\omega_{\text{MF}} t) \,, \quad \omega_{\text{MF}} = 2\pi f_{\text{MF}} \,, \tag{6}$$

where ν_{MA} is the modulation amplitude (MA) and f_{MF} the modulation frequency (MF). If the strength of absorption is not constant within $\nu_{\text{center}} \pm \nu_{\text{MA}}$, periodic absorption and therefore an acoustic signal is generated.

Let us assume that we want to measure an absorption feature whose shape is determined by a function $\alpha(\nu)$. In PAS, the strength of absorption signal also depends on the power of the incident light,[32] but if the power can be assumed frequency (and time) independent, it behaves as a constant and is for simplicity omitted in the following discussion. If this independency assumption cannot be made, the power fluctuations will couple into the measurement system and lead to different kinds of unwanted features in the measured spectrum,[37] which is briefly illustrated in appendix G. Also note that because the PAS signal is proportional to the power of the light source,[32] the output power of the OPO presented in section 3.1 was maximized. If we now expand $\alpha(\nu)$ as Taylor series at ν_{center}, the acoustic signal can be written as

$$\alpha(\nu_{\text{idler}}) = \sum_{n=0}^{\infty} \frac{\alpha^{(n)}(\nu_{\text{center}})}{n!} \nu_{\text{MA}}^n \cos^n(\omega_{\text{MF}} t) \,, \tag{7}$$

where the powers of the cosine function can be expressed as[41]

$$\cos^n(x) = \begin{cases} \frac{1}{2^{n-1}} \sum_{k=0}^{\frac{n-1}{2}} \binom{n}{k} \cos\left[(n-2k)x\right] \,, & n \text{ is odd} \\ \frac{1}{2^n} \binom{n}{\frac{n}{2}} + \frac{1}{2^{n-1}} \sum_{k=0}^{\frac{n}{2}-1} \binom{n}{k} \cos\left[(n-2k)x\right] \,, & n \text{ is even} \end{cases} . \tag{8}$$

The objective is to reorganize expression (7) into the corresponding Fourier series and find an expression for the second Fourier coefficient. In other words, the goal is to express the above expression as

$$\alpha(\nu_{\text{idler}}) = \sum_{n=0}^{\infty} c_n \cos(n\omega_{\text{MF}} t) \,, \tag{9}$$

which can be accomplished directly by reorganizing the expression (7) using (8). Furthermore, the second Fourier coefficient c_2 can be obtained by noting that only terms with $k = \frac{n}{2} - 1$ in the even powers of cosine functions ($n = 2m, m \in \mathbb{N}_1$) contribute to the coefficient:

$$c_2(\nu_{\text{center}}) = \sum_{m=1}^{\infty} \frac{\alpha^{(2m)}(\nu_{\text{center}})}{(2m)!} \nu_{\text{MA}}^{2m} \frac{1}{2^{2m-1}} \binom{2m}{m-1} = \sum_{m=1}^{\infty} \frac{\nu_{\text{MA}}^{2m} \alpha^{(2m)}(\nu_{\text{center}})}{2^{2m-1}(m-1)!(m+1)!} \,. \tag{10}$$

The so-called second harmonic spectrum of the absorption feature $\alpha(\nu)$ can now be obtained by measuring the coefficient c_2 with several different center frequencies and by plotting the coefficients as a function of the center frequency, which is illustrated in figure 3 (an animation). In practice, the coefficient c_2 is obtained by performing Fourier transform on the acoustic signal $\alpha(\nu_{\text{idler}})$ and looking for the second harmonic component in the obtained acoustic spectrum or by demodulating the acoustic signal with a lock-in amplifier.[42] The latter method was used in the radiomethane measurements, and details of the photoacoustic setup are discussed in section 3.2.

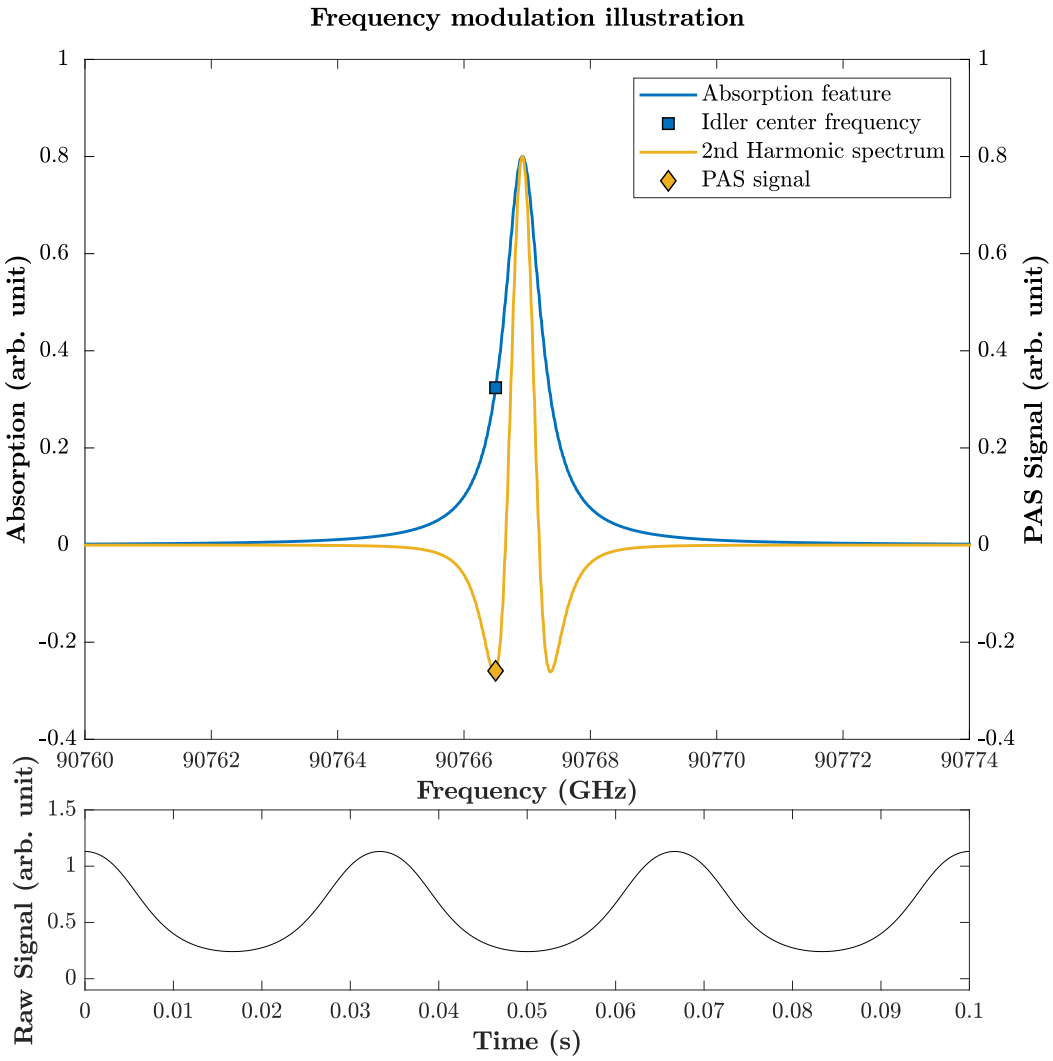

Figure 3: An animation illustrating the second harmonic spectrum (yellow curve) of a Lorentzian lineshape function[43] (blue curve). In this example, the MA and the full width at the half maximum of the line is 700 MHz (a typical width of the $^{14}CH_4$ lines), and the MF is 30 Hz. The bottom part of the figure shows the raw PAS signal that is demodulated at 60 Hz frequency to obtain the second harmonic coefficient at each center frequency (indicated by the markers in the figure).

As stated earlier and as can be seen from equation (10), the second harmonic spectrum is related to the different order derivatives of the actual absorption spectrum, which helps to reduce the effect of unwanted background absorption signals. Similarly, one could also measure some higher order harmonic of the absorption feature, but this would reduce the overall measured signal strength.[44] Also note that the shape of the second harmonic spectrum depends on the MA used. As a rule of thumb, the photoacoustic signal is maximized when the MA is of the same order than the full width at the half maximum (FWHM) of the transition peak to be measured.[44] However, in the radiomethane measurements, strong enough second harmonic signal was obtained with an MA of 0.243 GHz, while a typical linewidth of the measured transitions in the used pressure (200 mbar) was 0.70 GHz. Figure 4 (an animation) illustrates the effect of MA on the linewidth. As the illustrated line widens with increasing MA, smaller than "optimal" MA can aid in resolving partially overlapping lines.

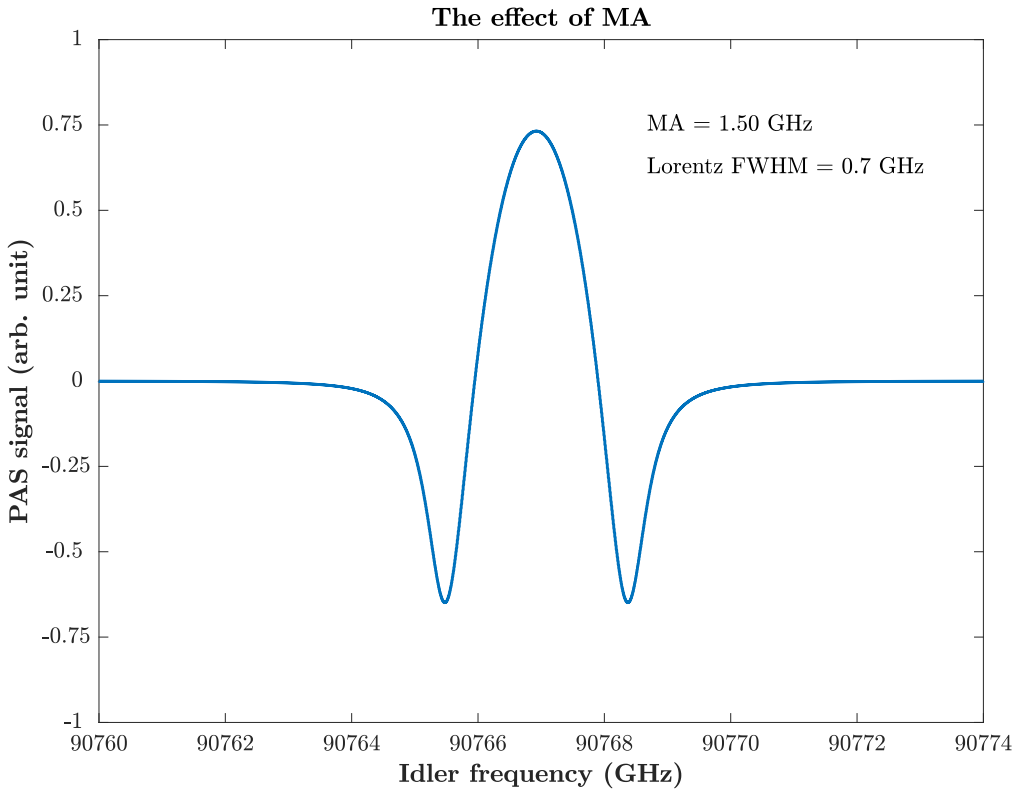

Figure 4: An animation illustrating the effect of MA on the second harmonic spectrum of a Lorentzian lineshape function[43] whose full width at the half maximum is 700 MHz. Note how the width and the strength of the second harmonic feature changes as a function of MA.

Figure 5 is an example of a Fourier transformed output signal of the photoacoustic instrument used in the radiomethane measurements (section 3.2). The red line indicates the chosen MF of 30 Hz. Increasing MF to 70 Hz (yellow line) had no clear advantage in signal to noise ratio supposedly due to the decrease in the response of the instrument[45] being compensated by the decrease in flicker noise. This example justifies the chosen 30 Hz MF.

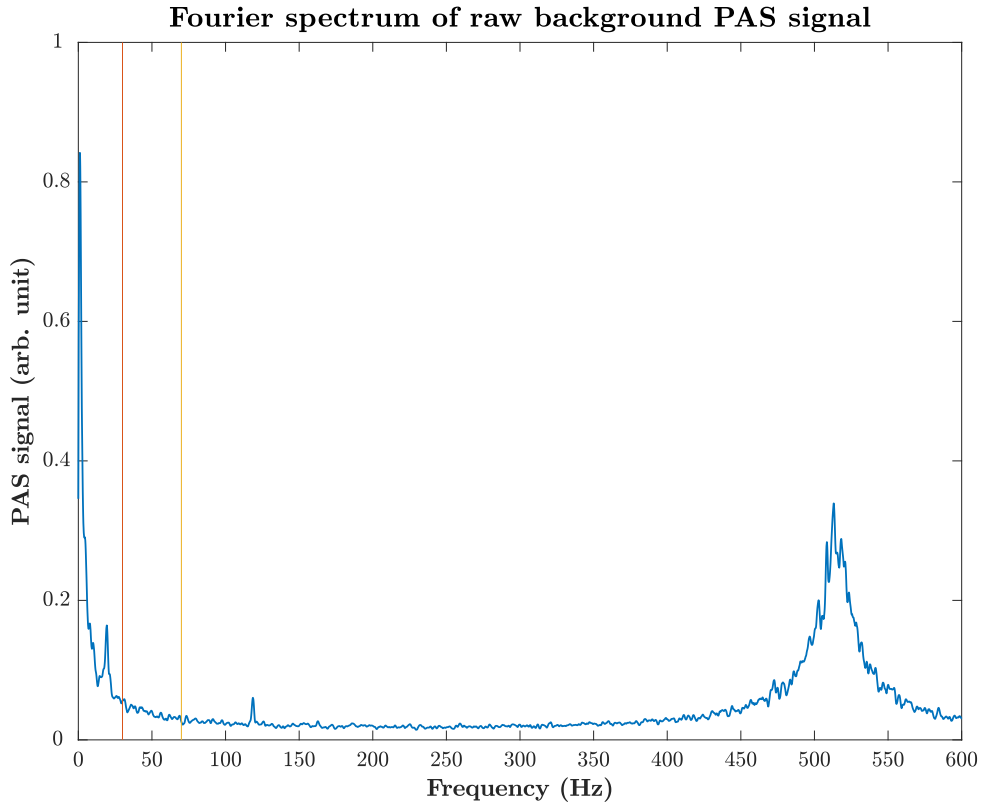

Figure 5: An example of a measured raw background signal of the photacoustic instrument. There are 50 spectra averaged in the shown Fourier spectrum. The red line marks the chosen 30 Hz MF and the yellow line marks the tried 70 Hz MF that had negligible effect on the SNR.

The most important consequence of the discussion in this section is that by measuring a second harmonic spectrum, information about the actual unknown absorption spectrum can be deduced: In the radiomethane measurements discussed in this thesis, a Voigt lineshape[46,47] (equation 11) for the absorption peaks was assumed. By defining an unknown scaling, line center frequency and linewidth parameters one can simulate the second harmonic spectrum for the function and use it as a fit model to obtain experimental values for the parameters defined.

$$V(\nu) = \int_{-\infty}^{\infty} G\left(\nu', \delta\nu_{\mathrm{G}}\right) L\left(\nu - \nu_0 - \nu', \delta\nu_{\mathrm{L}}\right) \mathrm{d}\nu' \,, \tag{11}$$

where $G(\nu, \delta\nu_{\mathrm{G}})$ is the Doppler lineshape[43] (equation (12), dominant in high temperatures and low pressures), and $L(\nu, \delta\nu_{\mathrm{L}})$ is the Lorentz lineshape[43] (equation (13), dominant in high pressures and low temperatures), ν_0 is the frequency of the peak maximum and $\delta\nu_j$ is the full width at the half maximum (FWHM) for the line shape with a label j. All of the linewidths considered in this thesis are of the FWHM quality although the half width at the half maximum (HWHM) quality is widely used in literature. The Voigt profile in itself is the convolution of these two line shapes and used when neither the Doppler nor Lorentz component of the linewidth is dominant.

The Doppler lineshape component is:[43]

$$G(\nu, \delta\nu_{\mathrm{G}}) \propto \mathrm{e}^{-\frac{4\ln(2)}{\delta\nu_{\mathrm{G}}^2}\nu^2}, \quad \delta\nu_{\mathrm{G}} = \frac{2\nu_0}{c}\sqrt{\frac{2N_{\mathrm{A}}k_{\mathrm{B}}T\ln 2}{M}}\,, \tag{12}$$

where c is the speed of light, N_{A} is Avogadro's number, k_{B} is Boltzmann's constant, T the temperature and M the molar mass of the species. The Lorentz component is:[43]

$$L(\nu, \delta\nu_{\mathrm{L}}) \propto \frac{1}{\nu^2 + (\frac{1}{2}\nu_{\mathrm{L}})^2}\,. \tag{13}$$

The second harmonic spectrum for a Voigt lineshape can be simulated with the method explained earlier in this section, but due to the integral definition of the Voigt profile, fitting using such an approach is time-consuming. Fortunately analytical solutions exist for the second Fourier coefficients of the Lorentz and Doppler lineshape functions, and they can be used to define the modulated Voigt lineshape:[37,48]

$$c_2(\nu_{\mathrm{center}}) \propto \mathrm{e}^{-2\frac{\delta\nu_{\mathrm{L}}^2}{\delta\nu_{\mathrm{G}}^2}\overline{\nu}_d^2} \otimes \left(2 + \frac{C_2 S_+ + D_2 S_-}{\sqrt{2}R}\right), \quad \begin{cases} C_2 & = -2 - \nu_{\mathrm{MA}}^2/\delta\nu_{\mathrm{L}}^2 + 2\overline{\nu}_d^2 \\ S_\pm = & \sqrt{R \pm \mathcal{M}} \\ R = & \sqrt{\mathcal{M}^2 + 4\overline{\nu}_d^2} \\ \mathcal{M} = & 1 + \nu_{\mathrm{MA}}^2/\delta\nu_{\mathrm{L}}^2 - \overline{\nu}_d^2 \\ D_2 = & -\mathrm{sign}(\overline{\nu}_d) 4\overline{\nu}_d \\ \overline{\nu}_d & = \left(\nu_{\mathrm{center}} - \nu_0\right)/\delta\nu_{\mathrm{L}} \end{cases}, \tag{14}$$

where $\otimes$ denotes convolution.

3. Experimental setup

3.1. The constructed OPO

Figure 7 shows the experimental design of the OPO constructed for the radiomethane measurements. The linearly polarized output beam (the pump beam, output power up to 15 W at 1064 nm) of an ytterbium amplifier (IPG YAR-15K-1064-LP-SF, referred to as "laser amplifier" from now on) is seeded with a single frequency fiber laser (output power roughly 10 mW at 1064 nm; NKT N80-130-21 Koheras). The beam is directed through a telescope (Thorlabs LC1715-C and LA1433-B with 10 cm separation) and focused (Thorlabs LA1708-B) into a 44 mm long and 1 mm thick anti-reflection coated (reflectivity $R < 0.5$ % at 1064 nm, < 0.5 % at 1450–1700 nm and < 10 % at 3000–3500 nm, as reported by the manufacturer) nonlinear crystal (HCP 5 mol % MgO doped periodically poled $LiNbO_3$). The crystal is mounted on a translational stage that is equipped with Peltier elements, which are controlled by a temperature controller (Newport 350B). The diameter of the laser amplifier output beam was assumed to be 0.9 mm, the value specified by the manufacturer. This diameter results together with the chosen telescope and beam focusing optics in a focusing parameter of about 1.9 for the pump beam in the crystal (equation (2)).

A bow tie resonator was constructed around the nonlinear crystal in an insulated aluminum box covered with a lid to reduce thermal disturbances and isolate the OPO from mode hop inducing air currents;[21] the whole experimental setup was constructed on an optical table floating on air cushions, which reduces mechanical disturbances. The resonator consists of two custom made (Quality Thin Films Inc.) CaF_2 concave–convex mirrors (the mirrors closest to the crystal) with a 100 mm radius of curvature. The outer surfaces of the mirrors are anti-reflection coated ($R < 0.25$ % at 1063–1065 nm, < 1.0 % at 1550–1750 nm and 2700–3500 nm) and the inner surfaces are coated to reflect > 99.9 % at 1550–1750 nm and < 3.0 % at 1063–1065 nm and 2700–3500 nm. The other two mirrors are plane mirrors (Thorlabs BB1-E04). The poling periods of the crystal and the available temperature tuning range together with the crystal and mirror coatings results in the signal beam wavelength to be roughly in the range of 1550–1760 nm, which corre-

sponds to the idler wavelength range of 2700–3400 nm (2940–3710 cm^{-1}). The frequency (wavelength) tunability of the OPO and methods for frequency (wavelength) tuning are discussed in more detail in the next subsection.

The optimal dimensions of the resonator (to result in the desired focusing parameter of 1.9 also for the signal beam) were deduced using the ABCD-matrix method:[49] based on figure 6, the optical curved mirror spacing ($2d_1$) of 110.8 mm was used, and the distance from the curved mirrors to the secondary focus between the plane mirrors (d_2) was chosen to be 282.3 mm. The total resonator length is then optically 675.4 mm, but the physical length of the resonator was set to 698.8 mm in order to take into account the different refractive index of the crystal.[50] It follows that the FSR of the resonator is roughly 400 MHz when taking into account the different refractive index of the crystal. The resonator was aligned and optimized in the 30.5 μm poling period (see subsection 3.1.1) at 90 °C crystal temperature corresponding to a signal wavelength of 1570 nm (3300 nm for the idler). Also note (figure 7) the 2 mm thick YAG etalon (40 GHz FSR) placed inside the resonator at the secondary focus. In addition, the etalon angle can be tuned electrically.

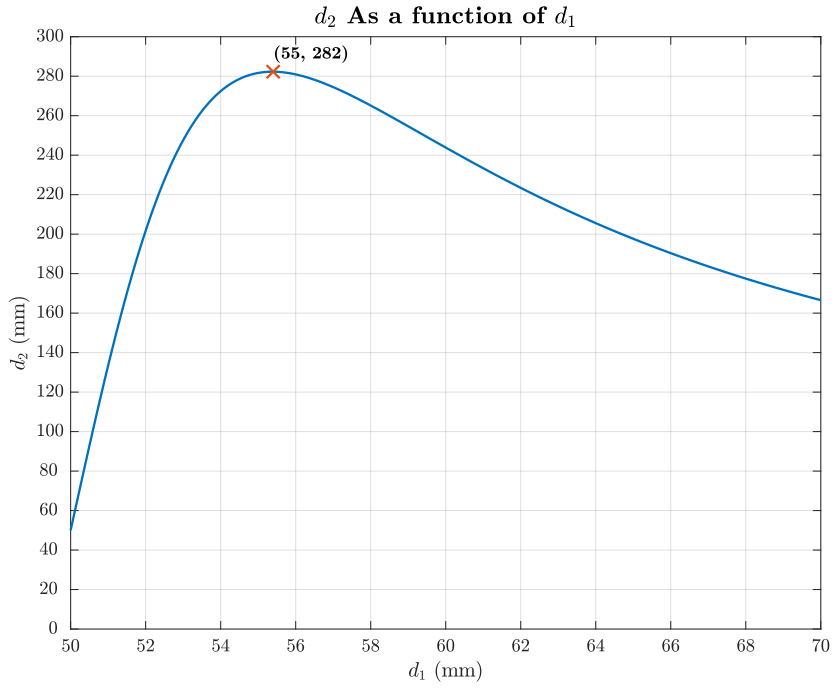

Figure 6: The distance from the curved mirrors to the secondary focus between the plane mirrors (d_2) as a function of the (optical) distance from the center of the crystal to the curved mirrors (d_1) resulting in the desired focusing parameter (1.9) for the signal beam. The curve was deduced with the ABCD-matrix method,[49] and the red cross indicates the optimal mirror separations in the sense that imprecise placing of the mirrors will have the smallest effect on the focusing parameter.

The OPO output beams (mainly idler and residual pump) that pass through the second curved mirror are guided through a focusing lens (LA5012-D) and a beam splitter (Quality Thin Films Inc., CaF_2, $R > 99.9$ % at 1064 nm and 1550–1750 nm and transmission $T > 95$ % at 2700–3500 nm) to refocus the beams and filter out the residual pump and signal beams. The residual pump and signal beams are then blocked. Some of the output idler power is sampled with a wedged CaF_2 plate (see figure 14 in section 3.2) and the first reflection from the plate is guided, after sufficient enough attenuation, to a wavelength meter (Bristol 771B), while the second reflection is aligned after sufficient enough attenuation into a photodetector constructed in our lab from a Hamamatsu P13243-011MA InAsSb photovoltaic detector; for the power characterization discussed in section 3.1.3, the idler power was measured with a Thorlabs S310C thermal detector head (connected to a Thorlabs PM100D console) after the CaF_2 plate. The idler beam, whose linewidth is in the order of 1 MHz,[51] is used as a light source in the photoacoustic experiment whose experimental design is discussed in more detail in section 3.2. The following subsections concentrate on the characteristics of the OPO.

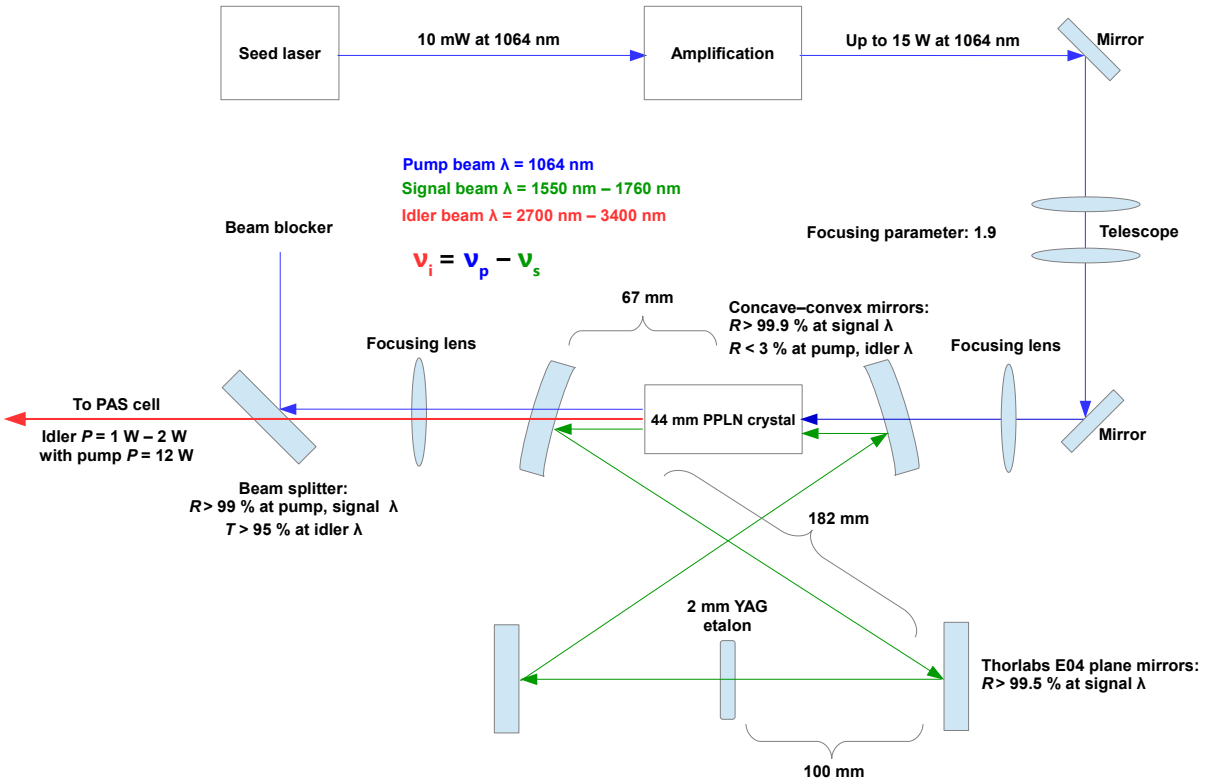

Figure 7: The experimental design of the OPO constructed for the $^{14}CH_4$ measurements. Not all of the details mentioned in the text are included in the figure.

3.1.1. Frequency tuning

As the OPO is used in a spectroscopic application, in this case, measuring the absorption spectrum of radiomethane, one should be able to tune the frequency of the idler beam. This can be done in several steps with the constructed OPO. First, the frequency can be tuned coarsely by choosing a poling period which changes the phase matching condition (equation (4)) and which is done in practice by physically moving the crystal horizontally on a translational stage so that the pump beam will penetrate through a different region in the crystal. The designed OPO works with three different poling periods (see figure 8) as allowed by the mirror and crystal reflectivities. Next, the frequency can be tuned more finely by changing the crystal temperature, which is why the crystal stage is equipped with Peltier elements that are controlled with a temperature controller: changing the temperature of the crystal influences the poling period length via thermal expansion and, on the other hand, the refractive indexes[29] of the crystal will change, which also affects the phase matching condition (equations 3 and 4). Finally, the idler frequency can be even more fine-tuned by tuning the frequency of the pump beam and this is what is ultimately done when measuring over an absorption feature: A certain poling period and temperature are chosen as to effectively fix the frequency of the signal beam circulating inside the resonator. When the signal frequency is fixed, changing the pump laser frequency will be observed as a simultaneous change in the idler frequency as predicted by equation (1) – the fine tuning of the idler beam and the actual scanning procedure of the idler via pump frequency scanning is discussed in more detail in subsection 3.1.2.

Figure 8 illustrates the frequency tunability of the OPO. As mentioned, the OPO works in three different poling periods (31.5 μm, 31.0 μm and 30.5 μm) allowed by the mirror reflectivities and the crystal coatings. The OPO was usually operated at temperatures between 30 and 110 °C (but at about 115 °C for measuring the R(7) transitions of radiomethane discussed in appendix E) to reach the different frequency ranges depicted in the figure; it was noticed that one degree change in the crystal temperature results roughly in a 50 GHz change in the idler frequency, but the value of course varies to some extent depending on the actual temperature and poling period.

The Peltier elements used in the setup were not trusted to withstand much higher temperatures than the limit mentioned above and this limitation in temperature tunability results in some unreachable frequency ranges, for example, there is a frequency gap of about 2500 GHz (83 cm^{-1}) between the second and third poling periods – to achieve continuous frequency tuning across all poling periods, the temperature tunability should be increased by several tens of degrees Celsius as can be estimated based on reference 52 for instance. The limited temperature tunability affected the radiomethane measurement to some extent, in other words, there is a limit to how many transitions in the frequency range of interest (84000–96000 GHz $\widehat{=}$ 2800–3200 cm^{-1} $\widehat{=}$ 3100–3600 nm) could be measured. Nonetheless, many transitions of radiomethane, some of which have never before been reliably assigned, could still be measured and much new spectral information on $^{14}CH_4$ was obtained as is discussed in detail in section 4.

Note that in figure 8, the third poling period is emphasized with a polynomial fit to the measurement points: only the 30.5 μm poling period was used in the actual radiomethane measurements, and the fit was used to estimate the correct temperatures for measuring each of the frequency ranges of interest (*i.e.* the frequency ranges containing the radiomethane lines of interest explained in section 4). Because only the third poling period was used, only that poling period is discussed in detail in the following subsections in terms of the OPO behaviour. Nevertheless, this section demonstrates that the OPO constructed in this thesis work could also be used for measuring species other than radiomethane even in frequency ranges that were not used in the $^{14}CH_4$ measurements.

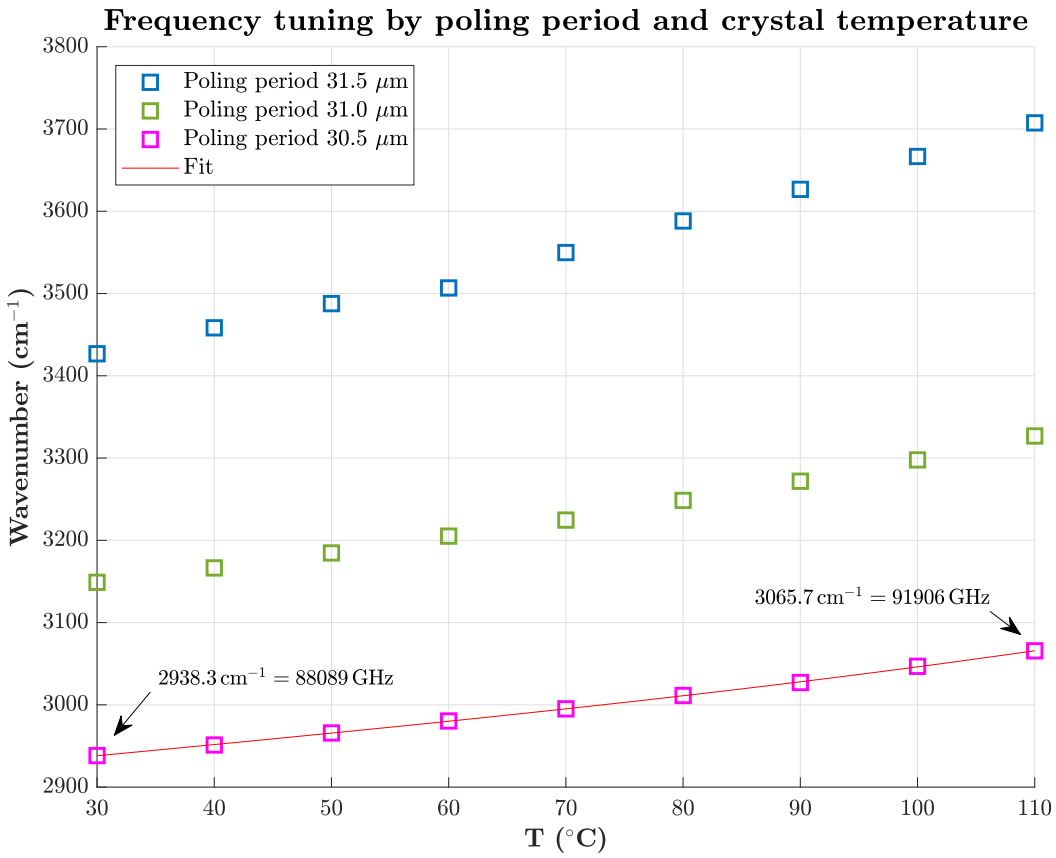

Figure 8: Illustration of the different frequency ranges available for the OPO: bridging the few frequency gaps evident from the figure would require increasing the temperature tunability of the OPO by several tens of degrees as explained in the text. The red line is a polynomial fit to the 30.5 μm poling period data. It was used to estimate the correct temperatures for reaching the frequency ranges of interest.

3.1.2. Laser piezo PID scanning and mode hop behavior

As explained in subsection 3.1.1, a scan over an absorption feature is executed by choosing a certain poling period and a crystal temperature, which will effectively fix the signal beam frequency. When the signal frequency is fixed, one can tune the idler frequency by tuning the pump laser frequency: the frequency of the seed laser (NKT N80-130-21 Koheras) that is used in the OPO setup can be manipulated by changing the voltage applied to the piezo elements of the laser. The voltage signal is generated with a digital-to-analog converter (National Instruments USB-6008 DAQ) controlled via LabVIEW and fed through a low-pass filter (5–10 Hz cut off frequency) and a signal mixing box that is used to add the modulation signal (section 2.2) to the DC signal. This sum voltage signal is amplified (Piezomechanik Gmbh SVR 150/3) before feeding it to the laser piezos. As a result,

the pump frequency can be tuned roughly by 60 GHz. This tunability was sufficient for measuring the radiomethane transitions of interest (section 4) at each chosen crystal temperature, because a common measured spectrum was usually less than 20 GHz wide.

As discussed in section 2.1, the OPO can be thought to start to oscillate in a resonator mode closest to the gain maximum (figure 1), in other words, in a resonator mode corresponding to minimum losses. Due to external interferences, temperature drifting and the possible unambiguity of the optimal resonator mode, mode hopping can (will) occur. To reduce this mode hopping, an etalon was placed inside the OPO resonator, as is commonly done.[20] Figure 9 shows an example of the behaviour of the designed OPO without an etalon. Before the measurement, the OPO had been oscillating for a long time, but as can be seen from the figure, even after this stabilization time the OPO does not remain in one resonator mode for long periods of time, but rather, it mode hops quite randomly. The possible mode hops seem to be resonator mode hops (about 400 MHz) and mode hops in the magnitude of 1–10 GHz.

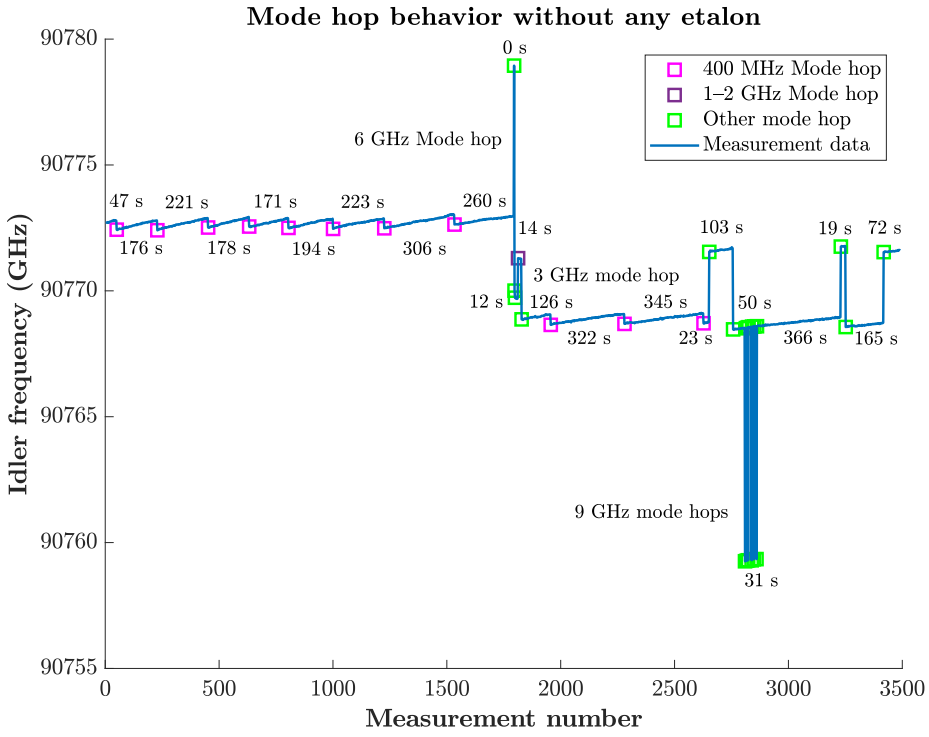

Figure 9: Illustration of the OPO behaviour without the etalon. The different coloured squares indicate mode hops, and the labels indicate the time between the different mode hop events. In this measurement the OPO had been oscillating for a long time before starting the measurement. The total measurement time in the figure is about 20 min.

The FSR of the etalon used to try to prevent these mode hops is about 40 GHz (figure 1). Figure 10 illustrates the behaviour of the OPO on start-up with the etalon placed inside the resonator. At first, the OPO mode hops a few times in large 40 GHz frequency steps but stabilizes after a few minutes making fewer and fewer hops. These 40 GHz frequency steps correspond to mode hops between adjacent etalon transmission maxima and the net increase of the idler frequency is due to the signal gain profile migrating to lower frequencies as the crystal (beam volume) temperature increases prior to stabilization.[21,50] An another type of mode hop that the OPO is able to make despite the etalon is a resonator mode hop (about 400 MHz). In general however, the number of mode hops and the variety in the magnitude of the possible mode hops is substantially reduced, and the OPO may stay in one mode for multiple minutes.

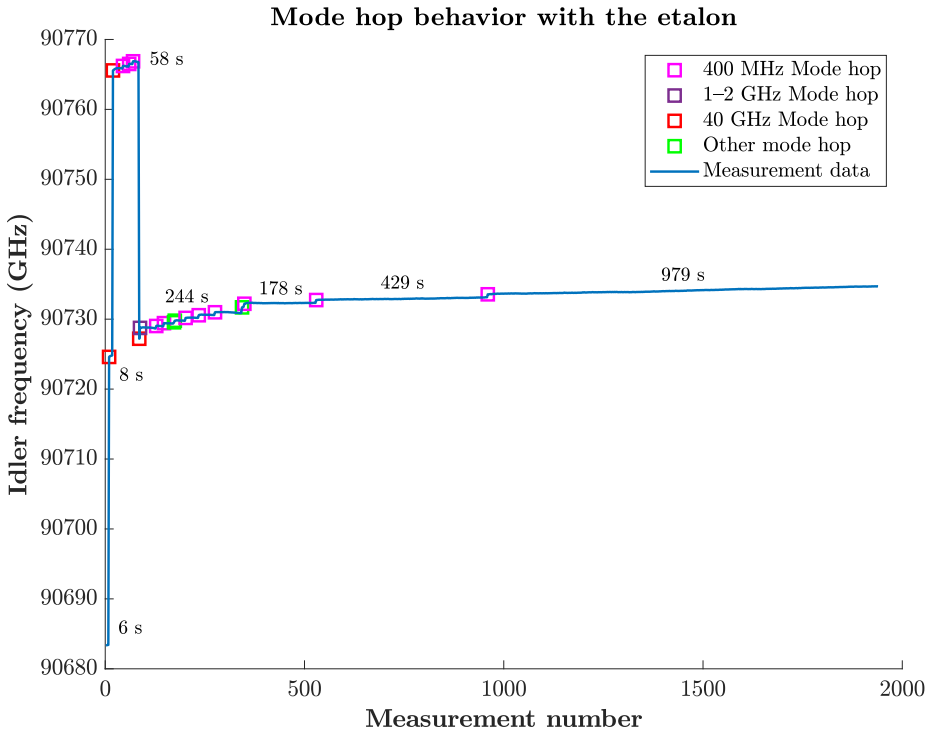

Figure 10: Illustration of the OPO behaviour with the etalon placed inside the OPO resonator. The different coloured squares indicate mode hops, and the labels indicate the time between the different mode hop events. This measurement starts right after the OPO has started to oscillate. The total measurement time in the figure is about 20 min. Note the upwards frequency drift even after the OPO has stabilized.

The behaviour depicted in figure 10 is usual for the OPO designed, but the example is still quite an ideal case: even after stabilization the OPO might sometimes experience a large 40 GHz mode hop, and resonator mode hops are still relatively common as is seen

in the figure. The reason for this residual mode hopping is presumably the slow upwards drift in the idler frequency evident from the figure, which is probably due to slow thermal expansion of the OPO resonator. This results in the oscillating mode drifting towards higher losses on the net gain curve (figure 1) and increasing the probability of a mode hop. These mode hops could probably be prevented for example by placing a piezo element on one of the OPO resonator mirrors and implementing a locking scheme to compensate for the signal frequency drift by adjusting the resonator length, as described for example in reference 53.

However, a totally different approach to manage the mode hops was implemented: The actual laser piezo scanning was executed using a proportional–integral–derivative controller (PID-controller) in LabVIEW. That is, the idler frequency was referenced to the wavelength meter used (Bristol 771B) and the scanning was executed by giving the program a frequency setpoint that it tried to reach by controlling the voltage fed into the laser piezo elements. Only after the setpoint was reached within a user defined tolerance was the measurement point approved and a new setpoint given; an ideal case (*i.e.*, a mode hop free case) of such a scan is illustrated in figure 11.

The PID idler frequency scanning was very useful, because even if a mode hop occurred, the PID-controller automatically tried to adjust the idler frequency back to the desired frequency before continuing the scan (figure 12). The trade-off of this method is the long measurement times: the measurement cycle of the wavelength meter is as long as one second and it usually takes several measurements to reach the current setpoint especially if a mode hop happens during a scan. For example, the 55 GHz scan depicted in figure 12 took about twenty minutes when the resolution was 500 MHz – note that a resolution of 50 MHz was used in the actual radiomethane measurements and despite that the measured spectral ranges were usually less than 20 GHz wide, the measurement time of one spectrum could sometimes be over an hour! Furthermore, even though a mode hop occurring during scan did not usually ruin the measurement, the occasional sudden idler power changes evident also in figure 12 did in some cases produce transients in the measured spectra, see for example section 4.2. It should also be mentioned that the etalon angle was sometimes needed to be adjusted during a scan to induce a mode hop if the DAQ voltage tunability was not sufficient to reach the desired setpoint after a large mode hop.

In conclusion, even though the PID scanning was convenient (and the measured spectra have a clean and equidistant frequency axes as illustrated in the result sections later in this thesis), a long term solution for the scanning procedure would be to (also) implement the above-mentioned locking scheme to compensate for the signal frequency drift with a piezo element attached to one of the OPO resonator mirrors. This would hopefully prevent mode hopping entirely, lead to somewhat shorter measurement times and minimize unnecessary power fluctuations that might affect the quality of the measured spectra.

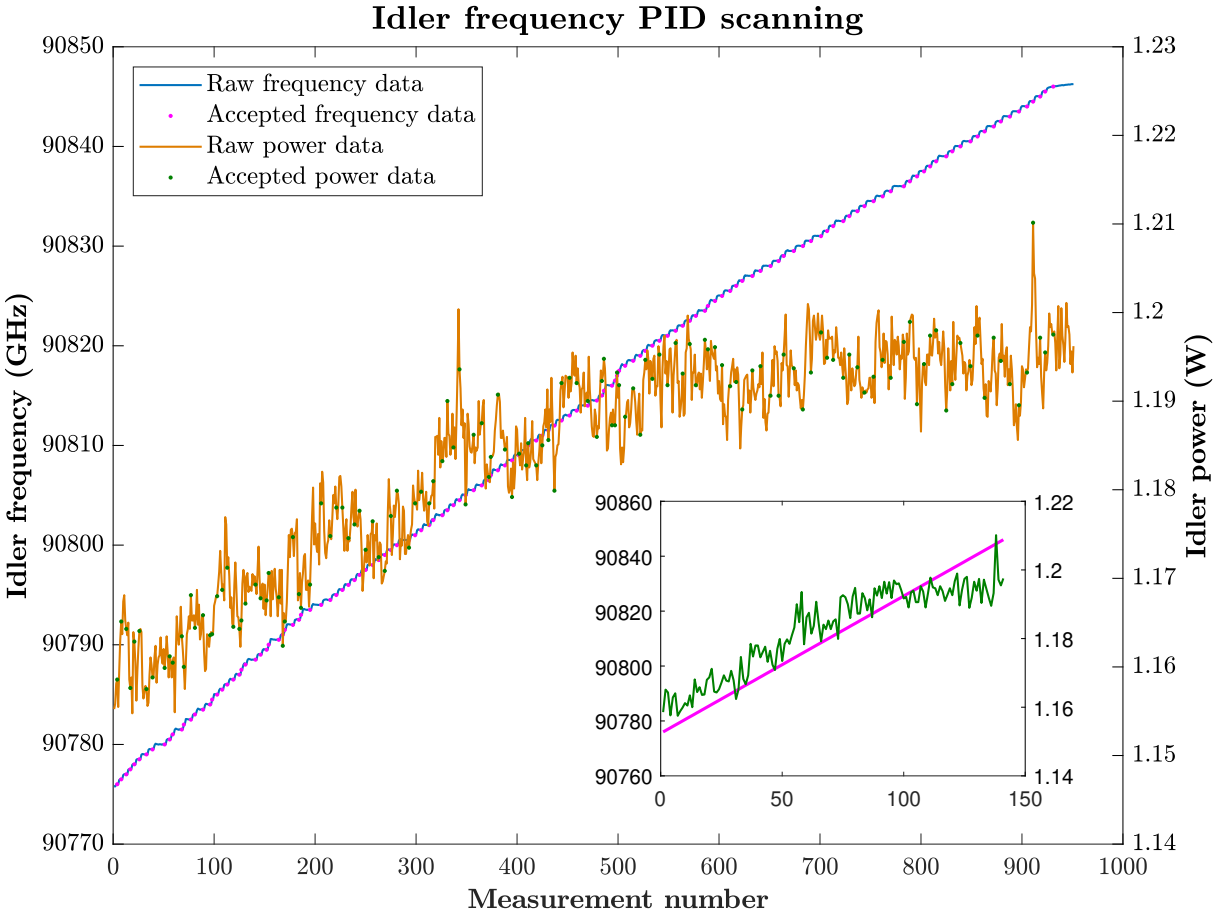

Figure 11: An example of an ideal laser piezo PID scan. The inset shows only the accepted frequency and power data, *i.e.* the datapoints that correspond to measurements close enough to the specified setpoint. The power (right vertical axis) has been measured with the Thorlabs thermal detector head after the wedged CaF_2 plate (figure 14). Note that even though the pump frequency tunability is roughly 60 GHz as mentioned, the total frequency scan width is 70.5 GHz in this measurement due to the previously mentioned upwards idler frequency drift. The standard deviation of the power data is only about 1 % with respect to the average power.

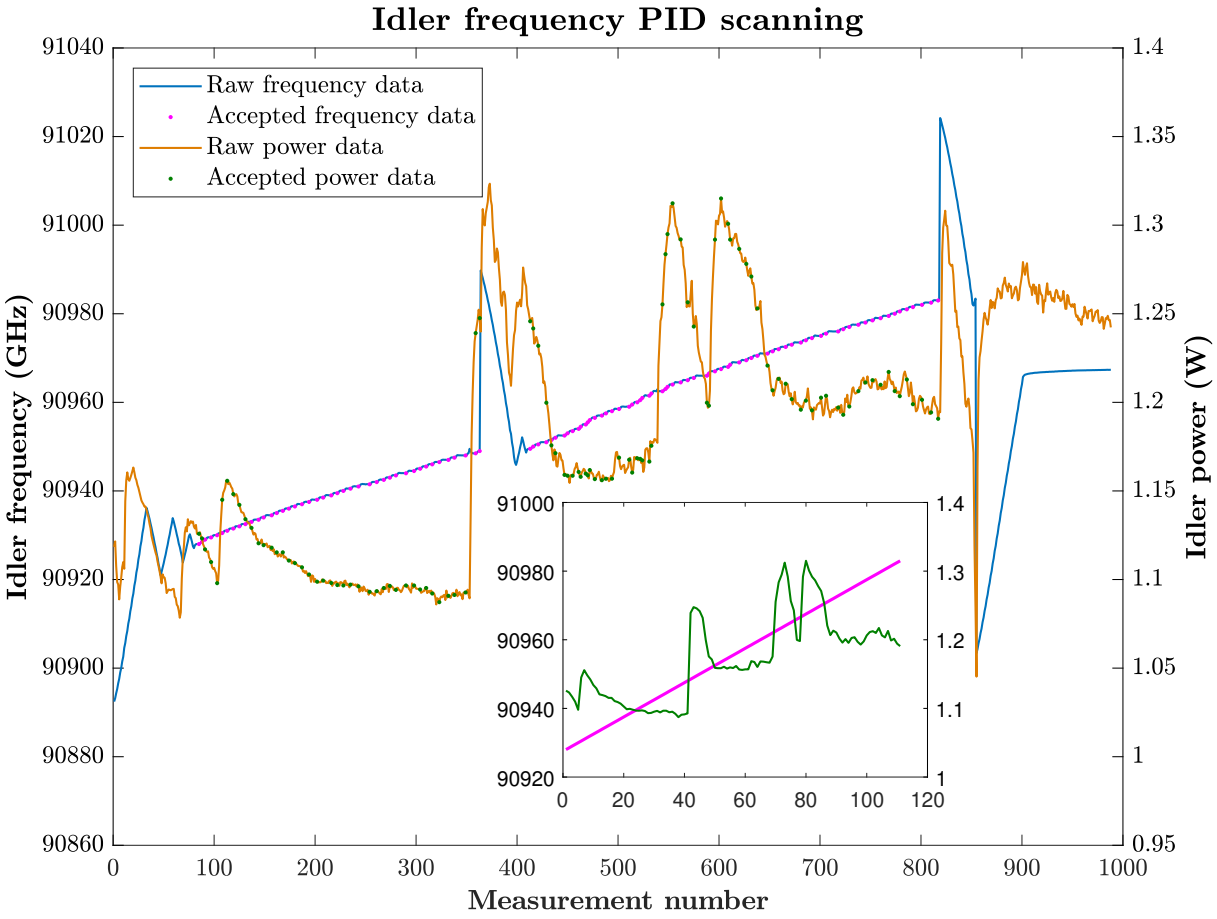

Figure 12: An example of a not so ideal laser piezo PID scan. The inset shows only the accepted frequency and power data, *i.e.* the datapoints that correspond to measurements close enough to the specified setpoint. Note the long recovery times after the large 40 GHz mode hops. The zigzagging in the beginning of the measurement is due to the first setpoint being far in frequency from the initial stabilized idler frequency before the scan was initiated. The total frequency scan width is only 55 GHz in this measurement, and the standard deviation of the power data is about 6 % with respect to the average power.

3.1.3. Output idler power

The power characteristics of the constructed OPO are briefly presented in this subsection. Figure 13 shows the idler power as a function of crystal temperature in the 30.5 μm poling period with the etalon placed inside the resonator. The pump power, defined as the output power of the laser amplifier measured by the amplifier itself, is 12 W and this pumping level was also used in the actual radiomethane measurements. The left vertical axis in the figure corresponds to the measured power (Thorlabs S310C thermal detector head) at the PAS cell entrance, and the right vertical axis describes the corresponding InAsSb detector signal (that is directly proportional to power) measured from the second reflection of the CaF_2 plate (section 3.2); the correspondence between the power measurements with the

two different methods is satisfactory and the data was used to roughly estimate the power in watts at the PAS cell entrance during the radiomethane measurements in which only the InAsSb detector was used to monitor power. It can be seen from the figure that the power level is always 1–2 W regardless of the crystal temperature. Note, however, that the power level stayed usually stable during a single spectrum measurement, see for example figures 11 and 12.

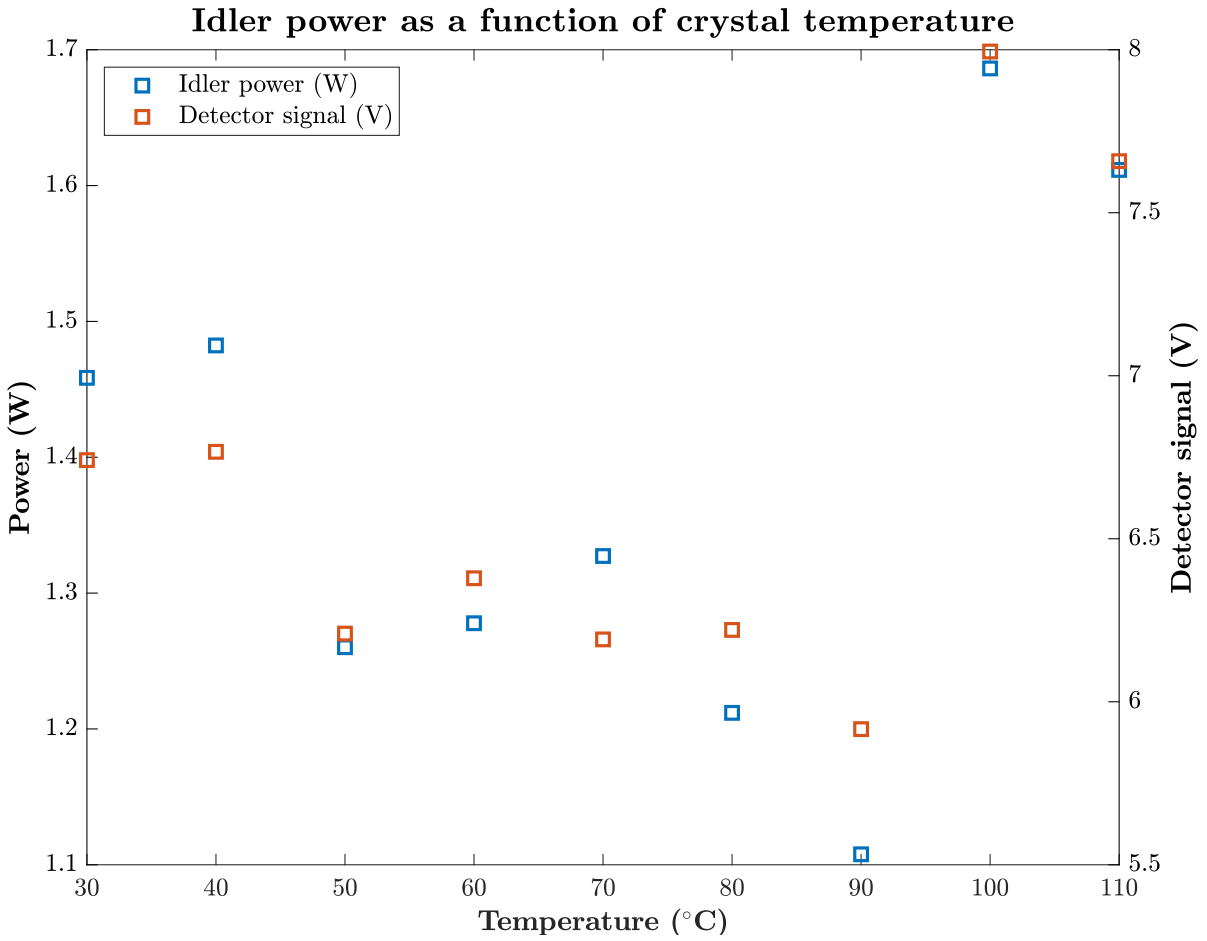

Figure 13: The correspondence between the power measured with the two different detectors as a function of crystal temperature in the 30.5 μm poling period. The left vertical axis corresponds to power measured with the Thorlabs thermal detector head at the PAS cell entrance, and the right vertical axis describes the corresponding InAsSb detector signal measured from the second reflection of the CaF_2 plate (the signal is directly proportional to power). This data was used to estimate the power at the PAS cell entrance during the actual radiomethane measurements in which only the InAsSb detector was used to monitor power: the conversion factor is about 0.206 W/V based on the figure with the standard deviation below 6 %.

The threshold of the OPO with the etalon placed inside the resonator is usually in the order of 10 W, which is a relatively high value for a well optimized OPO.[54] Even without the etalon, a typical threshold value for the 30.5 μm poling period was 8 W. One reason for these high thresholds could be the mirrors used: the mirror coatings have formed visible spots which might affect their reflectivities and increase losses in general. However, the threshold behaviour varies a lot and is strongly dependent on the crystal temperature and poling period: for example, the best threshold was about 3.5 W, which was obtained with the 31.0 μm poling period at 50 °C (not illustrated). As a side note, the maximum output idler power, about 2.5 W without the etalon, was still obtained in the 30.5 μm poling period with the highest possible pump power available (15 W).

Another interesting aspect of the OPO power behaviour is that the output idler power at the threshold was usually several hundred milliwatts! In addition, the OPO often stayed on even if the pump power was reduced under the original threshold, in other words, hysteresis[50] was detected. These phenomena imply that a thermal lensing effect[50] might be produced by the high power beams penetrating the crystal, which improves the overlap of the pump and signal beams leading to a higher efficiency of the nonlinear process. This would also explain why the output idler power is well above zero immediately after the OPO has started to oscillate, in other words, the threshold is decreased once the oscillation starts. The proposed thermal effects were not however studied any further and remain a hypothesis.

The high thresholds were not a problem for the measurements, because the OPO could always be turned on in the end and the oscillation remained stable with the 12 W pump power used in the measurements. In addition, despite the output powers are in general smaller with the etalon placed inside the resonator, the 1–2 W power levels obtained were enough for successful measurements, as will become evident in the following sections.

3.2. The photoacoustic setup and gas exchange system

As mentioned, the OPO designed and discussed in length in previous sections was used as a light source in a photoacoustic experiment to measure the anti-symmetric CH-stretching vibrational fundamental band ν_3 of radiomethane. This section concludes the description of the experimental setup used in the measurements.

The whole experimental setup is depicted in figure 14: the idler beam of the OPO, after sampling some power for frequency and power measurements as discussed in section 3.1, is aligned into a commercial photoacoustic cell (Gasera PA201) that utilizes the silicon cantilever technique mentioned in section 2.2. The raw photoacoustic signal is fed to a lock-in amplifier (Stanford SR830 DSP) that is used both to demodulate the photoacoustic signal and to generate the signal (30 Hz sine with an amplitude corresponding to 0.243 GHz) that modulates the idler frequency via modulating the pump frequency. The modulation signal is mixed with the laser piezo PID scanning signal and amplified before connecting it to the seed laser piezo elements, as explained in section 3.1.2.

The photoacoustic cell is kept at 25 °C temperature and it is connected to a gas exchange system also depicted in figure 14. The cell inlet and outlet as well as the vacuum pump connected to the cell outlet are controlled via LabVIEW (NI USB-6356 DAQ), the rest of the gas exchange system is controlled with manual valves. The nitrogen-based sample gas (Quotient Bioresearch) contains 1 ppm of radiomethane with 100 ppm of methane in total. Even though a sample gas with higher radiomethane concentration and lower amounts of $^{12}CH_4$ isotopologue would be more optimal for determining pure spectroscopic information, real field samples of radiomethane will have spectral interference from at least $^{12}CH_4$. The results of this thesis should therefore be useful for finding interference free radiomethane transitions for future applications.

The sample gas container is connected to a 6 mm stainless steel T-tube with manual valves and the other inlet is connected to a source of pure nitrogen used as a flushing gas. The outlet of the T-tube is connected with 6 mm Teflon tubing to the inlet of the photoacoustic cell that is equipped with a particle filter. The volume of the photoacoustic cell is about 8 ml and the volume of the entire gas system was estimated to be 35 ml.

Prior to measurements, the gas line was first flushed with pure nitrogen gas for several seconds and subsequently pumped to vacuum. Then, it was flushed with the sample gas and pumped to the measurement pressure of 200 mbar. After this, the cell inlet and outlet were closed as to isolate the cell during measurements. Note that the pressure is read with a pressure meter placed outside of the cell. However, it was concluded that the cell was indeed left roughly to the desired pressure during measurements; the cell was noticed to leak only 0.27 mbar/min in a separate test measurement, but because a measurement of one spectrum could take even an hour, this leaking probably lead to some pressure increase during the measurements. This variation in pressure was not taken explicitly into account, for example, in the determination of the linewidth uncertainties (section 4.1).

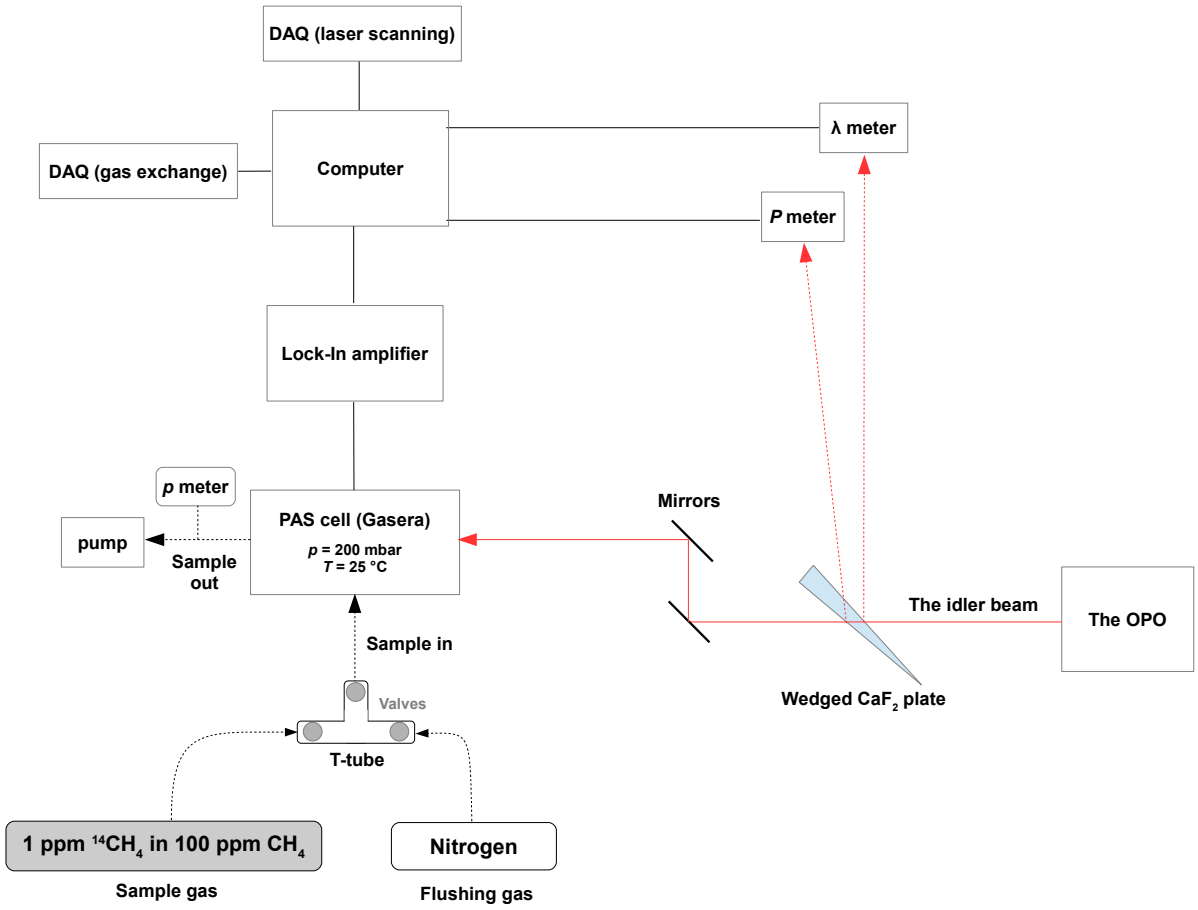

Figure 14: Illustration of the experimental setup used in the $^{14}CH_4$ measurements. Not all of the details mentioned in the text are included in the figure.

4. Measurements and results

The radiomethane measurements were conducted during two weeks. The experimental setup and the gas exchange procedure as well as the contents of the sample gas and the measurement conditions ($T = 25\,^{\circ}\mathrm{C}$, $p = 200$ mbar) have been discussed in the previous section. As explained in section 2.2, the measurements were based on photoacoustic spectroscopy and frequency modulation, and the section also discussed how to extract spectroscopic information from the measured spectra; note that the Doppler components of the Voigt line widths were always fixed to their theoretical values[55] during fitting (nonlinear Levenberg–Marquardt least squares fit), which is why only the (FWHM) results for the Lorentz components of the widths are presented. Normal methane and water transitions were also included in the fitting model where necessary. The fitting results for such peaks have been used to judge the accuracy of the determined radiomethane fit results, see for example subsection 4.2.

The basic theory of optical parametric oscillators has been covered in section 2.1 and the characteristics of the OPO that was constructed and used as a light source in the photoacoustic detection system has been discussed in detail in section 3.1: The OPO was pumped with 12 W pump power and the output idler power was always 1–2 W, but the power variation during a single spectrum measurement was usually only a few percent. Although all of the measured spectra have been normalized with the corresponding power spectrum (see appendix G for an illustration), the strength of the absorption peaks are not studied quantitatively. The resolution used in the measurements was 50 MHz and the width of a typical measured spectrum is under 20 GHz as already mentioned in the previous sections; the measurement of a single spectrum could take an hour.

Figure 15 illustrates which transitions of the anti-symmetric CH-stretching vibrational band ν_3 of $^{14}CH_4$ could be measured with the frequency tunability of the OPO (section 3.1.1). The blue spectrum is a HITRAN simulation[56] of the corresponding absorption band of $^{12}CH_4$, and the positions of the measured $^{14}CH_4$ transitions are marked with red lines in the figure. Note that the marked transitions have a tetrahedral splitting fine structure,[57] which makes the total number of measured lines to be 43. The results of the peak positions are tabulated in appendix A and the linewidths in appendix B.

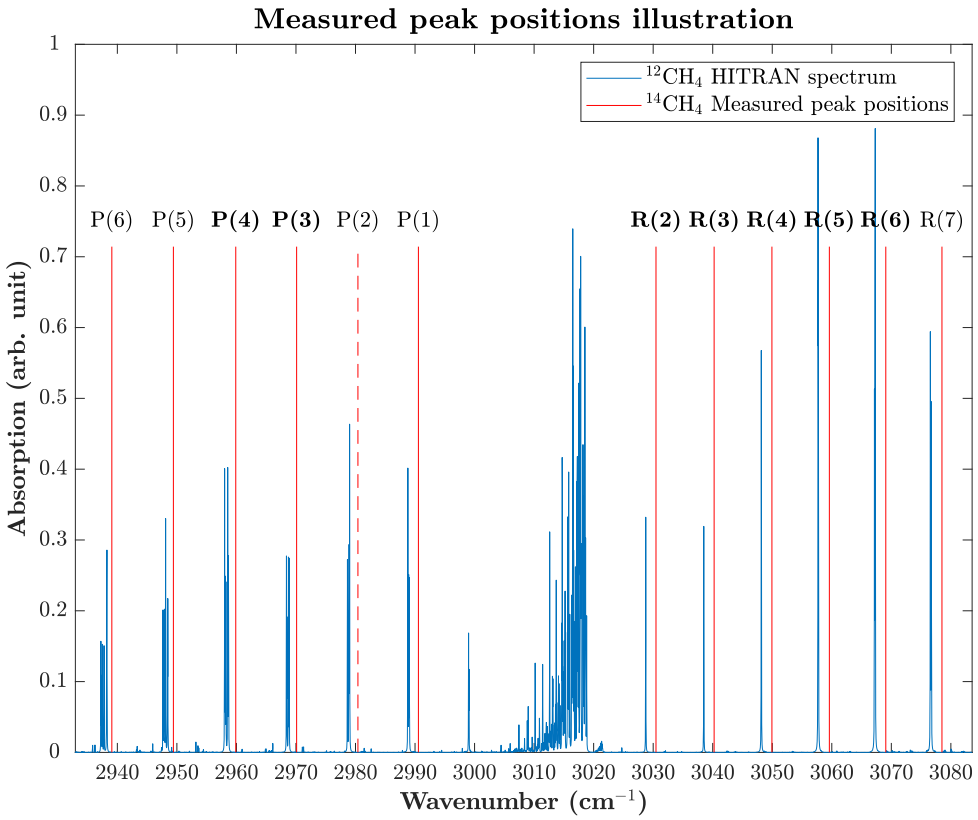

Figure 15: Illustration of the $^{14}CH_4$ transitions measured. The blue spectrum is a HITRAN simulation of $^{12}CH_4$ and the measured $^{14}CH_4$ peaks are marked with red lines. Note that the $^{14}CH_4$ lines have a tetrahedral splitting fine structure, which makes the total number of measured lines to be 43. The labels in bold mean that the corresponding transitions were also measured and reliably assigned by Karhu *et al.*[1] The dashed red line indicates that the P(2) transitions could not be reliably assigned due to major water interference.

The labels in bold in figure 15 mean that the corresponding transitions were also measured and reliably assigned by Karhu *et al.*[1] It can therefore be noted that several new lines have been measured in the work presented in this thesis. Moreover, the peak positions of the transitions could now be determined with improved accuracy and, for the first time, the widths of the measured lines were studied in detail. However, the dashed red line indicates that the two expected P(2) lines could not be reliably assigned due to major water interference (see appendix C). Also, measurement of the R(0) and R(1) transitions (expected roughly in the wavenumber range of 3010.1–3011.1 cm^{-1} and 3020.1–3021.1 cm^{-1}, respectively) was not even attempted due to major interference by $^{12}CH_4$ expected based on the simulation. In addition, the Q-branch was not studied in these measurements, but some features of the branch have been outlined in J. Karhu's doctoral dissertation.[58]

The lines were identified by simulating the second harmonic spectrum of water (whose concentration was estimated to be about 2.2 per mille based on data explained in appendix C), $^{12}CH_4$ (100 ppm), $^{13}CH_4$ (in its natural abundance with respect to the 100 ppm total concentration of methane) and $^{14}CH_4$ (1 ppm), whose spectrum was simulated based on the corresponding spectrum of $^{12}CH_4$ and equation (4.9) in J. Karhu's doctoral dissertation. The corresponding line positions, widths and relative strengths available in HITRAN[59] were used as an initial guess for the different fit parameters (for $^{14}CH_4$ lines, the initial guesses were the corresponding values of the corresponding $^{12}CH_4$ transitions). Note that the whole spectral region showed in figure 15 was not measured due to the long measurement times already discussed. Instead, only the spectral regions expected to contain $^{14}CH_4$ transitions of interest were measured.

Figure 16 shows an example of a spectrum simulation and it also shows the corresponding measured spectrum, the P(3) transitions discussed in detail in subsection 4.2. It can be noticed that despite the small, approximately 200 MHz offset discussed in subsection 4.1, the expected $^{12}CH_4$ lines are found in the measured spectrum. In addition, the relative heights of strongest lines in the spectrum match well with the expected $^{14}CH_4$ transitions, but the lines cannot be explained by constituents other than radiomethane. There is, however, a considerable, several gigahertz offset in the expected $^{14}CH_4$ peak positions, which is due to the crude model that was used to estimate the spectrum. The parameters of the model are updated based on the new data discussed in this thesis, see section 4.4.[†]

In the following subsections, the radiomethane measurement results are covered in detail, and the next subsection discusses the principles of uncertainty estimation for the determined line parameters. In subsection 4.2, the reproducibility of the measurements is considered as well as the effect of averaging and the credibility of the determined width parameters. In subsection 4.3, the R(3) line results are compared with the corresponding results in reference 1. See also the appendices in the end of this thesis, for they discuss many important details of the measurements and results.

[†]See also appendix H for a refined model of the ν_3 band.

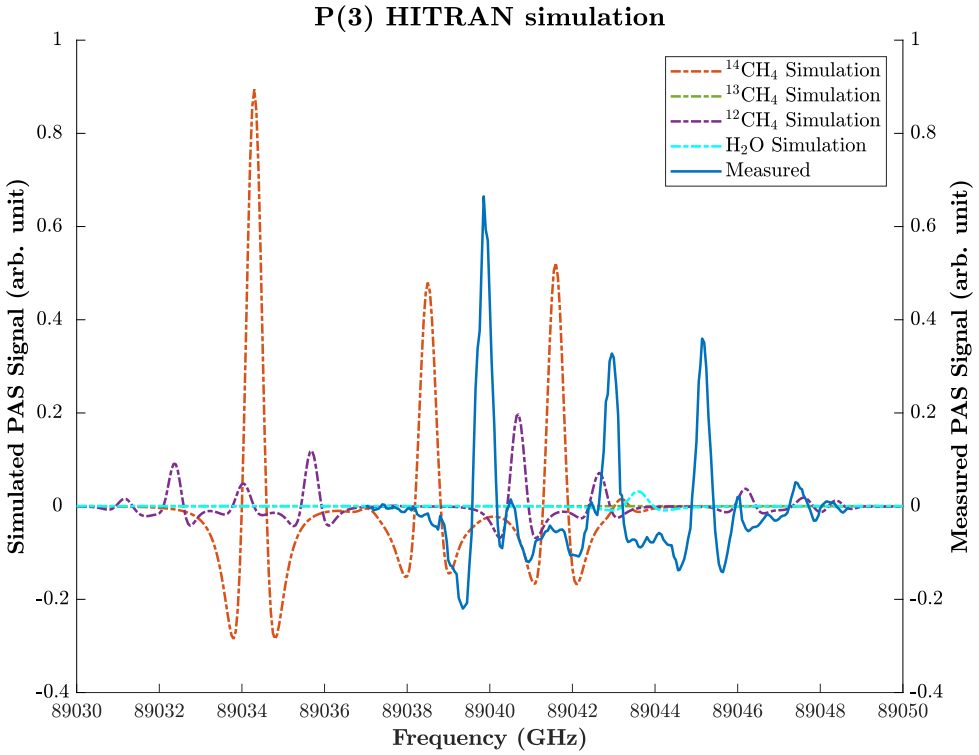

Figure 16: An example of a second harmonic spectrum simulation. This simulation was used to identify the peaks in the expected P(3) spectral region of $^{14}CH_4$. The actual measured spectrum of this region is also included in the figure. It can be noticed that the strong features in the spectrum can only be explained by transitions of $^{14}CH_4$ even though there is a considerable offset in the measured peak positions with respect to the expected peak positions. The reason for this is explained in the text. The $^{12}CH_4$ and water peaks are also shifted but only by 200 MHz, which is taken into account in the frequency axis calibration explained in the next subsection. Note also the modulation in the background of the measured spectrum. This background modulation is further discussed in subsection 4.2 and appendix G.

4.1. Uncertainty estimation

This subsection discusses the principles of uncertainty estimation for the determined peak parameters. As mentioned, only the peak centers and (Lorentzian FWHM) widths are studied quantitatively in this thesis. The sources of uncertainty considered in this subsection are the uncertainty resulting from fitting, the uncertainty from the frequency axis calibration and the uncertainty in the MA affecting the peak width results.

Considering the peak center uncertainties, it was noticed that the measured $^{12}CH_4$ and water peak center values differed by about 210 MHz on average from their corresponding HITRAN values,[59] probably due to non-perfect alignment of the OPO idler beam into the wavelength meter. This value was then used to calibrate the frequency axes in the measured spectra. More precisely, this offset has been taken into account in all tables

presenting the measured peak position results. However, in any figure illustrating the measured spectra, the horizontal axis has not been corrected with this value.

Figure 17 shows all of the peak center offsets of the $^{12}CH_4$ transitions that were measured and reliably fitted during the two weeks of measurements. The figure does not reveal any clear drift in the offset value between consecutive measured spectra as the offset may vary in a single spectrum as much as it varies during the whole two weeks of measurements. Two standard deviations (80 MHz) of the offset value were included as an estimate of the residual uncertainty in the peak positions due to the calibration.

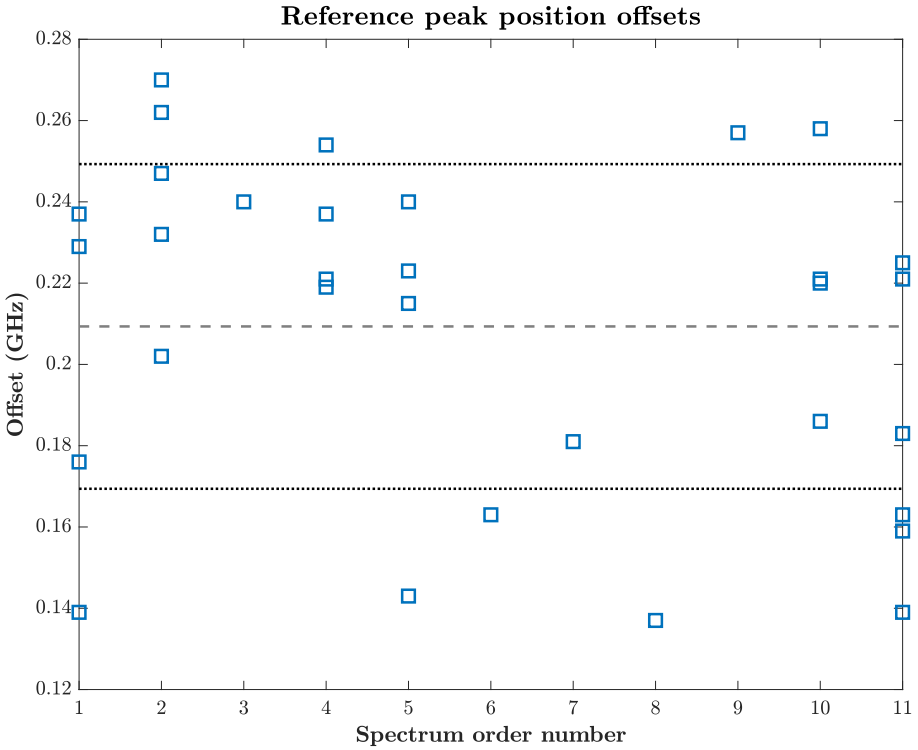

Figure 17: Differences of the measured and fitted $^{12}CH_4$ or water peaks from their corresponding HITRAN values. The horizontal axis indicates the measured spectra in measurement order, and the vertical axis indicates the actual offset values – if there are several points associated with the same horizontal axis value, it means that the measured spectrum contained several different $^{12}CH_4$ or water peaks that were fitted. The dashed line indicates the mean of the offsets and the dotted lines mark the one standard deviation of the offsets.

Overall, the uncertainties of the measured peak positions corresponding to 95% confidence intervals ($2\sigma_\nu$) were estimated using equation

$$2\sigma_\nu = \sqrt{(2\sigma_{\nu,\,\mathrm{fit}})^2 + (2s_{\mathrm{offset}})^2}\,, \tag{15}$$

where $\sigma_{\nu,\,\mathrm{fit}}$ is uncertainty obtained from the fit and s_{offset} is the standard deviation describing the uncertainty resulting from the calibration of the frequency axis as discussed

above. From now on, the quantities $2\sigma_{\nu,\,\mathrm{fit}}$ and $2s_{\mathrm{offset}}$ are referred to as "fit uncertainty" and "calibration uncertainty", respectively.

The calibration uncertainty majorly dominates the fit uncertainties: the fit uncertainty is below 45 MHz for all $^{14}CH_4$ peaks, the best fit uncertainty is 3 MHz (for one of the peaks in the averaged spectrum discussed in subsection 4.2) and the median is 7 MHz, whereas the calibration uncertainty explained above is about 80 MHz! Still, the improvement in the accuracy of the line positions compared to reference 1 is considerable as will be seen in the following subsections; the reproducibility of the measurements is discussed in more detail in subsection 4.2.

Considering the Lorentzian widths of the peaks, the uncertainties corresponding to 95% confidence intervals ($2\sigma_{\mathrm{L}}$) were estimated using equation

$$2\sigma_{\mathrm{L}} = \sqrt{(2\sigma_{\mathrm{L,\,fit}})^2 + (2\sigma_{\mathrm{L,\,MA}})^2}\,, \tag{16}$$

where $2\sigma_{\mathrm{L,\,fit}}$ is the uncertainty of the Lorentzian FWHM calculated[60] based on the Voigt FWHM fit uncertainty and a formula[61] approximating the Voigt FWHM. The minor error caused by the approximate formula is not considered.

The $2\sigma_{\mathrm{MA}}$ component in equation (16) is the estimated uncertainty resulting from the uncertainty of the used modulation amplitude ($\nu_{\mathrm{MA}} \pm 2\sigma_{\mathrm{MA}} = (0.24 \pm 0.02)\,\mathrm{GHz}$). It is clear from equation (10) and figure 4 that uncertainty in MA will affect the second harmonic spectrum and therefore the width fit parameters: increasing MA widens the second harmonic absorption peak, which has the effect that the width fit parameter will be smaller in compensation. Figure 18 shows how the Lorentzian FWHM behaves as a function of MA: the graph has been obtained by fitting with different modulation amplitudes (horizontal axis) to the averaged spectrum discussed in section 4.2 and the vertical axis in the graph describes the resulting Lorentzian width of the first $^{14}CH_4$ peak in the spectrum. It is clear that by assuming normally distributed MA, sampling the horizontal axis in figure 18 will result approximately in a normally distributed Lorentzian width for the peak under inspection (figure 19). Figure 19 has been obtained by fitting to the previously mentioned spectrum with modulation amplitudes sampled from a normal distribution defined by $\mu \pm \sigma \equiv \nu_{\mathrm{MA}} \pm \sigma_{\mathrm{MA}} = (0.243 \pm 0.010)\,\mathrm{GHz}$.

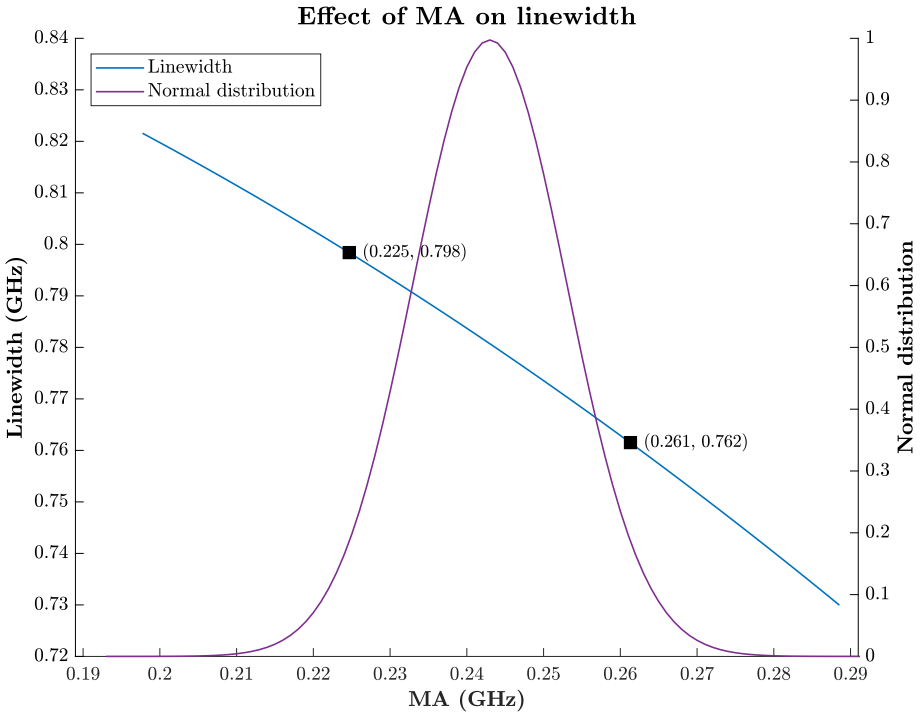

Figure 18: Illustration of the effect of MA on the fitted linewidth of the first $^{14}CH_4$ peak in the averaged spectrum discussed in section 4.2 (figure 23). The violet curve is a normal distribution defined by $\mu \pm \sigma = (0.243 \pm 0.010)$ GHz describing the assumed uncertainty in the MA and the blue curve shows the width fit result for the peak as a function of MA. The black squares indicate the widths that correspond to modulation amplitudes two standard deviations smaller and larger than the mean.

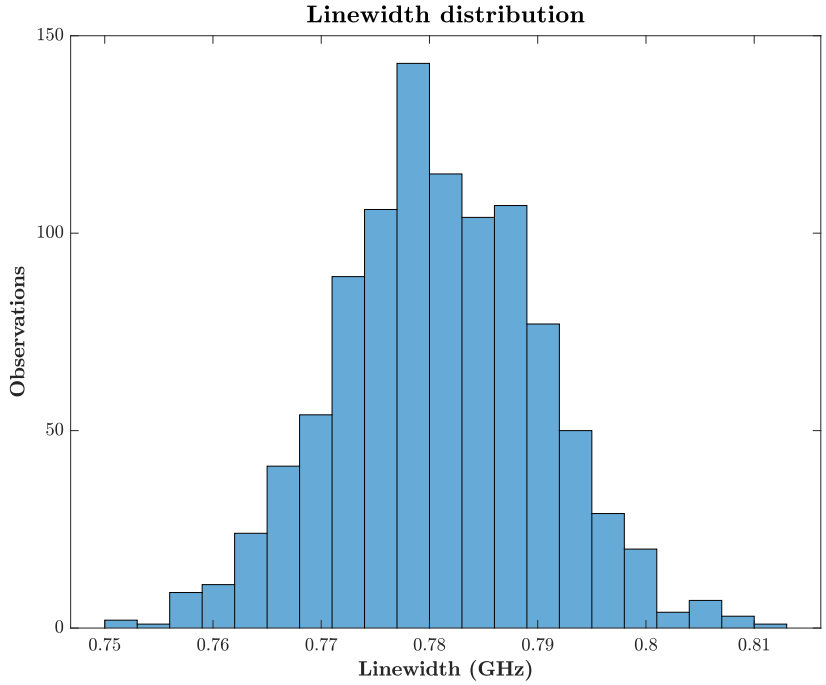

Figure 19: The width distribution for the first $^{14}CH_4$ peak in the averaged spectrum discussed in section 4.2 (figure 23). The distribution has been obtained by fitting with different modulation amplitudes sampled from a normal distribution defined by $\mu \pm \sigma = (0.243 \pm 0.010)$ GHz as explained in the text. The two standard deviations (19 MHz) of the distribution is well represented with the method explained in the text.

Two standard deviations of the distribution depicted in figure 19 corresponds to 19 MHz, which could now be identified as the uncertainty component $2\sigma_{\mathrm{L,\,MA}}$ for the examined peak. However, because this kind of analysis would be laborious to repeat for every measured spectrum, another approach is implemented: by noting the behavior of peak widths as a function of MA (figure 18), it can be assumed that a fit with one standard deviations greater MA than the mean will approximately result as the Lorentzian width corresponding to one standard deviations larger width than the mean in figure 19. Therefore, the $2\sigma_{L,\,\mathrm{MA}}$ uncertainty component for the fitted peaks were estimated by fitting to the spectra with modulation amplitudes MA = (0.243 ± 0.010) GHz, taking the mean of the results and multiplying it by two to obtain an approximation for the MA induced uncertainty in the width parameter corresponding to 95% confidence interval. As a result, the MA uncertainty component obtained with this method is also 19 MHz.

It should be emphasized however, that the behavior depicted in figure 18 is an ideal case. The results of the same analysis for the second $^{12}CH_4$ peak in the averaged spectrum discussed in section 4.2 (figure 23) are shown in figure 20. As can be seen, the distribution of the Lorentzian width is no longer purely Gaussian because the response of the width fit parameter to MA shows major deviations from linear behaviour. Furthermore, the resulting Lorentzian width does not decrease with an increasing MA, but the opposite. The deviation from ideal behaviour is probably due to interference between the water and the close proximity $^{14}CH_4$ peak, which affects the fit outcome. Still, the MA uncertainty component obtained with the method explained is 2 MHz, practically the same as the two standard deviations of the width distribution in figure 21, which proves the validity of this method to determine the MA uncertainty component. There is however no guarantee that the method works reliably with each and every measured peak, since the possible deviations from ideal behaviour were not tested for all of the measured peaks.

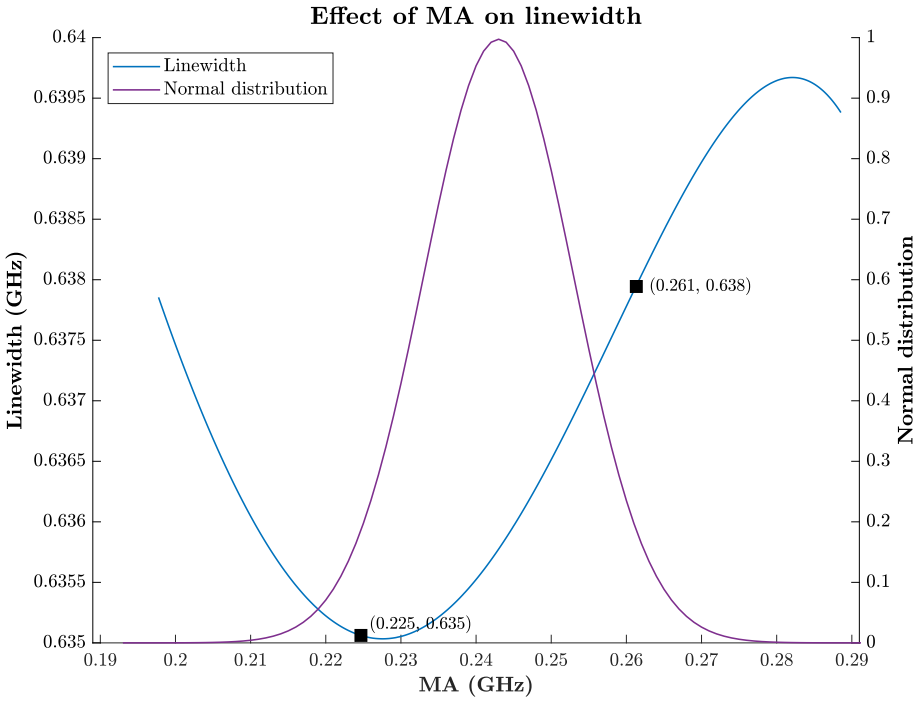

Figure 20: Illustration of the effect of MA on the linewidth of the second $^{12}CH_4$ peak in the averaged spectrum discussed in section 4.2 (figure 23). See the caption of figure 18 for explanation of the different curves.

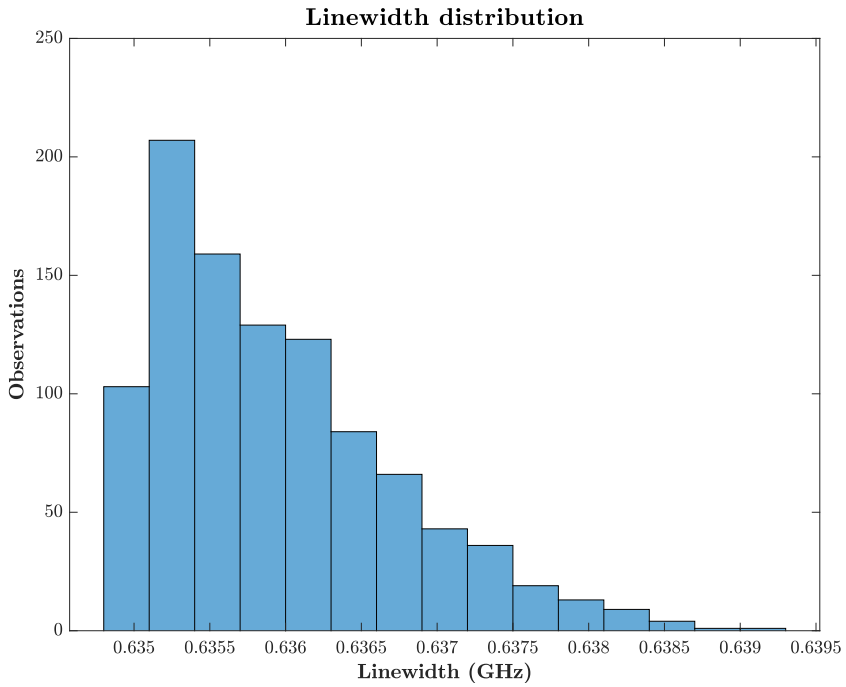

Figure 21: The width distribution for the second $^{12}CH_4$ peak in the averaged spectrum discussed in section 4.2 (figure 23). The distribution is obtained the same way as the distribution in figure 19. The two standard deviations of the distribution is 2 MHz, again fairly well represented by the method explained in the text.

Usually the MA component in the total width uncertainty is smaller than the fit uncertainty: for $^{14}CH_4$ peaks the median of fit uncertainties is about 40 MHz whereas the median of MA uncertainty is about 20 MHz. The overall width uncertainty (equation (16)) is about 25 MHz at best and 120 MHz at worst. On the other hand, this detailed analysis of the width uncertainty is an overkill as the uncertainty in the measurement pressure has not been taken into account in these considerations, see the discussion in section 3.2. Fortunately, the credibility of the width parameter determinations can be assessed by comparing the widths of the measured $^{12}CH_4$ (and water) peaks to their corresponding HITRAN values and furthermore, the measured $^{14}CH_4$ widths to the widths of the corresponding $^{12}CH_4$ transitions. These aspects are discussed in more detail in the next subsection.

4.2. P(3) transitions — reproducibility and averaging

The reproducibility of the measurements, in other words, how well the spectrum of a certain spectral region is reproduced if measured at a later time, was tested by measuring the P(3) transitions of radiomethane six times during three days. Some measurements were executed using the same sample and for some measurements the sample was changed as described in section 3.2. The P(3) region is well suited for reproducibility considerations because it contains several relatively strong $^{14}CH_4$ peaks, a few smaller $^{12}CH_4$ peaks and even one water peak in the background, so there is spectral interference and the fitting model is relatively complex.

The simulated spectrum as well as one of the measured spectra of this spectral region was already presented in figure 16, and all of the measured spectra can be seen in figure 22. Note that every spectrum has been normalized with the corresponding power spectrum (see an example of normalizing in appendix G). It can be seen from the figure that at least qualitatively the spectra are reproduced, even the peak heights match each other quite well. In some of the spectra however, artefacts can be seen due to mode hopping. This illustrates that despite the PID laser piezo scanning (section 3.1.2) a mode hop can affect the quality of the spectra.

Another interesting feature in the figure is the clear background modulation (BM) visible in the spectrum. The BM affects especially the fit uncertainties of the relatively small $^{12}CH_4$ peaks, but because the phase of the BM seems to change between measurements, the BM could probably be reduced by averaging. Averaging is discussed later in this section in more detail, and the origin of the BM is contemplated on in appendix G.

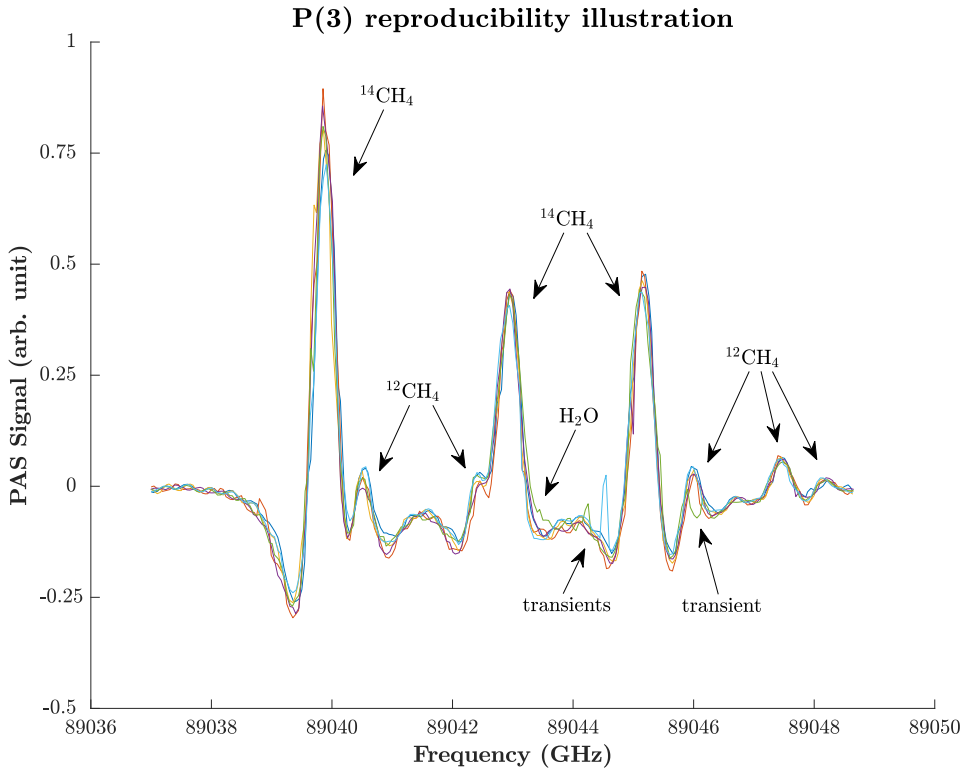

Figure 22: Six spectra of the P(3) transitions measured at different times during three consecutive days to illustrate the reproducibility of the measurement method. Note the labels that indicate which species the peaks belong to. The transients marked in the figure are due to mode hops during the measurements.

The line positions in figure 22 seem reproducible even quantitatively: the standard deviations of the line positions in the spectra are below 30 MHz for the $^{14}CH_4$ peaks, 40 MHz for the $^{12}CH_4$ peaks and 85 MHz for the water peak in the background. The larger variation in the $^{12}CH_4$ and water line positions is expected because the peaks are small and, therefore, more affected by noise in the background and interference from the other peaks. The peak widths, however, show more variation: the relative standard deviations are below 17 % for the $^{14}CH_4$ peaks, below 26 % for the $^{12}CH_4$ peaks and about 62 % for the water peak. As mentioned earlier, the peak heights are not considered quantitatively in this thesis.

Figure 23 shows the averaged spectrum of the spectra in figure 22. It can be seen that the BM is considerably reduced because of averaging. For consistency, the fit results of the P(3) transitions (table 1) are given based on a fit to this averaged spectrum and therefore the uncertainty estimations for the line parameters are done using the method explained in section 4.1. The parameters could be given as an average of the fit results from the separate spectra but the two methods showed only small differences at least for the $^{14}CH_4$ line parameters: < 1 MHz for the line positions and < 10 MHz for the widths not including the water interfered middle $^{14}CH_4$ peak for which the width difference was about 30 MHz.

The choice of method will however affect the uncertainty estimation, the chosen method possibly underestimating the uncertainty. If, for example, two standard deviations of the fit parameters determined from separate spectra are used to calculate the standard error of the mean for the $^{14}CH_4$ peak positions, the resulting values are 30 MHz, 20 MHz and 11 MHz in the order of increasing line position frequency, whereas the corresponding fit uncertainties determined from the averaged spectrum are 3 MHz, 11 MHz and 3 MHz, respectively. The total line position uncertainties are not considerably affected by the averaging or the chosen method of uncertainty estimation because the calibration uncertainty dominates the fit uncertainty as mentioned in subsection 4.1.

Similarly, the standard error of the mean for the widths are 30 MHz, 100 MHz and 50 MHz, whereas the corresponding fit uncertainties, that are expectedly roughly halved in most cases compared to the corresponding values obtained from the unaveraged spectra, are 11 MHz, 100 MHz and 20 MHz, respectively. These results show that the fit uncertainties might not be the best method to describe the uncertainties, but repeated measurements would nevertheless be beneficial for determining the peak parameters more reliably. Repeated measurements are, however, time-consuming due to the long measurement times already mentioned. Despite this discussion, the results for the P(3) transitions in table 1 are given based on the averaged spectrum.

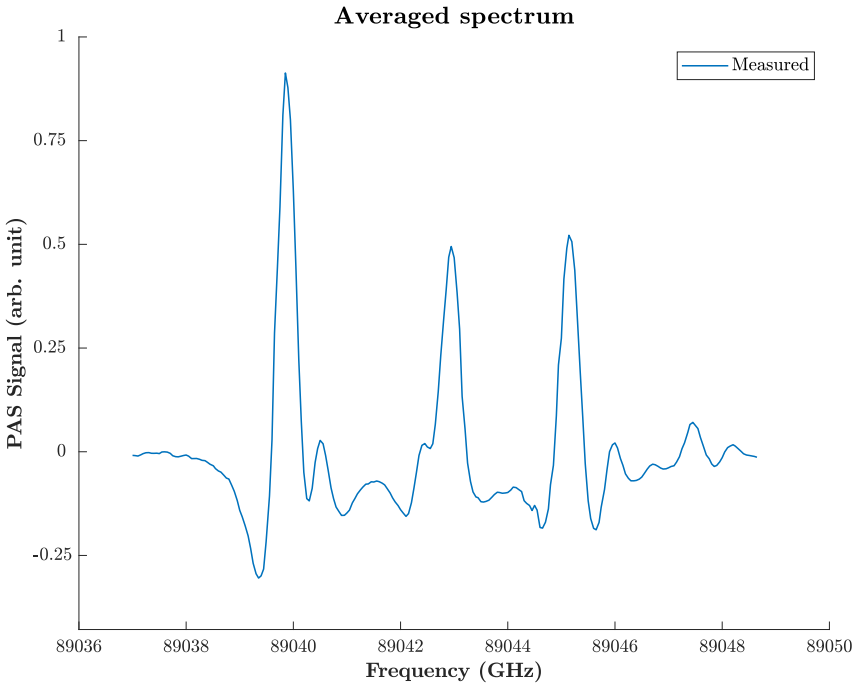

(a) The averaged spectrum.

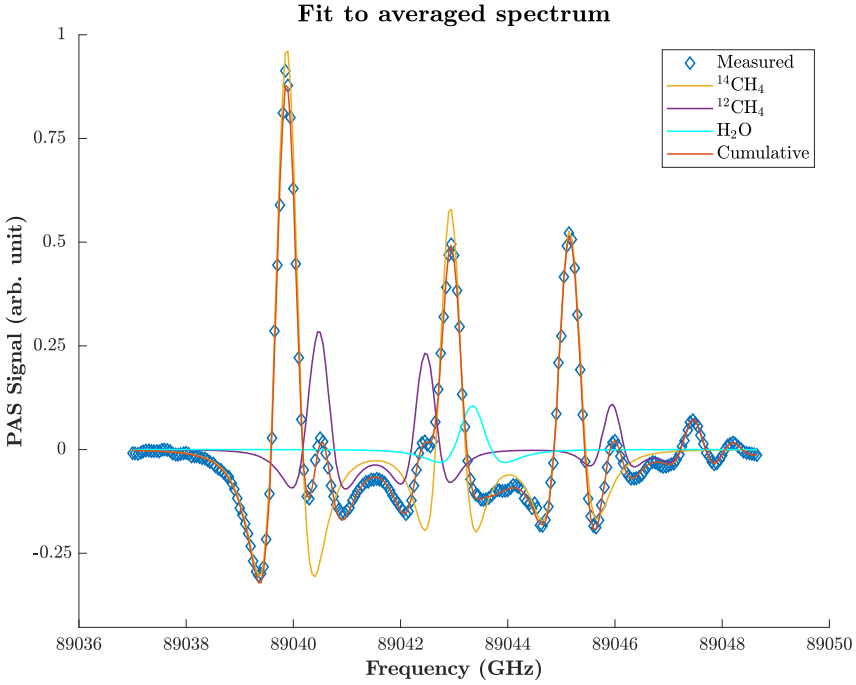

(b) Fit to the averaged spectrum.

Figure 23: The average spectrum of the spectra in figure 22 and a fit to it.

Tables 1 and 2 show fit results of the averaged spectrum. It can be seen that the relative width uncertainties are small not including the second $^{14}CH_4$ peak for which the water peak in the background probably increases the fit uncertainty. The $^{12}CH_4$ widths and the water peak width show larger uncertainties on average but in most cases the width

uncertainties are still larger than the deviations from the HITRAN values. A striking exception is the first $^{12}CH_4$ peak whose width uncertainty is reasonably small but the deviation of the width from the corresponding HITRAN value is 33 %! This example implies that the accuracy of the results might also be questionable for the $^{14}CH_4$ peaks. Fortunately, the credibility of the width results for the $^{14}CH_4$ lines can also be assessed by comparing the results with the corresponding $^{12}CH_4$ transitions, since a previous study[62] shows that the $^{12}CH_4$ and $^{13}CH_4$ widths of the corresponding transitions are reasonably comparable in air as well as in nitrogen. This is why a column comparing $^{14}CH_4$ and $^{12}CH_4$ widths is included in table 1 and in other tables presenting the width results of the radiomethane measurements. The values show satisfactory small deviations from the HITRAN values.

Table 1: The fit results of the averaged spectrum describing the P(3) transitions with ν denoting the center frequencies of the measured lines. The symbol $\delta\nu_{\mathrm{L}}$ refers to the FWHM Lorentz width (section 2.2), and the symbol $\Delta_{\mathrm{L,\,C12}}$ refers to the difference of the measured $^{14}CH_4$ width from the corresponding $^{12}CH_4$ transition width. The numbers in parentheses are the estimated uncertainties in the least significant digits corresponding to 95 % confidence intervals as explained in section 4.1.

ν (GHz)	$\delta\nu_{\mathrm{L}}$ (GHz)	$2\sigma_{\mathrm{L}}$ (%)	$\Delta_{\mathrm{L,\,C12}}$ (GHz)	$\Delta_{\mathrm{L,\,C12}}$ (%)
89040.11(8)	0.78(3)	3	0.03	5
89043.17(9)	0.69(12)	17	-0.13	-17
89045.39(8)	0.78(3)	4	0.02	2

Table 2: The fit results of the $^{12}CH_4$ peaks and the water peak (the last row) in the P(3) transition region of $^{14}CH_4$ with ν denoting the center frequencies of the measured lines. The symbol $\delta\nu_{\mathrm{L}}$ refers to the FWHM Lorentz width (section 2.2), and the symbol Δ refers to the difference of the measured value from the corresponding HITRAN result. The numbers in parentheses are the estimated uncertainties in the least significant digits corresponding to 95 % confidence intervals as explained in section 4.1. Note that the line position uncertainties for the $^{12}CH_4$ peaks and the water peak, calculated in the same way as for the $^{14}CH_4$ peaks (section 4.1), is majorly overestimated for some of the peaks.

ν (GHz)	Δ_ν (GHz)	$\delta\nu_{\mathrm{L}}$ (GHz)	$2\sigma_{\mathrm{L}}$ (%)	Δ_{L} (GHz)	Δ_{L} (%)
89040.71(9)	0.03	0.74(5)	6	0.18	33
89042.70(9)	0.05	0.64(9)	14	0.07	12
89046.18(9)	-0.01	0.48(8)	16	-0.11	-19
89047.70(9)	0.07	0.56(11)	19	-0.06	-10
89048.40(10)	0.05	0.5(3)	52	0.1	13
89043.6(2)	-0.02	1.0(3)	23	-0.1	-5

This subsection showed that the measured spectra are reproducible, especially when considering the line positions. It was also demonstrated that averaging would help to reduce the background modulation in the spectra and therefore improve the width uncertainties. Averaging or repeating measurements in general would, however, be very time-consuming with the current measurement setup due to the already long measurement times. In most cases, the $^{12}CH_4$ or water peak width deviations from the corresponding HITRAN values were small, but also a substantial exception occurred. This exemplifies that small width uncertainties do not necessarily guarantee the accuracy of the results. In this case however, the $^{14}CH_4$ widths were in good agreement also with the corresponding $^{12}CH_4$ transition widths, which gives credibility for the results; another way to judge whether the measured $^{14}CH_4$ peak width results are accurate could be to compare the obtained width parameters of some larger $^{12}CH_4$ or water peaks to their corresponding HITRAN values, because such peaks are not that much affected by noise in the background or interference from other peaks. This is considered, for example, in appendices C and D. In the following subsections and appendices, more examples of the results are given, and it will become even clearer that sometimes the width parameters match well with their corresponding HITRAN values and sometimes not. This is why the width parameters are tabulated in appendix B separately from the line position results (appendix A). Still, the data presented in the width appendix is valuable: never before have the width parameters of radiomethane been measured this reliably and even if the values could be more accurate, the data is useful for future reference.

4.3. R(3) transitions – a comparison with reference 1

The R(3) transitions of radiomethane were also measured by Karhu *et al.*, see for example figure 4 in reference 1. As explained in the article, due to the relatively low SNR (11)[†] and the considerable overlap of the Coriolis components in the pressure used (250 mbar), some simplifications of the fit model were necessary. For example, the line profiles were assumed Lorentzian, the relative intensities of the line components were fixed and all of the component widths were constrained to the same value. These kinds of simplifications were not needed in the measurement of the R(3) lines presented in this thesis; only in the case of some small interfering $^{12}CH_4$ peaks possibly affecting the width parameters of $^{14}CH_4$ lines was fixing the $^{12}CH_4$ peak parameters during fitting implemented. This procedure is explained in more detail in appendix F.

Figure 24 shows the measured second harmonic spectrum and a fit to it, and figure 25 is a reconstruction of the actual absorption spectrum using the fit parameters obtained to ease qualitative comparison of the results. As can be seen, the reconstructed absorption spectrum matches well with the spectrum in reference 1. Furthermore, the SNR (413, defined as the ratio of the height of the peak and one standard deviation of the residual in the wavenumber region 3040.10–3040.17 cm^{-1}), resolution (50 MHz, versus the instrument limited 600 MHz used by Karhu *et al.*) and the overall quality of the spectrum (equidistant measurement points due to the PID laser piezo scanning) are significantly better compared to the spectrum showed in figure 4 in reference 1. Also due to the lower pressure (200 mbar) and the frequency modulation technique used, the Coriolis line components are well separated. The concentration of $^{14}CH_4$ in the sample (1 ppm) leads to a noise equivalent limit of detection of about 3 ppb, which is a considerable improvement compared to references 1 and 58 (90 ppb).

Note that the small $^{12}CH_4$ peaks in figure 24 were not included in the fit model used by Karhu *et al* and that the first $^{12}CH_4$ peak on the left could not be reliably fitted in this thesis work. Therefore, its line parameters were fixed based on the corresponding HITRAN data during fitting. The peak fixing was deemed necessary because in this work

[†]Defined as the ratio of the height of the peak and one standard deviation of the noise close to a flat region near the foot of the peak.[21]

the width parameters of radiomethane were also of interest and the small $^{12}CH_4$ peak could affect the width results; fixing the peaks usually had negligible effect on the fitted line position parameters. As mentioned, the procedure of fixing the peak parameters during fitting is explained in more detail in appendix F.

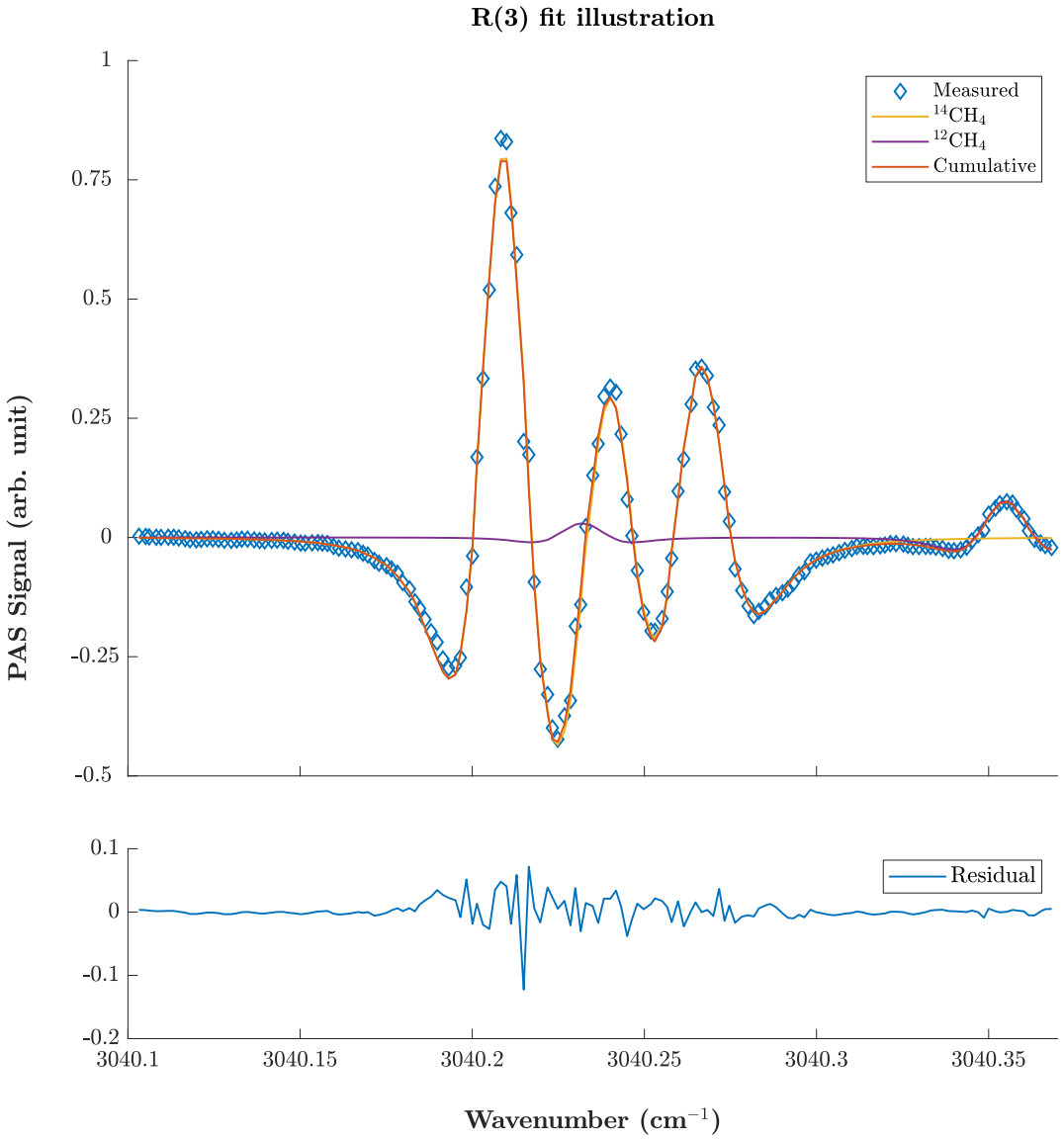

Figure 24: The measured spectrum of the R(3) transition region of $^{14}CH_4$ and a fit to it. The lower part of the figure is the fit residual. Note that the first $^{12}CH_4$ peak is not fitted but its parameters are fixed as explained in appendix F; fixing the peak affects the middle $^{14}CH_4$ peak position by 10 MHz and the width by 25 MHz, which is ignored in the uncertainty estimation.

Table 3 lists the obtained line position parameters for the measured $^{14}CH_4$ peaks. Column 3 in the table shows the correspondence between the results obtained in this work and in reference 1: the values in the column have been obtained by subtracting the corresponding line position value in column 2 by the corresponding line position in table 2 in reference 1,

and the numbers in parenthesis are the one-standard errors of the fit reported in reference 1 – it is important note that the numbers in parenthesis in the second column in table 3 are the line position uncertainties calculated with the method explained in section 4.1 and they correspond to 95 % confidence intervals. Furthermore, the uncertainties estimated in this work also contain the uncertainties resulting from the frequency axis calibration, an uncertainty source not explicitly taken into account in reference 1. It can therefore be said, that the accuracies in the measured transition line positions of radiomethane reported in this work are considerably improved when compared to the results in reference 1. In addition, the results in table 3 are in excellent agreement with the results reported in reference 1.

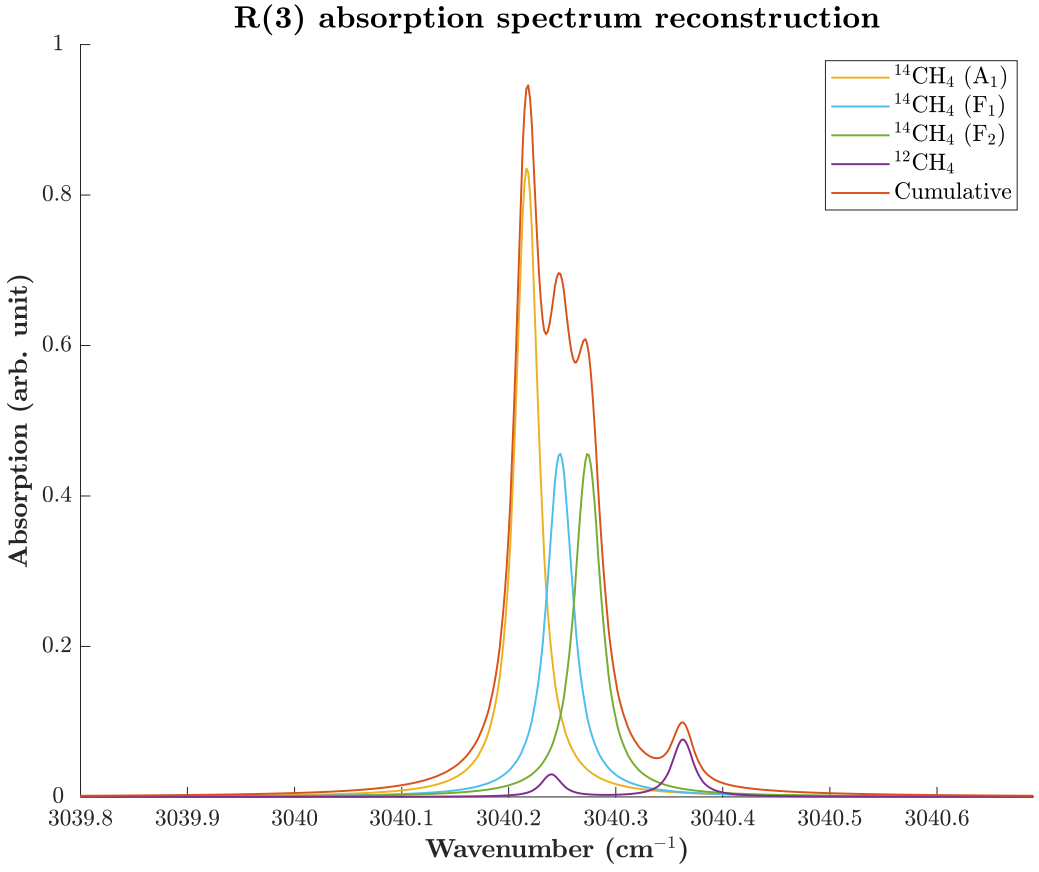

Figure 25: A reconstruction of the actual absorption spectrum of the radiomethane R(3) transition region based on the fit in figure 24. The symmetry labels in the legend refer to the upper state.

Table 3: Fit results of the radiomethane R(3) transitions with $\tilde{\nu}$ denoting the center wavenumbers of the measured lines. The symbol $\Delta_{\tilde{\nu},\,\mathrm{ref}}$ refers to the difference between the line positions in the second column and the corresponding values in reference 1. The numbers in parentheses in the third column are the one-standard errors in the least significant digits given by the least-squares fit in reference 1 – the numbers in parentheses in the second column are the estimated uncertainties in the least significant digits corresponding to 95 % confidence intervals as explained in section 4.1. The symmetry labels refer to the upper state.

Symmetry	$\tilde{\nu}\,(\mathrm{cm}^{-1})$	$\Delta_{\tilde{\nu},\,\mathrm{ref}}\,(\mathrm{cm}^{-1})$
A_1	3040.217(3)	-0.004(2)
F_1	3040.248(3)	0.002(3)
F_2	3040.274(3)	0.003(3)

The widths of the peaks in figure 24, as well as the widths for all of the other measured $^{14}CH_4$ transitions, are tabulated in more detail in appendix B. Briefly, the widths (FWHM) of the R(3) $^{14}CH_4$ peaks are 0.0228(10) cm^{-1}, 0.026(2) cm^{-1} and 0.0266(15) cm^{-1}, in the order of increasing line position wavenumber, and they differ from the corresponding HITRAN values for $^{12}CH_4$ by 5–12 %; the (FWHM) widths of these peaks are roughly 0.021 cm^{-1} according to Karhu *et al.* but taking the pressure difference into account. The width of the $^{12}CH_4$ line on the right in figure 24 is about 0.020(7) cm^{-1} and differs from the corresponding HITRAN value by 4 % giving credibility for the $^{14}CH_4$ line width results despite the differences between the $^{14}CH_4$ linewidths reported by Karhu *et al.* and the ones in this thesis.

In conclusion, the results of the R(3) transitions of radiomethane are in excellent agreement with the corresponding results reported by Karhu *et al.*, but due to the better SNR, resolution and the frequency modulation method used, the line positions have now been determined with improved accuracy. The discussion in this subsection also applies to the other measured transitions, as appendix A lists all the line position results and the agreement with the results in reference 1 is investigated where possible. In addition, appendix B lists the determined radiomethane widths, parameters, that were reported only for the R(3) transitions by Karhu *et al.*, but are now reported for all of the measured $^{14}CH_4$ lines. The width results differ to some extent from the results of Karhu *et al.*, but the correspondence of the new results with the expected HITRAN values are sufficient to imply accuracy for the determined R(3) widths, especially when taking into account the improved quality of the spectrum and the lack of constraints on the fit parameters.

4.4. Branch fitting

In the radiomethane measurements by Karhu *et al.*,[1] many of the P-branch lines could not be reliably assigned due to the relatively low resolution and SNR of the measured spectra. This is why a simple model[57] (equation (17)) was fitted to the measured R-branch lines to predict the positions of other $^{14}CH_4$ lines and aid possible future measurements; the results of this fit can be seen in table 1 in reference 1. Furthermore, using the corresponding data[63] for $^{12}CH_4$, an expression (equation (4.9) in reference 58 if solved for $\tilde{\nu}_{C14}$) to simulate the spectrum of $^{14}CH_4$ based on the corresponding spectrum of $^{12}CH_4$ was presented. This expression was very useful in the measurements described in this thesis to estimate the positions of the $^{14}CH_4$ peaks and identify them. It was noticed, however, that especially in the P-branch the simulated peak positions could differ from the experimental ones even several GHz. This was expected, because the data used in the expression was derived using data from a fit only to the R-branch. Now that many of the P-branch lines have also been measured and reliably assigned, it is good practise to update the parameters of the model to, again, aid possible future measurements.

$$\tilde{\nu} = \tilde{\nu}_0 + (\tilde{B}' + \tilde{B}'' - 2\tilde{B}'\xi)m + (\tilde{B}' - \tilde{B}'')m^2\,, \tag{17}$$

where $\tilde{\nu}_0$ is the branch center, $\tilde{B}'$ and $\tilde{B}''$ are the rotational constants for the excited and ground state, respectively, $2\tilde{B}'\xi$ takes into account the vibrational angular momentum of the excited vibrational state and m is the opposite number of the rotational quantum number of the excited state in the P-branch and the rotational quantum number of the ground state in the R-branch.[57] Considering the fit, the line positions $\tilde{\nu}$ were calculated as a weighted average of the corresponding Coriolis component lines with weights of 5, 2 and 3 for the symmetries A, E and F, respectively.[63]

Figure 26 shows the linear least squares fit of equation (17) to the data obtained from the $^{14}CH_4$ measurements reported here, and table 4 shows the obtained fit parameter values. It can be seen from the residual in figure 26, that the maximum discrepancy between the fitted model and the corresponding experimental values is about -0.082 cm^{-1} (2.4 GHz). This is a considerable improvement, since the corresponding value obtained with the previous model is about -0.520 cm^{-1} (-15.6 GHz). The standard deviation of the discrepancies are 5.4 GHz and 1.1 GHz for the previous and updated models, respectively.

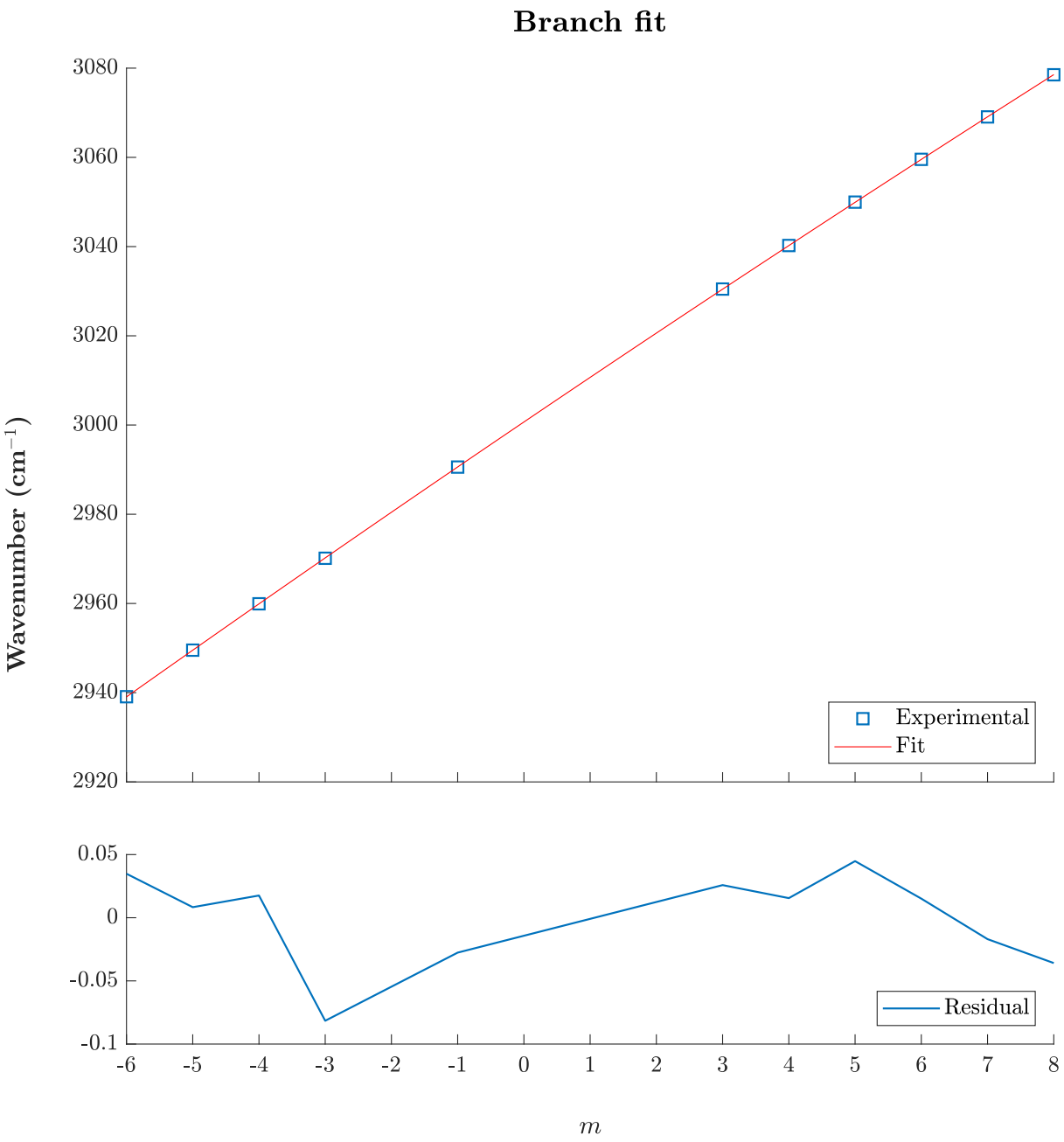

Figure 26: The fit of equation (17) to the P- and R-branch data of $^{14}CH_4$. The lower part of the figure is the fit residual.

Table 4: Results of the linear fit of equation (17) to the P- and R-branch data of $^{14}CH_4$. The parameters are explained in the text, and the numbers in parentheses are the uncertainties corresponding 68 % confidence intervals as given by the fit.

Parameter	Value (cm^{-1})
$\tilde{\nu}_0$	3000.68(3)
$(\tilde{B}' + \tilde{B}'' - 2\tilde{B}'\xi)$	10.040(4)
$(\tilde{B}' - \tilde{B}'')$	-0.0382(10)

The data in table 4 and the corresponding values[63] in literature for $^{12}CH_4$ lead to a similar expression as equation (4.9) in reference 58 to roughly simulate the spectrum of $^{14}CH_4$ based on the spectrum of $^{12}CH_4$:

$$\tilde{\nu}_{\mathrm{C14}} = \frac{10.040\,\mathrm{cm}^{-1}}{9.87\,\mathrm{cm}^{-1}} \left(\tilde{\nu}_{\mathrm{C12}} - 3018.91\,\mathrm{cm}^{-1}\right) + 3000.68\,\mathrm{cm}^{-1}\,. \tag{18}$$

Again, this expression shows considerable improvement compared to the corresponding expression in reference 58, but only in the P-branch: The maximum difference between a simulated peak position and the corresponding experimental peak value in the P-branch is about -3.6 GHz for the updated model (equation (18)) and -12.7 GHz for the previous model (equation (4.9) in reference 58). In R-branch however, the maximum difference between a simulated peak position and the corresponding experimental peak value is -7.8 GHz for the updated model whereas the corresponding value for the previous model is only 1.5 GHz! In general, the expression (18) and equation (4.9) in reference 58 performs poorly due to the neglect of the highest order term in equation (17) and because it does not take the Coriolis fine structure of the transitions properly into account.[†] Furthermore, additional inaccuracy might be introduced also from the used $^{12}CH_4$ literature values. Nonetheless, equation (17) can be used to estimate the transition centers (not taking the Coriolis fine structure into account) with reasonably good accuracy and equation (18) can be used to roughly estimate the spectrum of $^{14}CH_4$ based on the spectrum of $^{12}CH_4$ – these tools should be of use in possible future measurements of new $^{14}CH_4$ lines.

[†]After the completion of this thesis work, the measured data was used in a more rigorous spectroscopic analysis of the absorption band. The more refined model can be used to accurately predict the $^{14}CH_4$ line positions. See appendix H for more details.

5. Conclusions and outlook

In the work discussed in this thesis, several lines of the CH-stretching vibrational band ν_3 of $^{14}CH_4$ were measured with high resolution, SNR and accuracy; the accuracy was ensured by careful calibration of the frequency axis using the known $^{12}CH_4$ transitions. In addition, the determined line positions were in excellent agreement with the corresponding results in reference 1, but also several new lines especially in the P-branch could now be reliably assigned. Furthermore, the simple model presented in reference 1 was updated to better estimate the line positions to aid possible future radiomethane measurements.

The high SNR, and the improved limit of detection, was ensured by the constructed high power mid-infrared OPO and the highly sensitive cantilever-enhanced photacoustic detection system. The OPO was referenced to a wavelength meter and frequency scanning was executed with the help of a PID controller in LabVIEW. This made the measurements convenient, especially because the measurement system could recover automatically from possible mode hops that sometimes occurred despite the intracavity etalon.

The trade-off of the scanning method was the long measurement times especially if a mode hop occurred, and despite the PID, mode hops sometimes produced transients in the measured spectra. For these reasons, a locking scheme to stabilize the OPO signal frequency should also be implemented. This would hopefully prevent mode hops entirely and help reduce the measurement times. This would in turn reduce the effect of leaking gas cell, a major uncertainty source not even taken into account in the uncertainty determinations of the measured linewidths, parameters that were also studied in detail in this thesis.

In contrast to the determined line positions, the results of the linewidth measurements were dubious, which was assessed by noting that in a number of cases, the measured widths of the $^{12}CH_4$ lines did not agree with the corresponding HITRAN values. On the other hand, there were also several cases were the correspondence was surprisingly good. In order to improve the linewidth measurements, in addition to the approaches mentioned above, the background modulation affecting the quality of the measured spectra should be studied further and eliminated, repeated measurements (averaging) should be performed,

a sample gas with higher $^{14}CH_4$ concentration could be used and the SNR should be increased even more. This could be done for example by increasing the idler output power even more, by using better mirrors or by increasing the MA, although the last method would worsen the spectral resolution.

Even though the linewidth results might not be that accurate, the obtained data is important for future reference if radiomethane measurements were continued by some party – after all, never before have the linewidths of $^{14}CH_4$ been studied in this much detail. Especially the determined line positions help to enable future applications that rely on spectroscopic data on radiomethane, for example, quantitative and accurate optical in-situ analysis of $^{14}CH_4$ emissions from nuclear facilities. The results obtained in this thesis are also relevant for fundamental research, as $^{14}CH_4$ is the last naturally occurring isotopologue of methane that has not been extensively studied by optical methods.

In the future, radiomethane measurements should be continued because there are many lines that could not be measured with the current measurement setup due to the limited temperature tuning of the OPO. Also, the Q-branch is yet to be studied in detail, and there are several important parameters, such as the line strengths and pressure shifts of the lines, that should be determined – especially the line strengths would be important for quantitative analysis of $^{14}CH_4$.

References

1. J. Karhu, T. Tomberg, F. Senna Vieira, G. Genoud, V. Hänninen, M. Vainio, M. Metsälä, T. Hieta, S. Bell and L. Halonen, "Broadband photoacoustic spectroscopy of $^{14}CH_4$ with a high-power mid-infrared optical frequency comb", *Opt. Lett.* **44** (2019) 5, pp. 1142–1145.

2. S. Kirschke, P. Bousquet, P. Ciais, M. Saunois, J. G. Canadell, E. J. Dlugokencky, P. Bergamaschi, D. Bergmann, D. R. Blake, L. Bruhwiler, P. Cameron-Smith, S. Castaldi, F. Chevallier, L. Feng, A. Fraser, M. Heimann, E. L. Hodson, S. Houweling, B. Josse, P. J. Fraser, P. B. Krummel, J.-F. Lamarque, R. L. Langenfelds, C. L. Quéré, V. Naik, S. O'Doherty, P. I. Palmer, I. Pison, D. Plummer, B. Poulter, R. G. Prinn, M. Rigby, B. Ringeval, M. Santini, M. Schmidt, D. T. Shindell, I. J. Simpson, R. Spahni, L. P. Steele, S. A. Strode, K. Sudo, S. Szopa, G. R. van der Werf, A. Voulgarakis, M. van Weele, R. F. Weiss, J. E. Williams and G. Zeng, "Three decades of global methane sources and sinks", *Nat. Geosci.* **6** (2013) 10, pp. 813–823.

3. *September 2019, Global CH_4 Monthly Means*, Earth System Research Laboratory Global Monitoring Division, `https://esrl.noaa.gov/gmd/ccgg/trends_ch4/`, 8.1.2020.

4. G. Myhre, D. Shindell, F.-M. Bréon, W. Collins, J. Fuglestvedt, J. Huang, D. Koch, J.-F. Lamarque, D. Lee, B. Mendoza, T. Nakajima, A. Robock, G. Stephens, T. Takemura and H. Zhang, "Anthropogenic and Natural Radiative Forcing" in *Climate Change 2013: The Physical Science Basis. Contribution of Working Group I to the Fifth Assessment Report of the Intergovernmental Panel on Climate Change*, eds. T.F. Stocker, D. Qin, G.-K. Plattner, M. Tignor, S. K. Allen, J. Boschung, A. Nauels, Y. Xia, V. Bex and P.M. Midgley, Cambridge University Press, Cambridge, United Kingdom and New York, NY, USA, 2013, chap. 8.7, pp. 710–740.

5. K. R. Lassey, D. C. Lowe and A. M. Smith, "The atmospheric cycling of radiomethane and the "fossil fraction" of the methane source", *Atmos. Chem. Phys.* **7** (2007) 8, pp. 2141–2149.

6. H. Graven, T. Hocking and G. Zazzeri, “Detection of Fossil and Biogenic Methane at Regional Scales Using Atmospheric Radiocarbon”, *Earth’s Future* **7** (2007) 3, pp. 283–299.

7. N. E. Holden, ”Table of the Isotopes” in *CRC Handbook of Chemistry and Physics*, ed. John R. Rumble, 100$^{\text{th}}$ edn. (Internet Version 2019), CRC Press/Taylor & Francis, Boca Raton, FL, USA, `http://hbcponline.com/faces/contents/ContentsSearch.xhtml`, 8.1.2020.

8. H. Godwin, “Half-life of Radiocarbon”, *Nature* **195** (1962), p. 984.

9. I. U. Olsson, “Modern aspects of radiocarbon datings”, *Earth-Sci. Rev.* **4** (1968), pp. 203–218.

10. W. Kutschera, “Applications of accelerator mass spectrometry”, *Int. J. Mass Spectrom.* **349-350** (2013), pp. 203–218.

11. M. A. Pack, X. Xu, M. Lupascu, J. D. Kessler and C. I. Czimczik, “A rapid method for preparing low volume CH_4 and CO_2 gas samples for ^{14}C AMS analysis”, *Org. Geochem.* **78** (2015), pp. 89–98.

12. I. Galli, S. Bartalini, R. Ballerini, M. Barucci, P. Cancio, M. D. Pas, G. Giusfredi, D. Mazzotti, N. Akikusa and P. D. Natale, “Spectroscopic detection of radiocarbon dioxide at parts-per-quadrillion sensitivity”, *Optica* **3** (2015) 4, pp. 385–388.

13. G. Genoud, J. Lehmuskoski, S. Bell, V. Palonen, M. Oinonen, M.-L. Koskinen-Soivi and M. Reinikainen, “Laser Spectroscopy for Monitoring of Radiocarbon in Atmospheric Samples”, *Anal. Chem.* **91** (2019), pp. 12315–12320.

14. I. Galli, S. Bartalini, S. Borri, P. Cancio, D. Mazzotti, P. D. Natale and G. Giusfredi, “Molecular Gas Sensing Below Parts Per Trillion: Radiocarbon-Dioxide Optical Detection”, *Phys. Rev. Lett.* **107** (2011) 27, 270802, pp. 1–4.

15. G. Genoud, M. Vainio, H. Phillips, J. Dean and M. Merimaa, “Radiocarbon dioxide detection based on cavity ring-down spectroscopy and a quantum cascade laser”, *Phys. Rev. Lett.* **40** (2015) 7, pp. 1342–1345.

16. Å. Magnusson, ^{14}C *Produced by Nuclear Power Reactors – Generation and Characterization of Gaseous, Liquid and Solid Waste*, Ph.D. thesis, Lund University, Lund, 2007.

17. G. Herzberg, *Molecular Spectra and Molecular Structure II. Infrared and Raman Spectra of Polyatomic Molecules*, D. van Nostrand, 1951, 5$^{\text{th}}$ pr. edn., pp. 99–101 and 306–309.

18. W. Chen, J. Cousin, E. Poullet, J. Burie, D. Boucher, X. Gao, M. W. Sigrist and F. K. Tittel, "Continuous-wave mid-infrared laser sources based on difference frequency generation", *Comptes Rendus Physique* **8** (2007) 10, pp. 1129–1150.

19. J. A. Giordmaine and R. C. Miller, "Tunable Coherent Parametric Oscillation in $LiNbO_3$ at Optical Frequencies", *Phys. Rev. Lett.* **14** (1965) 24, pp. 1918–1939.

20. M. Vainio and L. Halonen, "Mid-infrared optical parametric oscillators and frequency combs for molecular spectroscopy", *Phys. Chem. Chem. Phys.* **18** (2016) 6, pp. 4266–4294.

21. J. Karhu, *Frequency Stability and Selectivity of a Singly Resonant Continuous-wave Optical Parametric Oscillator*, Master's thesis, University of Helsinki, Helsinki, 2014, `https://helda.helsinki.fi/bitstream/handle/10138/136543/pro_gradu_jk.pdf?sequence=2&isAllowed=y`, 14.3.2019.

22. J. Peltola, *Jatkuvatoiminen optinen parametrivärähtelijä* [Continuous-wave optical parametric oscillator], Master's thesis, Helsingin yliopisto, Helsinki, 2010.

23. R. Sowade, *Continuous-wave terahertz light from optical parametric oscillators*, Ph.D. thesis, Rheinischen Friedrich-Wilhelms-Universität Bonn, Bonn, 2010, `https://hss.ulb.uni-bonn.de/2010/2361/2361.pdf`, 26.11.2019.

24. R. W. Boyd, *Nonlinear optics*, Academic Press, Burlington, MA, USA, 2008, 3rd edn., chap. 2, pp. 69–133.

25. G. D. Boyd and D. A. Kleinman, "Parametric Interaction of Focused Gaussian Light Beams", *J. Appl. Phys.* **39** (1968) 8, pp. 3597–3639.

26. R. Paschotta, *Birefringence*, RP Photonics Encyclopedia, `https://www.rp-photonics.com/birefringence.html`, 15.1.2020.

27. R. L. Byer and S. E. Harris, "Power and Bandwidth of Spontaneous Parametric Emission", *Phys. Rev.* **168** (1968) 3, pp. 1064–1068.

28. H. H. Abu-Safe, "Difference frequency mixing of strongly focused Gaussian beams in periodically poled $LiNbO_3$", *Appl. Phys. Lett.* **86** (2005) 231105, pp. 1–3.

29. O. Gayer, Z. Sacks, E. Galun and A. Arie, "Temperature and wavelength dependent refractive index equations for MgO-doped congruent and stoichiometric $LiNbO_3$", *Appl. Phys. B: Lasers Opt.* **91** (2008) 2, pp. 343–348.

30. A. E. Siegman, *Lasers*, University Science Books, Mill Valley, CA, 1986, chap. 11, pp. 398–456.

31. T. Tomberg, M. Vainio, T. Hieta and L. Halonen, "Sub-parts-per-trillion level sensitivity in trace gas detection by cantilever-enhanced photoacoustic spectroscopy", *Sci. Rep.* **8** (2018) 1848, pp. 1–7.

32. C. Haisch, "Photoacoustic spectroscopy for analytical measurements", *Meas. Sci. Technol.* **23** (2012) 1, 012001, pp. 1–17.

33. V. Koskinen, J. Fonsen, J. Kauppinen and I. Kauppinen, "Extremely sensitive trace gas analysis with modern photoacoustic spectroscopy", *Vib. Spectrosc.* **42** (2006) 2, pp. 239–242.

34. V. Koskinen, J. Fonsen, K. Roth and J. Kauppinen, "Cantilever enhanced photoacoustic detection of carbon dioxide using a tunable diode laser source", *Appl. Phys. B* **86** (2007) 3, pp. 451–454.

35. G. A. West, J. J. Barrett, D. R. Siebert and K. V. Reddy, "Photoacoustic spectroscopy", *Rev. Sci. Instrum.* **54** (1983) 7, pp. 797–817.

36. A. Miklós, P. Hess and Z. Bozóki, "Application of acoustic resonators in photoacoustic trace gas analysis and metrology", *Rev. Sci. Instrum.* **72** (2001) 4, pp. 1937–1955.

37. P. Kluczynski, J. Gustafsson, Å. M. Lindberg and O. Axner, "Wavelength modulation absorption spectrometry – an extensive scrutiny of the generation of signals", *Spectrochim. Acta, Part B* **56** (2001) 8, pp. 1277–1354.

38. J. M. Supplee, E. A. Whittaker and W. Lenth, "Theoretical Description of Frequency Modulation and Wavelength Modulation Spectroscopy", *Appl. Opt.* **33** (1994) 27, pp. 6294–6302.

39. M. Fehér, Y. Jiang, J. P. Maier and A. Miklós, "Optoacoustic trace-gas monitoring with near-infrared diode lasers", *Appl. Opt.* **33** (1994) 9, pp. 1655–1658.

40. R. N. Hager Jr. and R. C. Anderson, "Theory of the Derivative Spectrometer", *J. Opt. Soc. Am.* **60** (1970) 11, pp. 1444–1449.

41. I. S. Gradshteyn and I. M. Ryzhik, *Table of Integrals, Series, and Products*, Academic press, 1980, corr. and enl. edn, pp. 25–26.

42. *About Lock-In Amplifiers, Application Note #3*, SRS Application Notes, Stanford Research Systems, `https://www.thinksrs.com/support/app.html`, 8.1.2020.

43. W. Demtröder, *Laser spectroscopy, Basic Concepts and Instrumentation*, Springer-Verlag Berlin Heidelberg New York, 1996, 2nd enl. edn., chap. 3, pp. 57–98.

44. J. A. Silver, "Frequency-modulation spectroscopy for trace species detection: theory and comparison among experimental methods", *Appl. Opt.* **31** (1992) 6, pp. 707–717.

45. V. Koskinen, J. Fonsen, K. Roth and J. Kauppinen, "Progress in cantilever enhanced photoacoustic spectroscopy", *Vib. Spectrosc.* **48** (2008) 1, pp. 16–21.

46. F. Schreier, "Comments on 'A Common Misunderstanding about the Voigt Line Profile'", *J. Atmos. Sci.* **66** (2009) 6, pp. 1860–1864.

47. B. Armstrong, "Spectrum line profiles: The Voigt function", *J. Quant. Spectrosc. Radiat. Transfer* **7** (1967) 1, pp. 61–88.

48. J. Westberg, J. Wang and O. Axner, "Methodology for fast curve fitting to modulated Voigt dispersion lineshape functions", *J. Quant. Spectrosc. Radiat. Transfer* **133** (2014), pp. 244–250.

49. H. Kogelnik and T. Li, "Laser beams and resonators", *Appl. Opt.* **5** (1966) 10, pp. 1550–1567.

50. M. Vainio, J. Peltola, S. Persijn, F. J. M. Harren and L. Halonen, "Thermal effects in singly resonant continuous-wave optical parametric oscillators", *Appl. Phys. B: Lasers Opt.* **94** (2009) 411, pp. 411–427.

51. J. Peltola, M. Vainio, T. Fordell, T. Hieta, M. Merimaa and L. Halonen, "Frequency-comb-referenced mid-infrared source for high-precision spectroscopy", *Opt. Express* **22** (2014) 26, pp. 32429–32439.

52. A. K. Y. Ngai, S. T. Persijn, G. von Basum and F. J. M. Harren, "Automatically tunable continuous-wave optical parametric oscillator for high-resolution spectroscopy and sensitive trace-gas detection", *Appl. Phys. B: Lasers Opt.* **85** (2006) 2–3, pp. 173–180.

53. E. Kovalchuk, *Optical parametric oscillators for precision IR spectroscopy and metrology*, Ph.D. thesis, Humboldt-Universität zu Berlin, 2008.

54. A. Henderson and R. Stafford, "Low threshold, singly-resonant CW OPO pumped by an all-fiber pump source", *Opt. Express* **14** (2006) 2, pp. 767–772.

55. *Definitions and Units*, HITRANonline (2016 edn.), `https://hitran.org/docs/definitions-and-units/` 28.12.2019.

56. *HITRAN on the Web*, `http://hitran.iao.ru/home`, 28.12.2019.

57. Ref. 17, pp. 451–458.

58. J. Karhu, *Applications of Mid-infrared Frequency Combs for Linear and Nonlinear Vibrational Spectroscopy*, Ph.D. thesis, University of Helsinki, Finland, 2019, `https://helda.helsinki.fi/bitstream/handle/10138/301759/Applicat.pdf?sequence=1&isAllowed=y`, 20.1.2020.

59. *Line-by-Line Search*, HITRANonline (2016 edn.), `https://hitran.org/lbl/`, 28.12.2019.

60. Eqn. 10 in *Evaluation of measurement data – Guide to the expression of uncertainty in measurement* (JCGM 100:2008 GUM 1995 with minor corrections), 1st

edn., 2008, http://www.optique-ingenieur.org/en/courses/OPI_ang_M01_C03/co/Contenu_13.html, 18.1.2020.

61. J. J. Olivero and R. L. Longbothum, "Empirical fits to the Voigt line width: A brief review", *J. Quant. Spectrosc. Radiat. Transfer* **17** (1977) 2, pp. 233–236, eqn. 4a with $C_1 = 1.0692$, $C_2 = 0.86639$ and $C_3 = 1$.

62. V. M. Devi, D. C. Benner, M. A. H. Smith and C. P. Rinsland, "Measurements of air-, N_2-, and O_2 -broadened halfwidths and pressure-induced line shifts in the ν_3 band of $^{13}CH_4$", *Appl. Opt.* **30** (1991) 3, pp. 287–304.

63. R. S. McDowell, "The ν_3 infrared bands of $C^{12}H_4$ and $C^{13}H_4$", *J. Mol. Spectrosc.* **21** (1966) 1–4, pp. 280–290.

64. M. Halonen and L. Halonen, "Rotational analysis of the (2000) stretching vibrational band system of $^{116}SnH_4$", *J. Chem. Phys.* **93** (1990) 3, pp. 1607–1612.

65. A. G. Robiette, D. L. Gray and F. W. Birss, "The effective vibration-rotation hamiltonian for triply-degenerate fundamentals of tetrahedral XY_4 molecules", *Mol. Phys.* **32** (1976) 6, pp. 1591–1607.

66. D. L. Gray and A. G. Robiette, "Extended measurement and analysis of the ν_3 infrared band of methane", *J. Mol. Spectrosc.* **77** (1979) 3, pp. 440–456.

67. J. P. Champion, J. Hilico and L. R. Brown, "The vibrational ground state of $^{12}CH_4$ and $^{13}CH_4$", *J. Mol. Spectrosc.* **133** (1989) 2, pp. 244–255.

68. S. Larnimaa, L. Halonen, J. Karhu, T. Tomberg, M. Metsälä, G. Genoud, T. Hieta, S. Bell and M. Vainio, "High-resolution analysis of the ν_3 band of radiocarbon methane $^{14}CH_4$", *Chem. Phys. Lett.* **750** (2020), 137488, pp. 1-5.

Appendices

A. Tables of determined $^{14}CH_4$ line positions

Table 5 lists the measured $^{14}CH_4$ line positions, whose measured center wavenumbers are denoted by $\tilde{\nu}$. The measurement conditions have been explained in section 4. The symbol $\Delta_{\nu,\,\mathrm{ref}}$ in the table refers to the difference between the line positions in the third column and the corresponding values in reference 1. The numbers in parentheses in the fourth column are the one-standard errors in the least significant digits given by the least-squares fit in reference 1 – the numbers in parentheses in the third column are the estimated uncertainties in the least significant digits corresponding to 95 % confidence intervals as explained in section 4.1. The fifth column is the difference between the measured line positions and theoretically calculated line centers – see appendix H for details. The symmetry labels refer to the upper state.

Table 5: The measured line positions of the $^{14}CH_4$ transitions. See the text for explanations of the symbols.

Transition	Symmetry	$\tilde{\nu}\,(\mathrm{cm}^{-1})$	$\Delta_{\tilde{\nu},\,\mathrm{ref}}\,(\mathrm{cm}^{-1})$	$\Delta_{\tilde{\nu},\,\mathrm{calc}}\,(\mathrm{cm}^{-1})$
P(1)	F_2	2990.573(3)	–	0.0008
P(3)	A_1	2970.058(3)	-0.012(14)	-0.0055
	F_1	2970.160(3)	0.02(3)	-0.0008
	F_2	2970.235(3)	-0.01(2)	0.0026
P(4)	F_1	2959.755(3)	-0.04(4)	-0.0042
	E	2959.901(3)	-0.01(9)	-0.0001
	F_2	2959.955(3)	-0.05(9)	0.0018
	A_2	2960.022(3)	-0.04(5)	0.0026
P(5)	F_2	2949.366(3)	–	-0.0003
	E	2949.419(3)		-0.0004
	F_1	2949.612(3)		0.0014
	F_2	2949.700(3)		0.0005
P(6)	A_2	2938.858(3)	–	0.0025
	F_2	2938.938(3)		0.0029

Table 5 (continues): The measured line positions of the $^{14}CH_4$ transitions. See the text for explanations of the symbols.

Transition	Symmetry	$\tilde{\nu}$ (cm^{-1})	$\Delta_{\tilde{\nu},\,\mathrm{ref}}$ (cm^{-1})	$\Delta_{\tilde{\nu},\,\mathrm{calc}}$ (cm^{-1})
P(6)	F_1	2939.023(3)	–	0.0008
	A_1	2939.245(3)		-0.0007
	F_1	2939.333(3)		-0.0021
	E	2939.356(3)		-0.0029
R(2)	F_1	3030.474(3)	0.006(5)	0.0006
	E	3030.487(3)	0.002(7)	0.0020
R(3)	A_1	3040.217(3)	-0.004(2)	-0.0020
	F_1	3040.248(3)	0.002(3)	0.0004
	F_2	3040.274(3)	0.003(3)	0.0005
R(4)	F_1	3049.898(3)	-0.003(5)	-0.0019
	E	3049.952(3)	0.008(9)	0.0007
	F_2	3049.974(3)	0.000(8)	0.0010
	A_2	3050.007(3)	0.002(4)	0.0015
R(5)	F_2	3059.487(3)	0.015(4)[a]	-0.0014
	E	3059.503(3)	0.001(6)	-0.0013
	F_1	3059.586(3)	0.001(4)	0.0028
	F_2	3059.629(3)	0.005(4)	0.0000
R(6)	A_2	3068.972(3)	0.005(4)	-0.0026
	F_2	3068.996(3)	0.004(8)	-0.0006
	F_1	3069.020(3)	0.001(6)	-0.0039
	A_1	3069.126(3)	0.005(3)	0.0071
	F_1	3069.166(3)	0.015(9)	-0.0012
	E	3069.180(3)	0.009(11)	0.0020
R(7)	F_2	3078.397(3)	–	0.0012
	E	3078.431(3)		0.0045
	F_1	3078.453(3)		0.0020
	A_1	3078.501(3)		-0.0082
	F_1	3078.631(3)		0.0041
	F_2	3078.652(3)		-0.0020

[a] The 3059.487 cm^{-1} and 3059.503 cm^{-1} lines are closely spaced, see figure 34 in appendix G.

B. Tables of determined $^{14}CH_4$ Lorentzian widths

Table 6 lists the measured Lorentzian FWHM linewidths $\delta\nu_L$ for the determined $^{14}CH_4$ lines, whose measured center frequencies are denoted by ν. The measurement conditions have been explained in section 4. The symbol Δ in the table refers to the difference of the measured width from the corresponding HITRAN value. Note that the relative $^{12}CH_4$ linewidth uncertainties are usually 5–10 %, as declared in HITRAN. The numbers in parentheses are the estimated uncertainties in the least significant digits corresponding to 95 % confidence intervals as explained in section 4.1. Also note the discussion in section 3.2 about the pressure possibly affecting the accuracy of the results. The asterisk indicates that there is a fixed peak under the peak in question as discussed in appendix F.

Table 6: The measured linewidths of the $^{14}CH_4$ transitions. See the text for explanations of the symbols.

Transition	ν (GHz)	$\delta\nu_L$ (GHz)	$2\sigma_L$ (%)	$\Delta_{L,\,C12}$ (GHz)	$\Delta_{L,\,C12}$ (%)
P(1)	89655.12(8)	0.63(4)*	6	-0.13	-17
P(3)	89040.11(8)	0.78(3)	3	0.03	5
	89043.17(9)	0.69(12)	17	-0.13	-17
	89045.39(8)	0.78(3)	4	0.02	2
P(4)	88731.23(8)	0.74(4)	5	0.01	2
	88735.59(9)	0.64(5)	7	-0.1	-14
	88737.21(9)	0.78(4)	5	-0.01	-2
	88739.24(8)	0.81(3)	3	0.02	3
P(5)	88419.76(9)	0.68(8)	11	-0.04	-7
	88421.35(9)	0.66(9)	14	-0.08	-11
	88427.16(9)	0.72(8)	10	-0.07	-9
	88429.78(9)	0.70(7)	10	-0.07	-9
P(6)	88104.74(8)	0.66(3)	4	-0.07	-10
	88107.14(9)	0.63(5)*	7	-0.1	-14
	88109.70(9)	0.75(4)	6	-0.01	-2
	88116.36(8)	0.67(3)	5	-0.09	-12
	88118.97(9)	0.68(5)	6	0.04	7
	88119.67(9)	0.69(6)	8	-0.05	-7

Table 6 (continues): The measured linewidths of the $^{14}CH_4$ transitions. See the text for explanations of the symbols.

Transition	ν (GHz)	$\delta\nu_{\mathrm{L}}$ (GHz)	$2\sigma_{\mathrm{L}}$ (%)	$\Delta_{\mathrm{L,\,C12}}$ (GHz)	$\Delta_{\mathrm{L,\,C12}}$ (%)
R(2)	90851.32(9)	0.82(5)	6	0.02	3
	90851.71(9)	0.63(8)	13	-0.08	-11
R(3)	91143.41(8)	0.68(3)	5	-0.04	-5
	91144.34(9)	0.79(5)*	6	0.08	12
	91145.12(9)	0.80(5)	6	0.04	5
R(4)	91433.64(9)	0.69(4)	5	-0.04	-6
	91435.27(9)	0.63(6)	9	-0.15	-20
	91435.93(9)	0.82(6)	7	0.09	12
	91436.92(8)	0.65(4)	5	-0.08	-11
R(5)	91721.12(9)	0.70(5)	6	-0.02	-4
	91721.58(9)	0.64(6)	9	-0.01	-2
	91724.08(8)	0.69(4)	5	-0.03	-5
	91725.37(8)	0.54(3)	6	-0.17	-25
R(6)[a]	92005.46(8)	0.74(3)	4	0.03	5
	92006.18(9)	0.92(6)	6	0.22	31
	92006.90(9)	0.89(5)	6	0.17	25
	92010.09(8)	0.85(3)	4	0.15	22
	92011.28(9)	0.88(8)	9	0.19	28
	92011.69(9)	0.76(10)	13	0.11	17
R(7)	92288.02(9)	0.71(5)	7	0.02	3
	92289.04(9)	0.47(5)	10	-0.12	-21
	92289.71(9)	0.74(5)	7	0.04	7
	92291.13(8)	0.65(3)	5	-0.04	-6
	92295.05(9)	0.78(6)	7	0.11	17
	92295.67(9)	0.81(5)	7	0.15	23

[a]The systematic and large deviations from HITRAN values imply that there might have been an unintentional pressure increase during the measurement.

C. P(2) transitions – water interference

As mentioned in section 4, the P(2)-transitions of radiomethane were also measured, but there was severe spectral interference from water. Figure 27 shows the simulation of the estimated spectrum and figure 28 the measured spectrum including a fit to it, table 7 lists the results obtained from the fit.

As can be seen from the measured spectrum, the two expected radiomethane lines might be under the strong water peak; the $^{14}CH_4$ P-branch peaks usually have even several GHz higher frequencies than the simulation estimate (about 4.7 GHz in P(3) region and 1.8 GHz in P(1) region). The shape and relative heights of the the fitted radiomethane peaks seem to match the simulation, but, for example, the confidence interval for the width parameter of first radiomethane line includes zero. These results are unreliable for assigning the radiomethane lines convincingly and that is why they are shown only in this appendix and are not tabulated in appendices A or B.

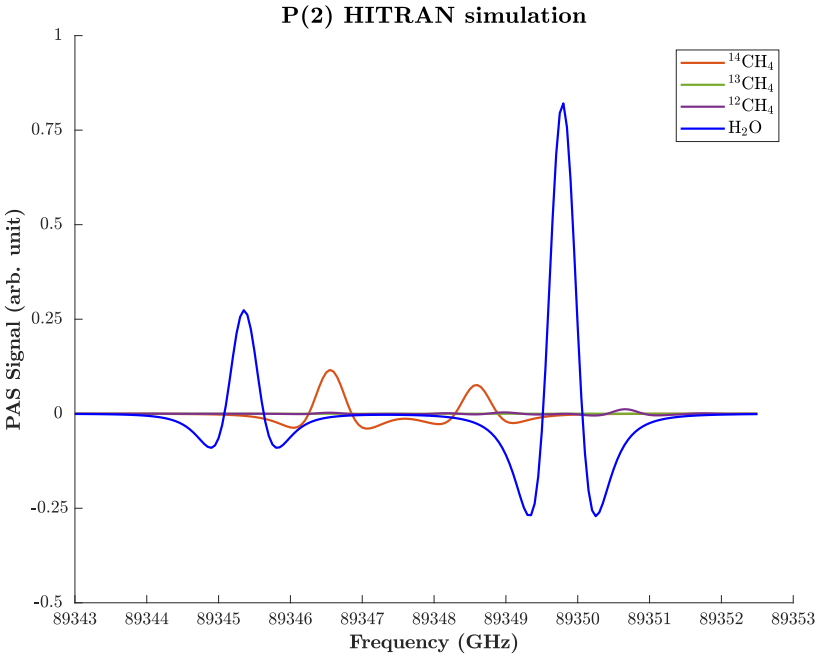

Figure 27: Simulation of the radiomethane P(2) transition region.

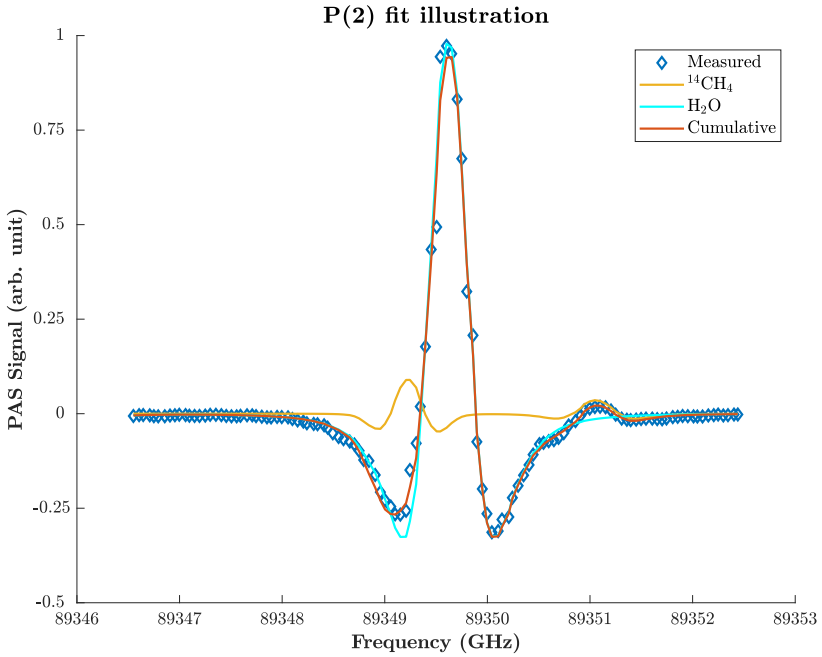

Figure 28: Fit to the measured P(2) transition region of $^{14}CH_4$. The first water line in the simulation (figure 27) was not measured completely and is therefore left out of this figure.

This appendix shows that the P(2) transitions are a poor choice for quantitative analysis of radiomethane, because water is a common spectrally interfering substance in many applications; the water concentration in the sample gas was estimated to be about 2.2 ‰ based on the strong water peak and the reasonably strong $^{12}CH_4$ peak in figure 29 in appendix D. Another reason to illustrate this spectral region is that the width parameter of the strong water peak (subtable 7b) shows good agreement with the corresponding HITRAN value, which might give credibility for the determined width parameters for $^{14}CH_4$ lines, as discussed in subsection 4.2 and as is further discussed in appendix D.

Table 7: Fit results of the radiomethane P(2) transition region. The center frequencies and the Lorentz FWHM values of the lines are denoted by ν and $\delta\nu_L$, respectively. The numbers in parentheses are the estimated uncertainties in the least significant digits corresponding to 95 % confidence intervals as explained in section 4.1.

(a) Fit results of the assumed $^{14}CH_4$ peaks. The symbol $\Delta_{L,\,C12}$ refers to the difference of the measured $^{14}CH_4$ width from the corresponding $^{12}CH_4$ transition width.

ν (GHz)	$\delta\nu_L$ (GHz)	$2\sigma_L$ (%)	$\Delta_{L,\,C12}$ (GHz)	$\Delta_{L,\,C12}$ (%)
89349.47(9)	0.11(15)	137	-0.66	-86
89351.30(9)	0.4(3)	56	-0.2	-32

(b) Fit results of the water peak. The symbol Δ refers to the difference of the measured value from the corresponding HITRAN value.

ν (GHz)	Δ_ν (GHz)	$\delta\nu_L$ (GHz)	$2\sigma_L$ (%)	Δ_L (GHz)	Δ_L (%)
89349.86(8)	0.07	0.62(3)	4	-0.03	-5

D. A reasonably strong $^{12}CH_4$ transition

As discussed in section 4.2, inspecting some reasonably strong $^{12}CH_4$ or water peak widths and their agreements with the corresponding HITRAN values could also give credibility to the measured $^{14}CH_4$ peak widths. In this appendix, one relatively strong $^{12}CH_4$ peak is shown to illustrate this.

Figure 29 shows part of the radiomethane P(5) transition spectrum and a quite strong $^{12}CH_4$ peak. Table 8 shows the fit results of the $^{12}CH_4$ peaks (the fit results of the $^{14}CH_4$ peaks are tabulated in appendices A and B). As can be seen from the table, the strong $^{12}CH_4$ peak width uncertainty is satisfyingly small and the corresponding confidence interval contains the HITRAN value. In contrast, the smaller $^{12}CH_4$ peak shows major deviation from the corresponding HITRAN value, which is probably due to the mode hop that happened during the measurement of the peak, as implied by the power spectrum also included in figure 29. This is a good example of the fact that even though mode hopping does not necessarily ruin measurements due to the laser PID piezo scanning, it can still affect the quality of the spectra and possibly lead to inaccurate results especially when considering the width parameters.

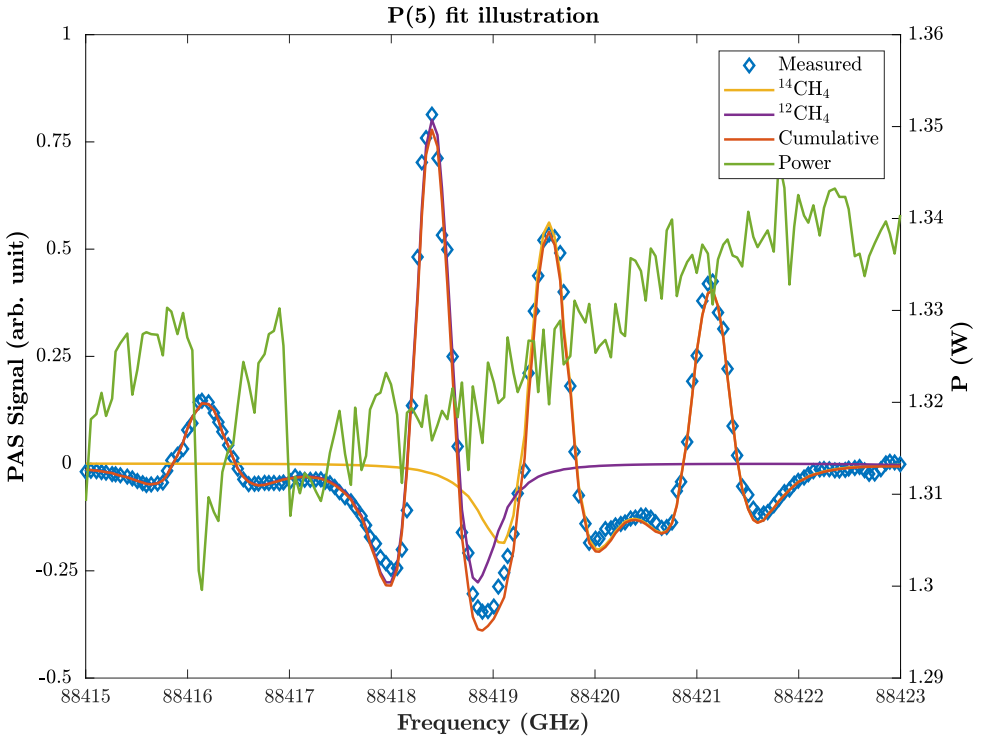

Figure 29: Part of the measured spectrum of the radiomethane P(5) transitions including one relatively strong $^{12}CH_4$ peak. The right vertical axis refers to the power estimated at the PAS cell entrance.

Table 8: The fit results of the two $^{12}CH_4$ peaks in figure 29. The center frequencies and the Lorentz FWHM values of the lines are denoted by ν and $\delta\nu_L$, respectively. The symbol Δ refers to the difference of the measured value from the corresponding HITRAN value, and the numbers in parentheses are the estimated uncertainties in the least significant digits corresponding to 95 % confidence intervals as explained in section 4.1.

ν (GHz)	Δ_ν (GHz)	$\delta\nu_L$ (GHz)	$2\sigma_L$ (%)	Δ_L (GHz)	Δ_L (%)
88416.38(10)	-0.03	0.8(3)	34	0.3	55
88418.62(9)	-0.01	0.55(6)	10	-0.05	-8

E. R(7)-transitions – deviations from expected peak heights

As discussed earlier, the radiomethane peaks were identified partly by noting that their heights matched at least qualitatively the heights predicted by the simulations explained in section 4. This appendix shows an example of a case where the peak heights do not quite match the expected ones.

Figure 30 shows the HITRAN simulation of the R(7) spectral region and figure 31 the measured spectrum of the same region, table 9 shows the obtained fit results. As can be seen from the spectrum, one of the $^{14}CH_4$ peaks but also one of the $^{12}CH_4$ peaks is stronger than expected. What is more, the odd $^{12}CH_4$ peak width is substantially smaller than expected according to HITRAN, whereas the other relatively strong $^{12}CH_4$ peak widths match well with their HITRAN values. There is no apparent reason for these mentioned exceptions, as the corresponding power spectrum (included also in figure 31) does not reveal that any kind of mode hop happened during the measurement. There is however some kind of idler power reduction during the measurement of the last two radiomethane peaks – these kinds of power fluctuations that possibly might affect the accuracy of the determined peaks widths are not explicitly indicated in appendix B tabulating the width results.

Table 9: Fit results of the $^{12}CH_4$ lines in the radiomethane R(7) transition region. The center frequencies and the Lorentz FWHM values of the lines are denoted by ν and $\delta\nu_L$, respectively. The symbol Δ refers to the difference of the measured value from the corresponding HITRAN value, and the numbers in parentheses are the estimated uncertainties in the least significant digits corresponding to 95 % confidence intervals as explained in section 4.1. The asterisk indicates that there is a fixed peak under the peak in question.

ν (GHz)	Δ_ν (GHz)	$\delta\nu_L$ (GHz)	$2\sigma_L$ (%)	Δ_L (GHz)	Δ_L (%)
92297.72(9)	0.02	0.57(5)*	7	-0.02	-4
92298.38(9)	-0.05	0.36(4)	11	-0.19	-35
92300.10(9)	-0.01	0.78(7)	9	0.12	19
92301.34(11)	-0.01	0.8(4)	47	0.3	54

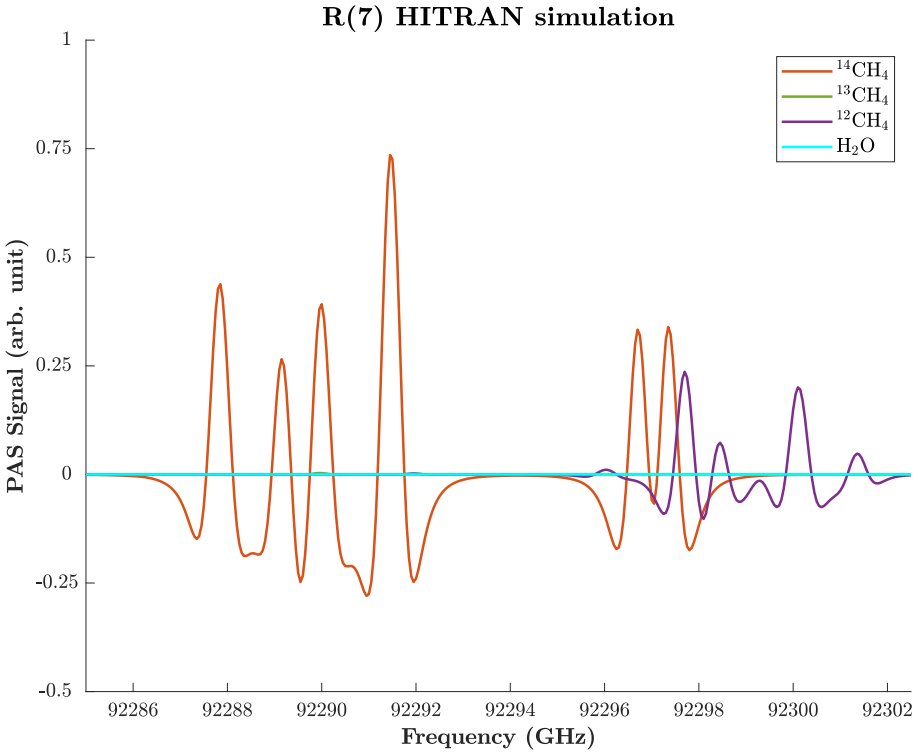

Figure 30: Simulation of the radiomethane R(7) transition region.

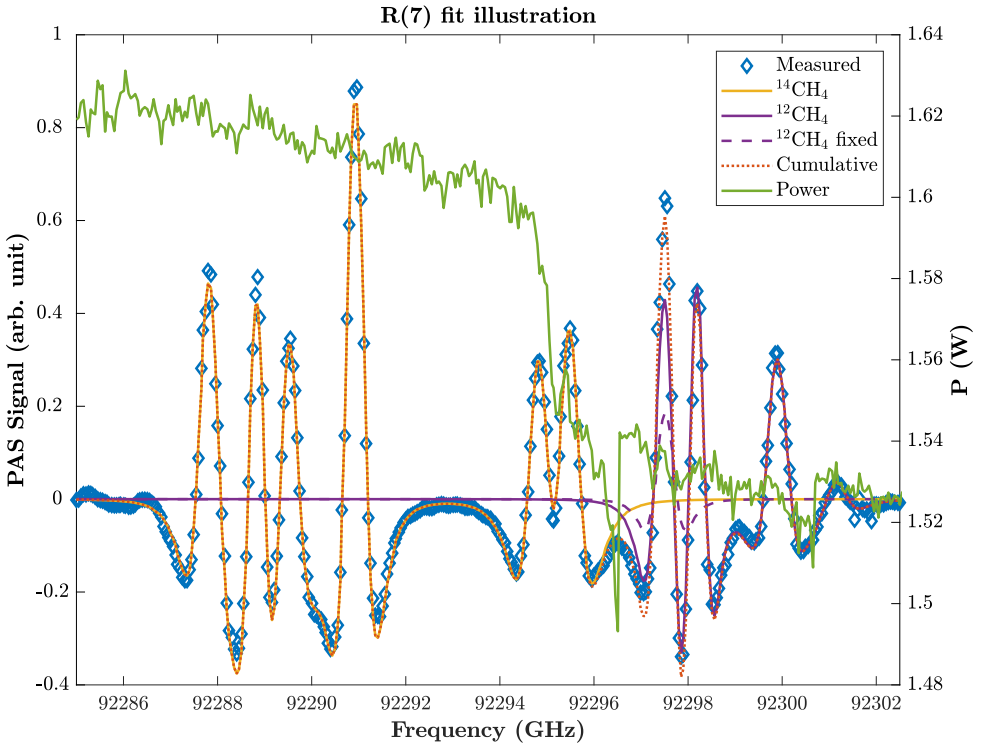

Figure 31: The measured spectrum of the R(7) transition region of $^{14}CH_4$ and a fit to it. Note that one of the $^{12}CH_4$ peaks is fixed (appendix F), which however affected negligibly the fit results of the first fitted $^{12}CH_4$ peak. The right vertical axis describes the power estimated at the PAS cell entrance.

F. P(4)-transitions – illustrating peak parameter fixing

In this appendix it is explained how in some of the measured spectra, some $^{12}CH_4$ peaks were fixed during fitting. The procedure was necessary, for example, if there was major spectral interference between $^{14}CH_4$ and $^{12}CH_4$ peaks in such a way that reliable fitting of the $^{12}CH_4$ line could not be performed and if the peak was considered strong enough to affect the width fit parameter of the radiomethane line. Fixing of the peaks affected usually negligibly the line position parameters, but in the example illustrated below, the relatively strong fixed $^{12}CH_4$ peak shifted the peak position by as much as 50 MHz and the width of the peak was also changed by about 50 MHz. In contrast to the case illustrated in section 4.3, fixing the small $^{12}CH_4$ peak shifted the line position of the $^{14}CH_4$ peak only by 10 MHz but narrowed the Lorentzian width by about 25 MHz. If a $^{12}CH_4$ peak is fixed under some $^{14}CH_4$ peak, it is indicated by an asterisk superscript in the corresponding cell of table 6 in appendix B.

Figure 32 shows the measured P(4)-transitions of radiomethane where the first $^{12}CH_4$ peak (dashed line) is fixed. The peak fixing procedure is as follows: First, all of the other peaks are fitted, so the peak to be fixed is ignored entirely. After this, the fit scaling parameter for a reference peak, in this case the second $^{12}CH_4$ peak, is normalized by the corresponding line intensity obtained from HITRAN, and the result is multiplied by the line intensity of the peak to be fixed. This estimates the strength of the peak to be fixed. Next, the Lorentzian width reported in HITRAN together with the calculated theoretical[55] Gaussian width is used to fix the Voigt width of the peak. Then, the line position is fixed by subtracting an offset from the corresponding HITRAN line position value. The offset is determined by examining how the measured line position of the reference $^{12}CH_4$ peak differs from its corresponding HITRAN value – it is therefore important to note that the fixed peak position is not estimated by the "global offset" (section 4.1) that is otherwise used to calibrate the frequency axes in the measured spectra. Finally, the second harmonic spectrum is simulated for the peak and the result is subtracted from the measurement data before fitting again to the spectrum and presenting the results. It is obvious that there will be additional uncertainty in the fitted $^{14}CH_4$ peak width parameters for peaks that have a fixed $^{12}CH_4$ peak under it, but this uncertainty is not explicitly taken into account. Such peaks are, however, marked with an asterisk as explained earlier.

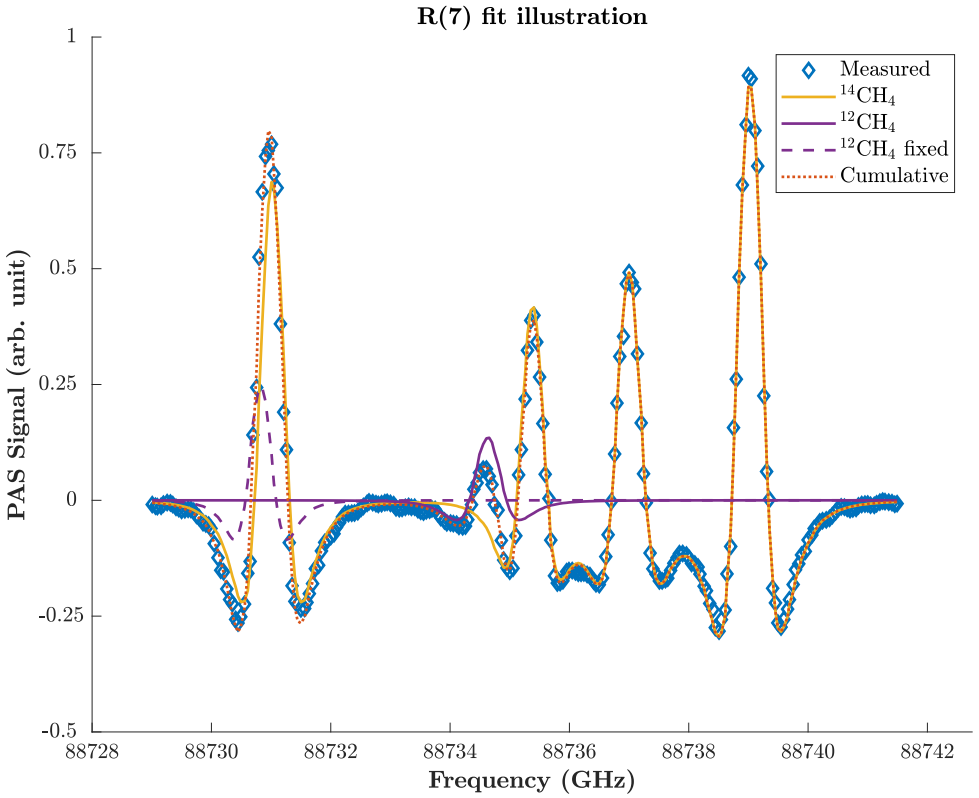

Figure 32: Measured spectrum of the P(4) transition region of $^{14}CH_4$ and a fit to it. The dashed line indicates that the peak is not fitted but fixed, as explained in the text. The fit results off the $^{14}CH_4$ lines are tabulated in appendices A and B.

G. Undesired background modulation

It has already been noticed that in some of the measured spectra there is unwanted modulation in the background, which will affect the fit uncertainties. In section 4.2, it was demonstrated that this background modulation (BM) could be reduced by averaging. In this appendix, the origin of the BM is contemplated on in more detail but is still left somewhat uncertain.

One source for this BM can be an unintended etalon[30] formed by some reflective component or components in the measurement setup:[37] An etalon produces frequency dependent, periodic power modulation that may couple into the photoacoustic signal, for example, by absorption in the cell windows.[31] As a result, one effectively measures the "absorption spectrum" of the etalon.

BM can especially be seen in the R(2) transitions of radiomethane (figure 33). The spectrum has two partially unresolved $^{14}CH_4$ transitions, and the amplitude of the background modulation increases with increasing idler frequency due to a strong water transition at 89349.86(8) GHz (not seen in the figure): the BM couples into the photoacoustic signal probably through increased absorption in the cell caused by water absorption.

If the BM in figure 33 was caused by an etalon, its FSR would be about 360 MHz with standard deviation of about 20 MHz. The length of this supposed etalon would then be about 39–44 cm in air, but such an etalon could not be recognized in the experimental setup; the OPO resonator FSR is about 400 MHz so somewhat larger than the FSR of the suggested etalon. The FSR also does not seem to stay perfectly constant and its phase can change (figure 22 in section 4.2), which also seems to happen after the mode hop evident in figure 33. These notions imply that an etalon is not necessarily the origin of the BM, although the phase change or the changing FSR can be explained by temperature (power) fluctuations, and mode hopping has been proved sometimes to cause transients in the spectra.

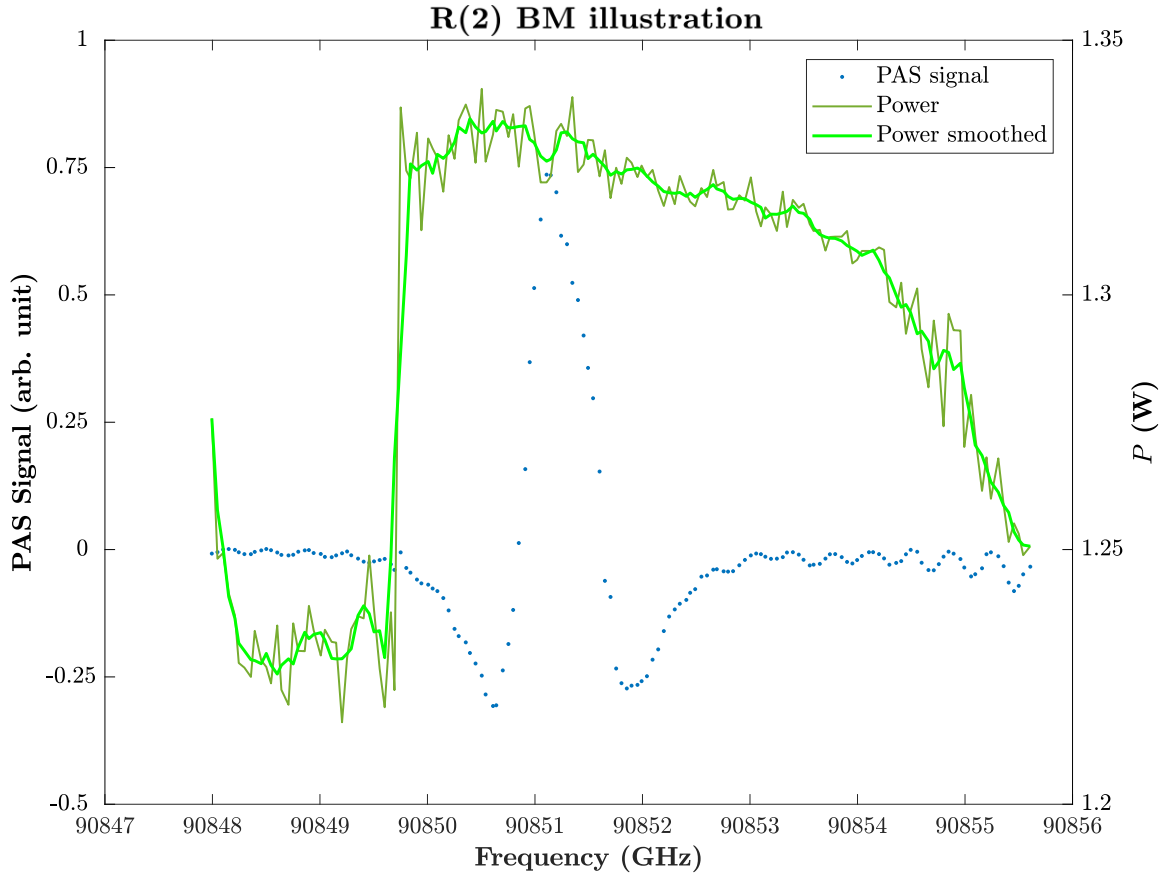

Figure 33: Illustration of the BM affecting the quality of radiomethane R(2) transition spectrum. Note how the amplitude of the background modulation increases with increasing idler frequency (horizontal axis) due increasing water absorption as explained in the text. The right vertical axis describes the idler power estimated at the PAS cell entrance. The light green curve describes the same power data as the dark green curve but in the light green curve the data is smoothed to better assess whether there is periodic nature in the power behaviour. Note also the transient in the PAS signal due to the mode hop implied by the power spectrum.

Another reason for the background modulation could be time dependent but frequency independent power changes. Figure 33 shows also the power spectrum of the measurement (dark green), the light green curve is the power data smoothed. It can be seen that there is indeed some kind power modulation, but the effect is not clearly as reproducible or smooth as the modulation of the PAS signal. Also note that even in the case of an etalon forming the BM, power modulation should be seen in the power spectrum. Maybe the power modulation is masked by noise in the detection system even though there are 15 measurements averaged in each of the measurement points.

The BM is probably not purely time-dependent, because the PAS spectrum shape is practically unaffected by normalization (figure 34): if the power is not frequency dependent and if the period of the power modulation is much longer than the one second it takes

to measure one data point, it is effectively constant during the measurement of the data point and will not be coupled into the second harmonic spectrum generation (section 2.2). In other words, normalization should help to reduce the BM in the measured spectra.

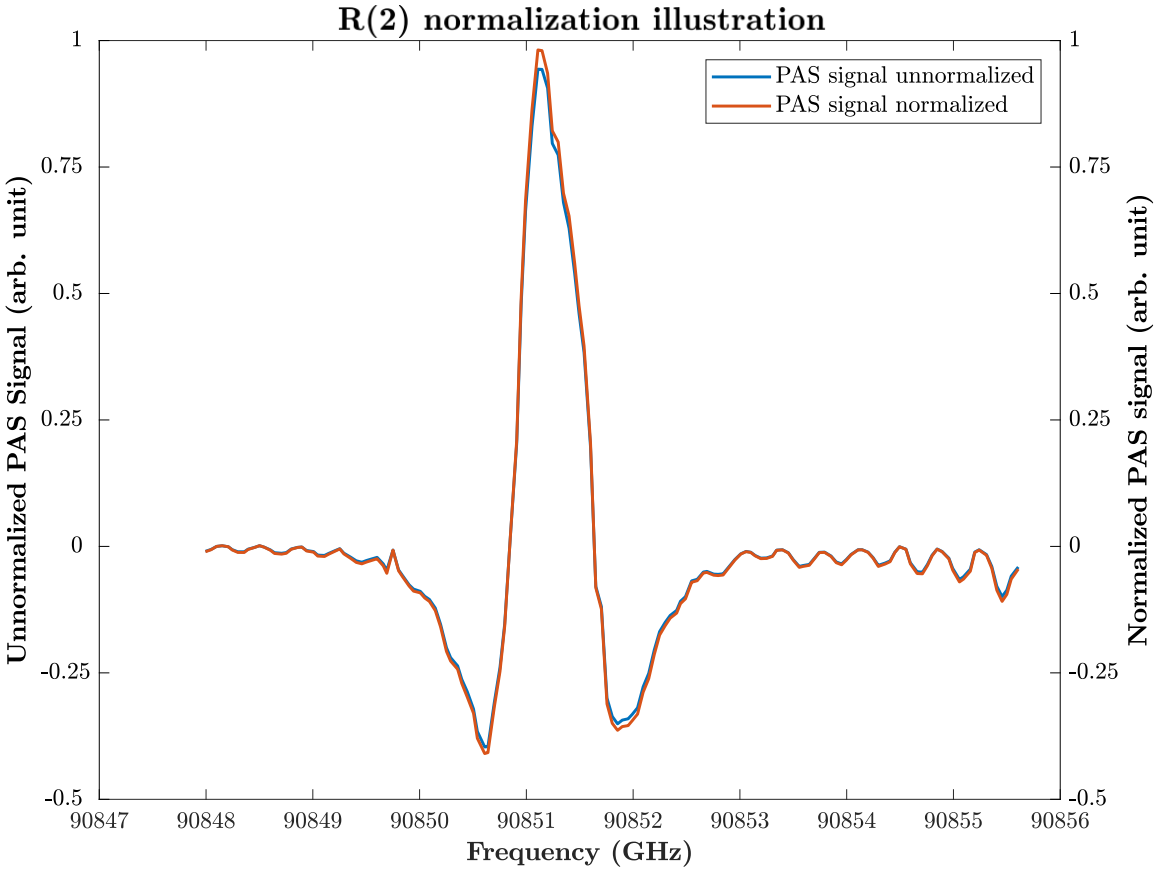

Figure 34: Illustration of the effect of normalizing the measured spectra with the corresponding power spectrum. Note how normalizing affects negligibly to the shape of the spectrum, which is due to the fact that the power is relatively constant during the measurements: in this case the standard deviation of the power data is about 3 % while the average power is about 1.3 W, see figure 33.

In conclusion, the origin of the BM was not identified conclusively. The most obvious reason for the effect would be an unintended etalon, but no etalon matching the observed BM could be identified. Furthermore, purely time dependent power fluctuations are unlikely to explain the BM because the shape of the measured spectra is practically unaffected by normalization. It would be interesting to investigate the origin of the BM further, but such investigations are out of the scope of this thesis work – the peak positions and widths of the $^{14}CH_4$ lines could usually be determined reliably enough despite the BM. More precise determinations of the linewidths would however require elimination of the BM, at least by averaging (section 4.2).

H. A refined model for the ν_3 band

A more refined model describing the ν_3 band of a tetrahedral molecule such as radiomethane was also used in a non-linear least squares fit to analyse the obtained results from the $^{14}CH_4$ line position measurements. The calculations were conducted by Lauri Halonen, Professor at the Department of Chemistry, University of Helsinki.

The Hamiltonian for the ground state of radiomethane is[64,65]

$$\begin{aligned}\tilde{H}'' = {} & \tilde{B}''J(J+1) - \tilde{D}''J^2(J+1)^2 + \tilde{H}''J^3(J+1)^3 \\ & - \left[\tilde{D}''_t + \tilde{H}''_{4t}J(J+1)\right]\mathbf{T}_{044} + \tilde{H}''_{6t}\mathbf{T}_{066}\,,\end{aligned} \tag{19}$$

and similarly the Hamiltonian for the singly excited ν_3 state is[64,65]

$$\begin{aligned}\tilde{H}' = {} & \tilde{\nu}' + \tilde{B}'J(J+1) - \tilde{D}'J^2(J+1)^2 + \tilde{H}'J^3(J+1)^3 \\ & - \left[\tilde{D}'_t + \tilde{H}'_{4t}J(J+1)\right]\mathbf{T}_{044} + \tilde{H}'_{6t}\mathbf{T}_{066} \\ & - 2\tilde{B}'\xi\mathbf{T}_{110} + \tilde{\alpha}_{220}\mathbf{T}_{220} + \tilde{\alpha}_{224}\mathbf{T}_{224}\,,\end{aligned} \tag{20}$$

where only the band center $\tilde{\nu}_0 = \tilde{\nu}' - 2\tilde{B}'\xi$ via the constant $\tilde{\nu}'$ and coefficient $2\tilde{B}'\xi$, upper state rotational constant $\tilde{B}'$, the Coriolis constant ξ via the coefficient $2\tilde{B}'\xi$, centrifugal distortion constants $\tilde{D}'$ and $\tilde{D}'_t$, and the coefficient $\tilde{\alpha}_{224}$ governing the effect of the vibration-rotation tensor operator $\mathbf{T}_{224}$ that partly explains the splitting of the measured lines[65] were optimized in the non-linear least squares fit performed on the measured $^{14}CH_4$ transition band. All the other coefficients, whose purpose and identity is explained in more detail in references 64 and 65, were fixed to the corresponding experimental values of $^{12}CH_4$,[66] except for $\tilde{B}''$ whose value was fixed to the corresponding experimental value of $^{13}CH_4$.[67]

Table 10 shows the obtained fit results for the above-mentioned coefficients. If one calculates the corresponding parameters in table 4 (section 4.4) based on the values in table 10, one notices that the results differ by 0.019 cm^{-1} (570 MHz), 0.0078 cm^{-1} (230 MHz) and -0.0021 cm^{-1} (-60 MHz) from the values in table 10 in listing order. These differences are not surprising considering the crudeness of the model considered in section 4.4, and the discrepancies do not invalidate the discussion in the section. Still, this more refined model can be used to predict even more accurately the line $^{14}CH_4$ positions: the fifth column

in table 5 in appendix A is the difference between the measured line positions and the theoretically calculated line centers based on this more refined model. As can be seen, the convergence of the fit is reasonably good and the square-root of the average of the squared residuals is about 0.003 cm^{-1} (90 MHz), which agrees quite well with the measurement uncertainty. Furthermore, this theoretical consideration proves that the assignments of the measured transitions are correct.

Please note that a scientific article[68] relating to the measurements discussed in this thesis was published upon completion of this thesis work. For example, the article includes also the relative intensities of the measured transition lines calculated based on the spectroscopic model briefly explained in this appendix.

Table 10: The results for the structural parameters obtained from the non-linear least squares fit performed on the measured $^{14}CH_4$ transition band. The numbers in parentheses are the one-standard errors in the least significant digits as given by the fit. The parameter symbols are explained in the text.

Parameter	Value (cm^{-1})
$\tilde{\nu}'$	3001.0544(15)
$\tilde{B}'$	5.20102(9)
$2\tilde{B}'\xi$	0.39492(13)
$\tilde{D}'$	$8.66(11)\times10^{-5}$
$\tilde{D}'_t$	$6.6(2)\times10^{-6}$
$\tilde{\alpha}_{224}$	$-2.313(14)\times10^{-3}$